ION EMISSION STUDY OF PLASMA FOCUS DEVICES AND ITS APPLICATIONS IN MATERIAL SCIENCE

By

RAM NIRANJAN

PHYS01201104019

Bhabha Atomic Research Centre, Mumbai

A thesis submitted to the

Board of Studies in Physical Sciences

In partial fulfillment of requirements

for the Degree of

DOCTOR OF PHILOSOPHY

of

HOMI BHABHA NATIONAL INSTITUTE

August, 2017

Homi Bhabha National Institute[1]

Recommendations of the Viva Voce Committee

As members of the Viva Voce Committee, we certify that we have read the dissertation prepared by **Ram Niranjan** entitled **"Ion emission study of plasma focus devices and its applications in material science"** and recommend that it may be accepted as fulfilling the thesis requirement for the award of Degree of Doctor of Philosophy.

Chairman - **Prof. N. K. Gupta** Date: 18/04/18

Guide / Convener – **Prof. T. C. Kaushik** Date: 18/04/18

Co-guide - --- Date:

Examiner – **Dr. S. R. Mohanty** Date: 18/4/2018

Member 1- **Prof. Amar Sinha** Date:

Member 2- **Prof. D. Bhattacharya** Date: 18/4/18

Member 3- **Prof. Srikumar Ghorui** Date: 18/4/18

Final approval and acceptance of this thesis is contingent upon the candidate's submission of the final copies of the thesis to HBNI.

I/We hereby certify that I/we have read this thesis prepared under my/our direction and recommend that it may be accepted as fulfilling the thesis requirement.

Date:

Place:

<Signature>
Co-guide (if applicable)

<Signature>
Guide

[1] This page is to be included only for final submission after successful completion of viva voce.

STATEMENT BY AUTHOR

This dissertation has been submitted in partial fulfillment of requirements for an advanced degree at Homi Bhabha National Institute (HBNI) and is deposited in the Library to be made available to borrowers under rules of the HBNI.

Brief quotations from this dissertation are allowable without special permission, provided that accurate acknowledgement of source is made. Requests for permission for extended quotation from or reproduction of this manuscript in whole or in part may be granted by the Competent Authority of HBNI when in his or her judgment the proposed use of the material is in the interests of scholarship. In all other instances, however, permission must be obtained from the author.

(Ram Niranjan)

DECLARATION

I, hereby declare that the investigation presented in the thesis has been carried out by me. The work is original and has not been submitted earlier as a whole or in part for a degree / diploma at this or any other Institution / University.

(Ram Niranjan)

List of Publications arising from the thesis

Journal

1. "Effect of gas filling pressure and operation energy on ion and neutron emission in a medium energy plasma focus device", **Ram Niranjan**, R. K. Rout, R. Srivastava, T. C. Kaushik, *J. Appl. Phys.*, **2018**, 123, 093301 (1-6).
2. "A 10^9 neutrons/pulse transportable pulsed D-D neutron source based on flexible head plasma focus unit", **Ram Niranjan**, R. K. Rout, R. Srivastava, T. C. Kaushik, *Rev. Sci. Instrum,* **2016**, *87*, 033504 (1-7).
3. "Surface modifications of fusion relevant materials on exposure to fusion plasma in plasma focus device", **Ram Niranjan**, R. K. Rout, R. Srivastava, Y. Chakravarthy, P. Mishra, T. C. Kaushik, S. C. Gupta, *Appl. Surf. Sci.*, **2015,** *355*, 989-998.
4. "Response of nickel surface to pulsed fusion plasma radiations", **Ram Niranjan**, R. K. Rout, R. Srivastava, Y. Chakravarthy, N. N. Patel, P. Alex, S. C. Gupta, *AIP Conf. Proc.*, **2014**, *1591*, 910-912.
5. "Use of delayed gamma rays for active non-destructive assay of 235U irradiated by pulsed neutron source (plasma focus)", S. Andola, **Ram Niranjan**, T.C. Kaushik, R.K. Rout, A. Kumar, D. B. Paranjape, P. Kumar, B. S. Tomar, K. L. Ramakumar, S.C. Gupta, *Nucl. Instrum. Methods Phys. Res. A*, **2014**, *753*, 138-142.
6. "Low and high energy deuterium ions emission in a 4.7kJ plasma focus device and its variation with gas filling pressure", J. Batra, A. Jaiswar, R. Srivastava, **Ram Niranjan**, R. K. Rout, T. C. Kaushik, *Indian J. Pure Appl. Phys.*, **2014**, *52*, 246-250.
7. "Palm top plasma focus device as a portable pulsed neutron source", R. K. Rout, **Ram Niranjan**, P. Mishra, R. Srivastava, A. M. Rawool, T. C. Kaushik, S. C. Gupta; *Rev. Sci. Instrum.*, **2013**, *84*, 063503 (1-5).

8. "Nondestructive assay of fissile materials through active neutron interrogation technique using pulsed neutron (plasma focus) device", B. S. Tomar, T. C. Kaushik, S. Andola, **Ram Niranjan**, R. K. Rout, A. Kumar, D. B. Paranjape, P. Kumar, K. L. Ramakumar, S. C. Gupta, R. K. Sinha, *Nucl. Instrum. Methods Phys. Res. A*, **2013**, *703*, 11-15.
9. "Characterization of pulsed neutron (plasma focus) source with image plate and application to neutron radiography", S. Andola, **Ram Niranjan**, A. M. Sheikh, R. K. Rout, T. C. Kaushik, and S.C. Gupta, *AIP Conf. Proc.*, **2013**, *1512*, 528-529.
10. "The smallest plasma accelerator device as a radiation safe repetitive pulsed neutron source", **Ram Niranjan**, R. K. Rout, R. Srivastava and S. C. Gupta, *Indian J. Pure Appl. Phys.,* **2012**, *50*, 785-788.
11. "Note: A portable pulsed neutron source based on the smallest sealed type plasma focus device", **Ram Niranjan**, R. K. Rout, P. Mishra, R. Srivastava, A. M. Rawool, T. C. Kaushik, S. C. Gupta, *Rev. Sci. Instrum.,***2011**,*82*, 0261041 (1-3).

Conferences

1. **"**Characteristics of ions produced from plasma focus devices and application to material studies**",** **Ram Niranjan**, R. K. Rout, Rohit Srivastava and T. C. Kaushik, Proc. *10th International Conf. Inertial Fusion Sci. Appl. (IFSA 2017), Saint Malo, France,* **2017**, 322.
2. "Surface modification study of zirconium on exposure to fusion grade plasma in an 11.5 kJ plasma focus device", Rohit Srivastava, **Ram Niranjan**, R. K. Rout, Y. Chakravarthy, P. Mishra and T. C. Kaushik, *32nd National Symp. Plasma Sci. Technol. (PLASMA 2017), IPR, Gandhinagar, India,* **2017.**
3. "Development and application of various portable plasma focus devices as pulsed fusion plasma source", **Ram Niranjan**, R.K. Rout, R. Srivastava, S. Andola, T.C. Kaushik and Satish C. Gupta,

22nd IAEA Tech. Meeting (TM) Res. Small Fusion Device. (RUSFD), Prague, Czech Republic, **2015**.

4. "Pulsed plasma assisted diamond like carbon deposition using 2kJ plasma focus device", **Ram Niranjan**, R. K. Rout, V. Kale, R. Srivastava, N. N. Patel, Y. Chakravarthy, T. C. Kaushik, S. C. Gupta, *30th National Symp. Plasma Sci. Technol. (PLASMA-2015), SINP, Kolkata, India,* **2015**, 325.

5. "Surface modification of titanium, one of the prospective materials for fusion reactor on exposure to fusion plasma radiations", **Ram Niranjan**, R. K. Rout, R. Srivastava, Y. Chakravarthy, P. Alex, S. C. Gupta, *12th National Symp. Nucl. Radiochem. (NUCAR-2015), BARC, Mumbai, India,* **2015**, 116-117.

6. "X-ray dose mapping of an 11.5kJ plasma focus device", R. Srivastava, **Ram Niranjan**, R. K. Rout, N. S. Rawat, A. Soni, D. K. Koul, T.C. Kaushik, S. C. Gupta, *30th National Symp. Plasma Sci. Technol. (PLASMA-2015), SINP, Kolkata, India,* **2015**, 125.

7. "Study of X-ray imaging parameters of plasma focus device using Image plates", S. Andola, **Ram Niranjan**, R. Srivastava, R. K. Rout, T. C. Kaushik, *30th National Symp. Plasma Sci. Technol. (PLASMA-2015), SINP, Kolkata, India,* **2015**, 154.

8. "Indigenous pulsed x-ray and neutron sources for non-destructive material characterization", T. C. Kaushik, R. K. Rout, S. C. Andola, **Ram Niranjan** and S. C. Gupta, *National Seminar International Exhibition Non-Destructive Evaluation, Hyderabad, India,* **2015**, 162.

9. "Development and operation of a flexible transmission line based novel 17kJ capacitor bank with matching plasma focus device", R. K. Rout, **Ram Niranjan**, R. Srivastava, S. C. Gupta, *29th National Symp. Plasma Sci. Technol. (PLASMA-2014) MG University, Kottayam, Kerala, India,* **2014**, 206.

10. "Active neutron Interrogation and delayed neutron counting (AIDNEC) for assay of ^{235}U", S. Andola, **Ram Niranjan**, A. Kumar, D. B. Paranjape, P. Kumar, R. K. Rout, T. C. Kaushik, S.C. Gupta, B. S. Tomar, K. L. Ramakumar, *National Symp. Nucl. Radiochem. (NUCAR-2013), R. D. University, Jabalpur, India,* **2013**, 635.

11. "Active non-destructive assay of nuclear fissile materials using pulsed neutron source (plasma focus) by delayed gamma counting", S. Andola, **Ram Niranjan**, A. Kumar, R. K. Rout, D. B. Paranjape, P. Kumar, T. C. Kaushik, B. S. Tomar, K. L. Ramakumar, S.C. Gupta, *National Symp. Nucl. Radiochem. (NUCAR-2013), R. D. University, Jabalpur, India,* **2013**, 637.

12. "Surface damage from exposure to pulsed fusion grade plasma generated using a plasma focus device", S. C. Gupta, **Ram Niranjan**, R. K. Rout, R. Srivastava, Y. Chakravarthy, N. N. Patel, P. Alex, *28th National Symp. Plasma Sci. Technol. (PLASMA 2013), KIIT Bhubaneshwar, India,* **2013**, 86-87.

13. "Evaluation of half-lives through thermal neutron activation using plasma focus neutron source", R. K. Rout, B. S. Tomar, P. S. Ramanjaneyulu, D. B. Paranjape, **Ram Niranjan**, T. C. Kaushik, S.C. Gupta, *28th National Symp. Plasma Sci. Technol. (PLASMA 2013), KIIT Bhubaneshwar, India,* **2013**, 87.

14. "Detection of ^{4}He generated during the reaction of $^{3}He(^{3}He,2p)^{4}He$ in a plasma focus device using lexan solid state nuclear track detector", **Ram Niranjan**, R. V. Kolekar, R. K. Rout, R. Srivastava and S. C. Gupta, *27th PSSI National Symp. Plasma Sci. Technol. (PLASMA-2012), Pondicherry University, Puducherry, India,* **2012**, 67

15. "Response of tungsten material to fusion grade plasma", **Ram Niranjan**, R. K. Rout, R. Srivastava, D. Joseph, N. N. Patel, S. C. Gupta, *27th PSSI National Symp. Plasma Sci. Technol. (PLASMA-2012), Pondicherry University, Puducherry, India,* **2012**, 128.

16. "On performing neutron radiography using plasma focus neutron source and imaging plate detector", S. Andola, **Ram Niranjan**, A.M. Shaikh, R.K. Rout, T.C. Kaushik, S.C. Gupta, *Proc. National Seminar Exhibition Nondestructive Evaluation NDE, New Delhi, India,* **2012**, 9.

17. "The smallest plasma accelerator device as a radiation safe repetitive pulsed neutron source", **Ram Niranjan**, R. K. Rout, R. Srivastava and S. C. Gupta, *International Conf. Accel. Rad. Safety (ICARS-2011), BARC, Mumbai, India,* **2011**.

18. "Study of ions emitted from a plasma focus device using faraday cup and solid state nuclear track detector", **Ram Niranjan**, R.K. Rout, R. V. Kolekar, R. Srivastava, S. C. Gupta, *26th National Symp. Plasma Sci. Technol. (PLASMA- 2011), BIT, Patna, India,* **2011**,145.

19. "Thermal neutron activation analysis using transportable medium energy plasma focus device", S. C. Gupta, R. K. Rout, B. S. Tomar, P.S. Ramanjaneyulu, D. B. Paranjape, **Ram Niranjan**, T.C. Kaushik, K. L. Ramakumar, R. K. Sinha, *20th IAEA Tech. Meet. Res. using Small Fusion Dev., Vienna, Austria,* **2011.**

(Ram Niranjan)

Dedicated

To

My Family

ACKNOWLEDGEMENTS

I express my heartfelt gratitude to my guide Prof. T. C. Kaushik for his invaluable guidance and constant encouragement throughout this work. I express special gratitude to Dr. R. K. Rout for always being around to advice and to share his knowledge.

I extend my profound gratitude to Dr. Satish. C. Gupta, who provided a constant moral support throughout this work.

Special thanks to the current members of my doctoral committee Dr. N. K. Gupta, Dr. A. Sinha, Dr. D. Bhattacharya, and Dr. S. Ghorui and to the former members Dr. A. K. Das, Dr. A. Shyam for their critical comments and suggestions at various stages of this work.

I thank Shri R. V. Kolekar, RSSD for collaborative work on measurements of ion track densities using various nuclear track detectors.

I am thankful to my colleague and friends Dr. A. K. Saxena and Mr. N. N. Patel for their valuable discussions and meticulous suggestions at various stages of this work.

My special thanks to Mr. Rohit Srivastava, Mr. A. M. Rawool, Ms. Varsha Kale, Mrs. Joycee Jenifer, Mr. A. V. Patil and Mr. K. S. Bonde who provided necessary technical help for carrying out the experimental work.

Finally, I am indebted to my family especially my parents, for their great sacrifices and incessant moral supports.

CONTENTS

CHAPTER 4 EXPERIMENTAL RESULTS AND DISCUSSION

CHAPTER 5 MATERIAL SCIENCES INVESTIGATIONS USING PLASMA FOCUS

SYNOPSIS

Fusion power offers inexhaustible source of clean energy for mankind due to attractive features including vast availability of fusion fuels [Deuterium (D) and Tritium (T)] and almost negligible production of long lived radioactive waste. Fusion fuels are confined to a small volume and their temperatures are raised high enough to facilitate the nuclear fusion reactions. There are mainly two schemes namely magnetic confinement fusion (MCF) where a strong magnetic field is used to contain the hot plasma and inertial confinement fusion (ICF) where high power density lasers and/or particle beams are used to compress the fusion fuels [Ongena et al. 2016, Betti et al. 2016].

Based on MCF, fusion devices of various configurations like Stellerator [Miyamoto 1978], Tokamak [Goldstone 1984], Reversed field pinch [Ortolani 1989] and Spheromak [Jarboe 1994] have been developed. Out of these configurations, tokamak is the most developed and studied. Tokamaks have been studied to address various issues pertaining to physics of fusion plasma such as confinement and stability, transport and turbulence as well as various technological challenges such as selection of materials for different components, their characterization and further improvement, development and testing of diagnostic techniques among others [Goldstone 1984, Federici et al. 2001]. Nevertheless, the commercial deployment of fusion power has been restricted by insurmountable scientific and technological challenges. Selection of materials amongst existing ones or development of new materials remains the main challenge for construction of future fusion reactor such as tokamak based ITER (International Thermonuclear Experimental Reactor) and DEMO (Demonstration power station). Heat loads varying from 0.5 to 20 MW/m^2 on different plasma facing components are estimated to be produced during the ITER normal operation and transient events [type - 1 edge localized modes (ELMs), plasma disruptions, vertical displacement events (VDEs)]. In addition, many components will also be exposed to high flux (10^{14} $n/cm^2/s$) of 14.1 MeV neutrons [$^{2}_{1}D$ ($^{3}_{1}T$, $^{4}_{2}He$) $^{1}_{0}n$] [Federici et al. 2001, Hirai et al. 2005]. It is therefore essential to study the behavior of materials under similar environment.

Various facilities are in operation to irradiate and experimentally simulate the behavior of materials under ITER-relevant conditions like electron beam facilities, particle beam facilities, IR heaters, plasma gun and spallation neutron sources [Hirai et al. 2005]. An accelerator-driven intense neutron source called IFMIF (International Fusion Material Irradiation Facility) is being developed for simulation of effects of 14.1 MeV neutrons on materials. The neutron emission rate of typically 10^{17} n s^{-1} is estimated in IFMIF, which would result in a neutron flux of typically 10^{14} cm^{-2} s^{-1}at the target [Moslang et al. 2000]. Each of these facilities has been used to see effects of heat loads due to specific radiations only. Heat flux produced in the above devices does not match with that estimated to be produced in a fusion reactor. Moreover, they are complex in operation and also high in cost.

Plasma focus (PF) is a fusion device that produces fusion-like environment, by electromagnetic acceleration and compression of plasma, for a short time varying from a few tens to a few hundred nanoseconds [Filippov et al. 1962, Mather 1965]. This is simple in operation and also a low-cost alternative to the above-mentioned devices for understanding various issues related to fusion research. This is a compact source of radiations (ions, electrons, X-rays and neutrons). Neutrons of 2.45 MeV and/ or 14.1 MeV energy are produced when pure deuterium and/or deuterium-tritium mixture gas respectively are used as the filling gases in the PF device. It produces a wide range of heat flux relevant to fusion reactor in the form of ion beam and plasma streams depending on the operation energies and size of the device. Pimenov et al. [2008] used PF devices (PF-1000, PF-6 and PF-5M) with hydrogen and/or deuterium as the filling gas for irradiation of prospective plasma facing materials (tungsten and stainless steel) of a fusion reactor. They have studied the influences of high power density ions and plasma streams upon surface damage, evolution of microstructure and subsequent properties of the materials.

The radiations produced in PF devices have applications in many other areas as well. Ions can be used in material science for applications such as ion implantation [Feugeas et al. 1988], surface

modification [Lepone et al. 1999], thin film deposition [Rawat et al. 1993] and short-lived radioisotope production for medical applications [Roshan et al. 2010]. X-rays are useful in semiconductor industries e.g. micro-lithography [Wong et al. 2004] and in radiography of various substances [Moreno et al. 2002] while neutrons have been used for non-destructive assaying of nuclear materials [Raoux et al. 2003], neutron activation analysis [Tartari et al. 2002], illicit material and explosive detection [Gribkov et al. 2010] along with various other applications [Gribkov et al. 2015].

PF devices operating at energies in sub-kilojoule to megajoule range have been developed in various laboratories across the world since its inception in 1960s independently by N. V. Filippov [Filippov et al. 1962] and J. W. Mather [Mather 1965]. They have been used to understand the underlying science of plasma focus and of fusion plasma as well as for applications. However, even after six decades of intensive research, some of the questions related to plasma focus dynamics and mechanisms of radiation emission such as saturation of neutron yield of PF devices operating at energies beyond MJs range are still difficult to be clearly explained. Various reports are often contradictory in nature [Bernard et al. 1998, Soto 2005, Krishnan 2012].

In view of the above, a number of PF devices operating at energies of 100 J to 17 kJ have been designed and developed in our laboratory [Niranjan et al. 2011**,** Rout et al. 2013**,** Niranjan et al. 2012, Niranjan et al. 2015, Niranjan et al. 2010, Niranjan et al. 2016]. Since durations of various physical processes in the PF device typically range from a few tens of nanoseconds to a few μs, it is important to develop relevant diagnostics techniques to record signals related to the respective processes. In addition, important information about possible physical processes can also be obtained by characterizing the emitted radiations without perturbing plasma focus dynamics. The radiations are emitted for a short time typically ranging from a few ten to a few hundred nanoseconds.

The work in the thesis focuses on development, optimization and study of radiation emission characteristics of different PF devices, specifically operating in the energy range of 200 J to 17 kJ.

The thesis also covers design, development and characterizations of Faraday cup for study of time-resolved emission of ions in PF devices. The ions have been characterized to understand the mechanisms of their acceleration to high energies (up to a few MeV) and to understand their effects on neutron emission as well as for applications in materials science. Applications of PF device as ion source in material science such as for irradiation of fusion reactor relevant materials and for deposition of thin films of carbon have been included. Several other applications of PF device as neutron source such as neutron activation analysis (NAA) of nuclear fissile materials using delayed neutrons [Tomar et al. 2013] and delayed gamma counting [Andola et al. 2014] as well as radio-isotope productions [Rout et al. 2013] have also been discussed.

Two different PF devices operating at energies in sub-kilojoule range have been developed and optimized. The sealed tube based portable PF device, "SPF1-P2" [Niranjan et al. 2011] and the compact repetitive PF device, "PF-P5" [Niranjan et al. 2012] were operated at 200 J and 500 J respectively. The PF configurations of these two devices are of tubular geometry. The SPF1-P2 device uses smallest plasma chamber of volume of 33 cm^3. The plasma chamber was evacuated to $\leq 10^{-5}$ mbar using rotary - diffstac pump and then filled with deuterium gas at optimum pressure (8mbar). Neutron emission was observed for 200 shots over a time span of more than 200 days without refilling of the deuterium gas. Maximum neutron yield of $(3.8 \pm 1.7) \times 10^4$ neutrons/pulse into 4π steradian with a pulse width of (24 ± 5) ns was measured in the first 50 shots. Neutron yield was observed to be decreasing with subsequent PF shots and it was reduced below the detector threshold [(1080 ± 30) neutrons/ shot] of ^{3}He detector after 200 shots. The enhancement in time averaged neutron yield was achieved in the PF-P5 device through repetitive operation. Time averaged neutron yield of $(1.3 \pm 0.2) \times 10^5$ neutrons/pulse in to 4π steradian with a pulse width of (22 ± 5) ns was enhanced to $(1.4 \pm 0.3) \times 10^6$ neutrons/shot (1 shot = 10 neutron pulses) in to 4π steradian at10 Hz repetition rate. This study should prove useful in achieving high neutron yield/shot without increasing the operation energy and the PF device size. Both the devices are compact and portable, hence, they

can be used for applications where not so high neutron yield ($\leq 10^6$ neutrons/shot) is required such as detector testing.

Three other PF devices "PF-2", "MEPF-12" and "MEPF-17" working at energies in kilojoule range have also been developed and optimized for radiation emissions [Niranjan et al. 2015, Niranjan et al. 2010, Niranjan et al. 2016]. The PF configurations of these three devices are of squirrel-cage geometry. The compact plasma focus, "PF-2", operating at 2 kJ, was assembled with a single capacitor (10 μF, 25 kV) while medium energy plasma focus, "MEPF-12" was assembled with a capacitor bank consisting of four capacitors (each 10 μF, 25 kV). PF device in MEPF-12 was assembled using parallel plate transmission lines in a compact geometry. The maximum neutron yield of $(1.2 \pm 0.3) \times 10^9$ neutrons/pulse in to 4π steradian with pulse width of (46 ± 5) ns was obtained when operated at 11.5 kJ. Another medium energy plasma focus, "MEPF-17" device was assembled with a capacitor bank consisting of six capacitors (each, 10 μF, 25 kV). PF device in this case was connected using forty-eight RG213 coaxial cables (each 5 m long). Here, a maximum neutron yield of $(7.1 \pm 1.4) \times 10^8$ neutrons/pulse into 4π steradian was measured when operated at 17 kJ. Long length as well as flexibility of RG213 cables allow PF device to be positioned in any convenient orientation suitable for specific applications. Such provision has been incorporated for the first time in such medium energy operating devices. Anisotropies in neutron yield/energy i.e. ratio of neutron yield/ energy in the axial to that of in the radial direction were measured in MEPF-17 device by varying the filling pressures at 17 kJ. It was observed that the anisotropy factor for neutron yield and neutron energy was (1.33 ± 0.18) and (1.35 ± 0.09) respectively. This suggests that the mechanism of neutron emission is predominantly a beam-target phenomenon, in conformity with other such reported works [Verma et al. 2009].

Effect of operation parameters (filling pressure and operation energy) on emission of ions and neutrons has been studied with deuterium as the filling gas. Numerical computation of ion fluence from different PF devices operating at 0.4 to 480 kJ has been reported by Lee et al. [2012].

Comparative analysis on the characteristics of ion beams from different PF devices operating at energy range of 5 to 50 kJ was reported by Sadowski et al. [2000]. Here, time-resolved emission of ions has been measured using Faraday cup in MEPF-12 device at operation energies of 3.9 to 9.7 kJ and different filling pressures of 1 to 10 mbar. Also, angular emission anisotropy of ions and effect of filling pressures on them was observed using CR39 detector.

Typical deuterium ion fluence of $(7.0 \pm 1.1) \times 10^{14}$ ions/cm^2 at 14 cm axial distance was measured at operation energy of 9.7 kJ and filling gas pressure of 4 mbar. The deuterium ion fluence was observed to be varying with operation energy and filling gas pressure. Variation in deuterium ion fluence over given operating energy range was 13% and for given filling gas pressure range was 19%. The variation was due to possible poor shot to shot reproducibility as well as error in the detection process [Calker et al. 1985, Tarifeno-Saldiviaa et al. 2012]. Therefore, it may be concluded that deuterium ion fluence in the axial direction was nearly independent of operation energy and filling pressure for a specific PF device. Nevertheless, peak density and most probable energy of deuterium ions were observed to be varying significantly with operation energy and filling pressure. Simultaneous measurement of neutrons showed variation of neutron yield/shot and the reason may be attributed to variation in deuterium ion energy spectrum over the operating energy and filling pressure range.

The study of spatial emission profile of ions using CR39 track detector in MEPF-12 device revealed that the ion emission was anisotropic with more ions emitted in the forward direction (30 deg. to electrode axis) than that of in the radial direction (90 deg. to electrode axis) [Sadowski et al. 2000, Jager et al. 1987, Bernstein et al. 1972]. Angular emission anisotropy, ratio of track density in the forward direction to that in radial direction was observed to be varying with filling pressures. The possible reason of this variation is due to change in energy spectrum of ions with filling pressures and this also reinforces the observations carried out using Faraday cup.

MEPF-12 device was used to irradiate different fusion reactor relevant materials viz. tungsten (W), molybdenum (Mo), copper (Cu), nickel (Ni) and stainless steel (SS). Each sample was irradiated with twenty PF discharges. Surface morphologies and surface roughness were characterized using scanning electron microscope (SEM) and surface profilometer respectively. X-ray diffractometer (XRD) was used to characterize crystalline structure and energy dispersive X-ray spectroscopy (EDX) was used to measure elemental compositions of samples before and after irradiation. Irradiations using multiple PF discharges have resulted into melting and erosion of surface layer of all samples. Other effects such as blisters, micro-cracks, pores and voids were also revealed in the SEM images of the irradiated samples. The microcracks were observed to have formed over the entire surface of the W, Mo and Ni samples and it may be concluded that these sample have "brittle fracture" tendencies under exposure to pulse irradiations. On the contrary, the craters were seen to have formed on the surfaces of SS and Cu samples. Comparative analysis of surface damages of all the irradiated samples indicate that the surface of the Cu sample has the most while that of the W sample has the least damage features amongst all irradiated samples.

Comparative analysis of XRD profiles of irradiated samples along with virgin samples revealed no structural phase transformation in W, Mo, Cu and Ni samples but in SS, the structural phase was found to have transformed from initial combined austenitic (γ) and ferritic (α) phase to only austenitic (γ) phase after irradiation [Niranjan et al. 2015].Variation in intensities and shifts in angular positions of diffraction peaks towards higher 2Θ values were observed in the XRD profiles of the irradiated samples. These observations may possibly be due to crystalline defects such as lattice dislocations, point defects as well as compressive stress due to non-steady heat load by the energetic deuterium ions and plasma streams. The EDX analysis of irradiated samples revealed presence of iron (Fe), chromium (Cr) and Ni. This is possibly due to erosion of anode material (SS) due to relativistic electrons post plasma focus disruptions and then depositing over the surface of the target material. The study revealed that materials (W and Mo) having high melting point, low thermal expansion

coefficient and low thermal conductivity as well as high energy threshold for sputtering are suitable for use as plasma facing materials in fusion reactors [Pimenov et al. 2008].

The "PF-2" device has been used for deposition of thin films of carbon when operated with Acetylene (C_2H_2) as the filling gas [Niranjan et al. 2015]. Characterizations of deposited films using Raman spectrometer suggest formation of diamond like carbon (DLC). Moreover, the characteristics of DLC films seem to depend on the depositions conditions such as angular positions with respect to electrode axis and number of PF discharges.

All the above points have been divided in six chapters of thesis as described below.

Chapter-1 begins with a general introduction of plasma focus, its dynamics and radiation emission characteristics. A short review on updated results of the experimental and theoretical works performed by the researchers across the world on the radiation emission from plasma focus device is included. Various current as well as prospective applications of radiations in material science and many other fields have also been discussed. Finally, the chapter concludes by discussing the scope for thesis work behind carrying out the present work.

Chapter-2 describes the details of diagnostics employed in the present work. The diagnostics include electrical (Rogowski coil, resistive divider), neutron detection (silver activation based GM counter, ^{3}He detectors, plastic scintillator-photomultiplier tube) and that for ions (Faraday cup, solid state nuclear track detectors) which have been discussed. The chapter also discusses material characterization techniques used in the present work viz. SEM, EDX, XRD, surface profilometer and Raman spectroscopy.

Chapter-3 presents the design, construction and optimizations of various plasma focus devices operating at energies in sub-kilojoule to kilojoule range developed as a part of the thesis work. This chapter discusses in details about the design criterion of plasma focus devices and associated systems such as capacitor bank, spark gap switches, transmission lines and high voltage charging power supply.

Chapter-4 describes the experimental results. Results on optimizations and radiation emission characteristics of various plasma focus devices used in the work have been discussed in details. Considerable emphasis has been given on the ion emission characteristics of plasma focus devices operating at energies in the kilojoule range.

Chapter-5 discusses the applications of plasma focus devices in different fields. A significant emphasis has been on the exposure of materials to multiple plasma focus discharges and their characterizations. The chapter presents comparative analysis of the surface damages of irradiated materials along with virgin samples. The use of plasma focus for deposition of thin films of carbon on silicon substrates and the effect of ion emission characteristics on the properties of the films has also been discussed.

Chapter-6 summarizes various results and then concludes with future scope of the present work.

To conclude, the thesis reports on design and development of PF devices based on novel concepts. The neutrons emission was observed for the longest time-span (over 200 days) and for the most shots (200 shots) in the sealed "SPF1-P2" device. This is a portable table-top device incorporating smallest plasma chamber among its class of miniature devices reported from different laboratories. Reasonably high neutron yield ($\geq 10^6$ neutrons/pulse) was achieved using another miniature and portable "PF-P5" device in repetitive operation. The provision of orienting plasma focus head through use of RG213 coaxial cables was incorporated for the first time in a medium energy operating MEPF-17 device.

The fluence of ions in MEPF-12 device was observed to be nearly independent of operation energy and filling gas pressure but the peak density and most probable energy were found to be varying. Comparative analysis of materials irradiated using twenty PF discharges revealed that the surface damage features are strongly dependent on the materials properties. The structural phase of SS

material was transformed post irradiation with no such effect being observed in materials like W, Mo, Ni and Cu.

References

1. "Use of delayed gamma rays for active non-destructive assay of ^{235}U irradiated by pulsed neutron source (plasma focus)", Andola S., Niranjan R., Kaushik T.C. et al., *Nucl. Instrum. Methods Phys. Res. A*, **2014**, *753*, 138-142.
2. "Scientific status of plasma focus research", Bernard A., Bruzzone H., Choi P. et al., *Moscow Phys. Soc.*, **1998**, *8*, 93-170.
3. "Neutron energy and flux distributions from a crossed-field acceleration model of plasma focus", Bernstein M. J. Comisar, G. G., *Phys. Fluid*, **1972**, *15*, 700-707.
4. "Inertial-confinement fusion with lasers", Betti R., Hurricane O. A., *Nature Phys.*, **2016**, *12*, 435-448.
5. "Pinch formation and reaction proton spectra of SPEED 1 focus discharges", Calker C. V., Decker G., Jager U. et al., *Phys. Lett. A*, **1985**, *113A*, 203-206.
6. "Plasma-material interactions in current tokamaks and their implications for next step fusion reactors", Federici G., Skinner C. H., Brooks J. N. et al., *Nucl. Fusion*, **2001**, *41*, 1967-2137.
7. "Nitrogen implantation of AISI304 stainless steel with a coaxial plasma gun", Feugeas J., Llonch E. C., deGonzalez C. O. et al., *J. Appl. Phys.*, **1988**, *64*, 2648–2651.
8. "High temperature dense plasma in a non-cylindrical Z-pinch", Filippov N. V., Filipova T. I., Vinogradov V. P., *Nucl. Fusion (suppl.)*, **1962**, *2*, 577-587.
9. "Energy confinement scaling in tokamaks: some implications of recent experiments with ohmic and strong auxiliary heating", Goldstone R. J., *Plasma Phys. Control. Fusion*, **1984**, *26*, 87-103.

10. “Dense Plasma Focus: physics and applications (radiation material science, single-shot disclosure of hidden illegal objects, radiation biology and medicine, etc.)”, Gribkov V. A., Miklaszewski R., Paduch M. et al., *J. Phys.: Conf. Ser.*, **2015**, *591*, 012020(1-19).
11. “A dense plasma focus-based neutron source for a single-shot detection of illicit materials and explosives by a nanosecond neutron pulse”, Gribkov V. A., Latyshev S. V., Miklaszewski R. A. et al., *Phys. Scripta*, **2010**, *81*, 035502 (1-12).
12. “ITER relevant high heat flux testing on plasma facing surfaces”, Hirai T., Ezato K., Majerus P., *Mat. Trans.*, **2005**, *46(2)*, 412-424.
13. “Fast ion kinetics and fusion reaction mechanism in the plasma focus”, Jager U., Herold H., *Nucl. Fusion*, **1987**, *27*, 407-423.
14. “Review of spheromak research”, Jarboe T. R., *Plasma Phys. Control. Fusion*, **1994**, *36*, 945-990.
15. “The Dense Plasma Focus: A Versatile Dense Pinch for Diverse Applications”, Krishnan M., *IEEE Trans. Plasma Sci.*, **2012**, *40(12)*, 3189-3221.
16. “Plasma focus ion beam fluence and flux—scaling with stored energy”, Lee S., Saw S. H., *Phys. Plasmas,* **2012**, *19*, 112703 (1-5).
17. “Surface modification produced by a nitrogen operated plasma focus device: the role of the ion beam in the heating of a substrate”, Lepone A., Kelly H., Lamas D. et al., *Appl. Surf. Sci.,* **1999**, *143*, 124-134.
18. “Formation of a high-density deuterium plasma focus”, Mather J. W., *Phys. Fluids*, **1965**, *8(2)*, 366-377.
19. “Recent stellarator research”, Miyamoto K., *Nucl. Fusion*, **1978**, *18*, 243-284.
20. “Industrial application of plasma focus radiation”, Moreno C., Venere M., Barbuzza R. et al., *Brazillian. J. Phys.,***2002**, *32(1)*, 20-25.

21. "Suitability and feasibility of the International Fusion Materials Irradiation Facility (IFMIF) for fusion materials studies", Moslang A., Ehrlich K., Shannon T. E. et al., *Nucl. Fusion*, **2000**, *40*, 619-627.

22. "Development and study of 13 kJ capacitor bank and plasma focus device", Niranjan Ram, Rout R. K., Srivastava R. et al., *25th National Symp. Plasma Sci. Technol. (PLASMA -2010)*, *IASST, Guwahati, India,* **2010**, 79.

23. "Note: A portable pulsed neutron source based on the smallest sealed type plasma focus device", Niranjan Ram, Rout R. K., Mishra P. et al., *Rev. Sci. Instrum.,* **2011**, *82*, 0261041 (1-3).

24. "The smallest plasma accelerator device as a radiation safe repetitive pulsed neutron source", Niranjan Ram, Rout R. K., Srivastava R. et al., *Indian J. Pure Appl. Phys.,***2012**, *50*, 785-788.

25. "Surface modifications of fusion relevant materials on exposure to fusion plasma in plasma focus device", Niranjan Ram, Rout R. K., Srivastava R. et al., *Appl. Surf. Sci.*, **2015**, *355*, 989-998.

26. "Pulsed plasma assisted diamond like carbon deposition using 2 kJ plasma focus device", Niranjan Ram, Rout R. K., Kale V. et al., *30th National Symp. Plasma Sci. Technol. (PLASMA-2015), SINP, Kolkata, India,* **2015**, 325.

27. "A 10^9 neutrons/pulse transportable pulsed D-D neutron source based on flexible head plasma focus unit", Niranjan Ram, Rout R. K., Srivastava R. et al., *Rev. Sci. Instrum.,* **2016**, *87*, 033504 (1-7).

28. "Magnetic confinement fusion", Ongena J., Koch R., Wolf R. et al., *Nature Phys.*, **2016**, *12*, 398–410.

29. "Reversed field pinch confinement physics", Ortolani S., *Plasma Phys. Control. Fusion*, **1989**, *31*, 1665-1683.

30. "Damage and modification of materials produced by pulsed ion and plasma streams in dense plasma focus device", Pimenov V. N., Demina E. V., Maslyaev S .A. et al., *Nukleonika*, **2008**, *53(3)*, 111-121.

31. "Transuranic waste assay by neutron interrogation and online prompt and delayed neutron measurement", Raoux A. C., Lyoussi A., Passard C. et al., *Nucl. Instrum. Methods Phys. Res.* B, **2003**, *207*, 186–194.
32. "Crystallization of an amorphous lead zirconate titanate thin film with a dense-plasma-focus device", Rawat R. S., Srivastava M. P., Tandon S., and Mansingh A., *Phys. Rev. B*, **1993**, 47, 4858-4862.
33. "Short-Lived PET Radioisotope Production in a Small Plasma Focus Device", Roshan M. V., Springham S. V., Rawat R. S. et al., *IEEE Trans. Plasma Sci.*, **2010**, *38(12)*, 3393-3397.
34. "Evaluation of half-lives through thermal neutron activation using plasma focus neutron source", Rout R. K., Tomar B. S., Ramanjaneyulu P. S. et al., *28th National Symp. Plasma Sci. Technol. (PLASMA 2013), KIIT Bhubaneshwar, India,* **2013**, 87.
35. "Palm top plasma focus device as a portable pulsed neutron source", Rout R. K., Niranjan Ram, Mishra P. et al., *Rev. Sci. Instrum.*, **2013**, *84*, 063503 (1-5).
36. "Comparison of characteristics of pulsed ion beams emitted from different small PF devices", Sadowski M., Skladnik-Sadowska E., Baranowski J. et al., *Nukleonika,* **2000**, 45(3), 179–184.
37. "New trends and future perspectives on plasma focus research", Soto L., *Plasma Phys. Control. Fusion*, **2005***, 47*, A361–A381.
38. "Statistical characterization of the reproducibility of neutron emission of small plasma focus devices", Tarifeno-Saldiviaa A., Soto L., *Phys. Plasmas*, **2012**, *19*, 092512 (1-10).
39. "Improvement of calibration assessment for gold fast-neutron activation analysis using plasma focus devices", Tartari A., Verri G., Da Re A. et al., *Meas. Sci. Technol.*, **2002**, *13*, 939–945.
40. "Non-destructive assay of fissile materials through active neutron interrogation technique using pulsed neutron (plasma focus) device", Tomar B. S., Kaushik T. C., Andola S. et al., *Nucl. Instrum. Methods. Phys. Res. A*, **2013**, *703*, 11-15.

41. “Experimental study of neutron emission characteristics in a compact sub-kilojoule range miniature plasma focus device”, Verma R., Rawat R. S., Lee P. et al., *Plasma Phys. Control. Fusion*, **2009**, *51*, 075008 (1-16).

42. “Soft X-ray optimization studies on a dense plasma focus device operated in neon and argon in repetitive mode”, Wong D., Patran A., Tan T. L. et al., *IEEE Trans. Plasma Sci.*, **2004**, *32(6)*, 2227-2235.

List of Figures **Page No.**

List of Table **Page No.**

Chapter-1

Introduction

1.0 Preamble

Nuclear fusion offers the prospect of an almost inexhaustible source of energy for future generations. It has potential of fulfilling the growing energy demands associated with continued economic growth, given the availability of fusion fuels deuterium (D) and tritium (T). But, the commercial deployment of fusion power has been restricted by insurmountable scientific and engineering challenges. The major challenge has been to develop a device that can heat the fusion fuel (D-T) to a high temperature (≥10 keV) for a long enough time so that energy released through fusion reactions is sufficient to get the reaction going further in the remaining fuel. Broadly, there are two schemes which used to confine the hot plasma (i) magnetic confinement fusion (MCF) [Ongena et al. 2016], and (ii) inertial confinement fusion (ICF) [Betti et al. 2016]. In MCF, a strong magnetic field is used to confine the plasma whereas in ICF, high power lasers and/or particle beams are used to compress fusion fuel pellet to extremely high densities and temperatures.

Various approaches for magnetically confining the plasma have been investigated and they are classified as open and toroidal system. The former contains magnetic mirrors [Post et al. 1987], field reversed configuration [Tuszewski et al. 1988], and cusps [Tuck et al. 1960], while the latter can further be divided into (i) axially symmetric systems viz. Tokamak [Goldstone et al. 1984], Reversed field pinch [Ortolani et al. 1989], Spheromak [Jarboe et al. 1994]), and (ii) axially asymmetric systems viz. Stellerator [Miyamoto et al. 1978], Heliac [Blackwell et al. 1985], Bumpy torus [Uckan et al. 1983]).

The Tokamak is the most developed of all the devices. They have been studied in order to maximize the potential of fusion as an energy source. Most of the studies have been focused on (i) identifying engineering problems such as testing of materials for different components, their

characterization and improvement, (ii) technology developments such as new diagnostic concepts and prototypes, design of control and data acquisition systems and others and (iii) topic concerning plasma physics such as confinement and stability, transport and turbulence. The experiences gained with these studies can further be theoretically extrapolated for next step fusion reactors International Thermonuclear Experimental Reactor (ITER) and Demonstration Power Station (DEMO). However, there are still a number of issues for which the existing database is still fragmentary or which are critical on the basis of extrapolation from present fusion devices. Nevertheless, considering the complexities as well as high cost involved in commissioning and operation of a Tokamak, it is necessary to have simple and low cost alternatives for addressing various issues in order to meet the ITER timeline.

The plasma focus is a fusion device based on Z-pinch principle [Hartman et al. 1977]. This is a coaxial plasma accelerator which essentially uses a self-generated magnetic field to compress the plasma to high density (10^{19} - 10^{20} cm^{-3}) and temperature (~ 1 keV). It is simple in operation and economical where conditions similar to fusion reactor are produced for a few tens to a few hundreds of ns [Mather 1965 & Filippov et al. 1962]. It has generated immense interest among researchers since its inception in early 1960s primarily because of neutron emission. The observation of intense bursts of neutrons from plasma focus led the researchers to believe of achieving controlled thermonuclear fusion. Subsequently, plasma focus devices were developed in various laboratories across the world leading to the great progress in understanding of plasma focus dynamics as well as in improving the associated technologies relevant to controlled fusion research. However, after more than six decades of intensive research, a better understanding of plasma focus dynamics and mechanism of neutron production have raised fundamental doubts on the relevance of plasma focus as the controlled thermonuclear fusion device. Nevertheless, plasma focus devices are currently being used as a tool in controlled fusion research for various investigations like exposure of fusion reactor

relevant materials to understand interaction of fusion grade plasma with material, and testing of diagnostics techniques to be employed in fusion reactor.

Among the various issues, selection of materials for different components of fusion reactor is one of the key issues that need to be resolved for realization of fusion power. Various components in fusion reactor are expected to be exposed to high heat flux in form of energetic plasma particles and electromagnetic radiations. In addition, exposure to high flux ($\sim 10^{17}$ $m^{-2}s^{-1}$) of energetic neutrons (14.1 MeV) will also cause displacement damage which in turn will lead to swelling and embrittlement of component materials [Brooks et al. 2009; Hirai et al. 2005; Renk et al. 2005]. Various radiation sources viz. electron beam, ion/particle beam, IR heaters, plasma guns, laser, and International Fusion Material Irradiation Facility (IFMIF) have been in use for experimental simulation of effects of fusion reactor relevant heat fluxes on prospective materials. Heat fluxes produced in each of the above sources are of specific radiations only and they do not match to that of estimated in the fusion reactors (ITER and DEMO). Moreover, they are complex in operation and of high cost. Plasma focus device has proven to be an excellent simulator for testing of materials in fusion reactor relevant conditions as it provides a realistic fusion reactor environment including all sort of radiations e.g. neutrons, X-rays, electrons and ions. The advantages of plasma focus are high radiation yield with appropriate radiation energy spectrum, point source characteristics and possibility of higher repetition rate operations which allows varying heat flux levels to match the varying heat loads on different components of the fusion reactor in relatively small size as well as at low cost. Moreover, they are being explored for a wide range of applications from activation analysis and material detection to radiography and plasma nanotechnology.

The plasma focus device as a neutron source is being used in many applications such as activation of material for its detection and also to produce short-lived radioisotopes (for applications in industry or medicine). A plasma focus device generating $(3 - 4) \times 10^8$ neutrons per pulse has been reported to be used in fast neutron activation analysis of gold by inelastic scattering in the reaction

^{197}Au (n, n'γ) ^{197}Au [Verri et al. 2000]. A compact plasma focus device producing 2×10^8 neutrons/pulse has been used for detecting water contents of a few percent in volume by neutron scattering [Tartaglione et al. 2004]. Gribkov et al. [2010] reported use of plasma focus based neutron source for single-shot detection of illicit materials and explosives. The device has also been used [Tomar et al. 2013] for activation and non-destructive assay of sample containing ^{235}U using delayed neutron counting through which it has been possible to detect 18 mg of ^{235}U with a neutron yield of $(1.2 \pm 0.3) \times 10^9$ neutron/shot. Similarly, samples were irradiated to assay ^{235}U content using delayed gamma counting wherein the detection limit was observed to be 14 mg of ^{235}U [Andola et al. 2014]. Moreover, owing to its excellent neutron emission characteristics, plasma focus device is also being explored for applications in other areas such as in-vitro irradiation of enzymes [Gribkov et al. 2004, Gribkov et al. 2006], Boron Capture Neutron Therapy (BCNT) [Benzi et al. 2004], and hybrid nuclear reactors based on combined fusion and fission processes [Gribkov 1983, Zoita et al. 2001, Sinha et al. 2015, Clausse et al. 2015].

The plasma focus as an ion source has found many applications including radiation material science (irradiation, implantation and thin film depositions) and for production of short–lived radionuclides useful for medical applications. High energy ions produced in the plasma focus device have been used to produce short-lived isotopes used in nuclear medicine through Positron Emission Tomography (PET) [Roshan et al. 2014]. The deuterium ions produced in the plasma focus device were used to produce ^{13}N radionuclide using nuclear reactions ^{12}C (d, n) ^{13}N for the tomographic diagnostics of human body. Thus, plasma focus as ion source can be a potential alternative to the classical accelerators viz. cyclotrons, LINAC in production of various radio-isotopes, in particular because of its potentially lower cost and simple operation.

X-rays produced in plasma focus devices have been used for applications such as X-ray lithography in microelectronics and radiography. Several groups across the world have used plasma focus device as X-rays source for various commercial applications. Wong et al. [2004] used NX2

plasma focus device at NTU/Singapore as an X-ray source to imprint a test lithograph on a highly sensitive photo-resist SU-8 when operated with neon filling gas. Their 0.2 kJ fast miniature plasma focus device (FMPF-1) was used as a pulsed X-ray source for fast (< 32 ns exposure time) radiographic applications using hydrogen as filling gas [Verma et al. 2010]. The following sections discuss details about construction, working principle and radiation emission characteristics of the plasma focus device.

1.1 Plasma focus device configurations

Operation of the plasma focus device is based on Z -pinch principle. It operates by a fast transfer (typically a few μs) of the electrical energy to a coaxial load by means of a spark gap switch. The electrical energy transforms rapidly into electromagnetic energy through electrical discharge in the gas filled at low pressure of a few mbar. A fraction of the electromagnetic energy is converted into the kinetic energy of plasma through electromagnetic acceleration and compression while the rest is lost in the form of radiations, mainly Bremsstrahlung and line emissions.

It may be worth noting here that various Z – pinch configurations namely classical Z – pinch (Anderson et al. 1958), vacuum spark (Cilliers et al. 1975), exploding wire (Burkhalter et al. 1977), X – pinch (Baker et al. 1979), gas puff (Shiloh et al. 1978), high density Z – pinch (Hammel et al. 1983) have been conceptualized and studied extensively over the years. However, several limitations were experienced with these configurations. The limitations include (1) the pinch disintegrates much before the driver current could attain its maximum value and (2) the insulator wall of the pinch (required initially to launch the snowplow) gets irradiated by pinch radiations. This results in "insulator breakdown".

Above problems are overcome by a device like plasma focus device. The device was originally conceived and developed in two configurations, independently by Filippov and Mather in the early 1960s. Both configurations of plasma focus device have two coaxial electrodes i.e. anode

(center electrode) and cathode (outer electrode) separated by an insulator sleeve. Two configurations differ in aspect ratio (length to diameter) of electrodes i.e. for Mather-type is >1 whereas for Filippov type, it is < 1 as shown in fig. 1.1.

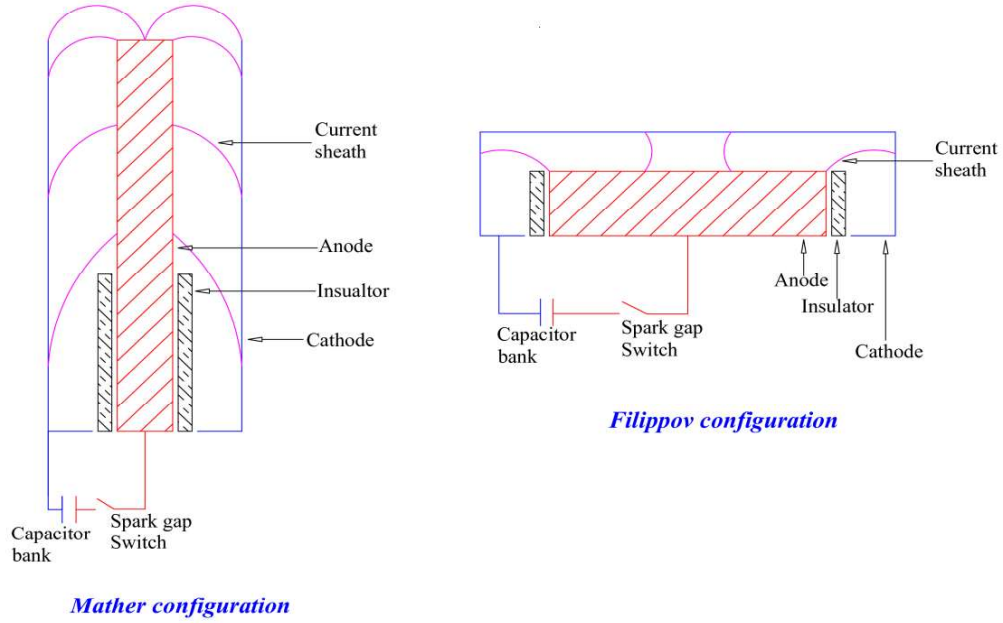

FIG.1.1 Schematics of Mather and Filippov type plasma focus devices.

Even though they are different in aspect ratio, they exhibit similar dynamics and radiation emission characteristics such as scaling laws for neutron emission, characteristic emission of ions and electrons, X-rays and other electromagnetic radiations. But, Mather type has been more popular over Filippov type due to relatively simple design, convenient access to various diagnostics and distinguishable phases of current sheath dynamics. The dynamics of plasma focus and its radiation characteristics have been discussed in subsequent sections.

1.2 Plasma focus device dynamics

Working of the plasma focus device from initial electrical discharge to acceleration and then finally compression into the form of a dense and hot plasma column is divided in three distinct phases:

(a) Breakdown,

(b) Axial acceleration phase or axial rundown, and

(c) Radial compression

Significant features of the three phases are discussed in brief below.

1.2.1 Breakdown phase

The breakdown phase is considered as the most crucial phase of plasma focus dynamics as it sets the stage for plasma focus formation. The electrical breakdown in gas (a few mbar) occurs when a pulse high voltage (a few kV to a few ten kV) is applied between the electrodes of the plasma focus device using capacitor bank. A schematic of plasma focus device dynamics is presented in fig. 1.2. The anode and cathode are at high voltage and ground respectively. Electric field intensity is estimated to be highest in the region between the edge of the cathode and the insulator. The breakdown is initiated by the free electrons present in the region near the edge of the cathode. Free electrons accelerate towards insulator and ionize the gas molecules along the path. Once the breakdown is initiated, ionization avalanche is formed and subsequently number of charge particles grows exponentially according to Townsend law [Braithwaite et al. 2000, Lisovskiy et al. 2000] for electrical gas breakdown. A uniform sheath of ionized gas (known as “current sheath” or “plasma sheath”) gas is quickly formed through sliding discharge over surface of the insulator and this bridges the gap between two electrodes. Subsequently, this provides the lowest resistance path for the current to flow.

It has been observed through different diagnostics such as image converter camera, magnetic probe, Rogowski coil, that formation of current sheath depends on many factors like the insulator, electrode-insulator configurations, polarity of electrodes, and filling gas [Bruzzone et al. 1993, Donges et al. 1980]. For optimized conditions, uniform current sheath is observed to be formed over the insulator surface through sliding discharge which is essentially required for strong plasma pinching. Mather [1965] and Kies et al. [1986] independently observed that a few initial discharges

are always required to form a uniform current sheath. The possible reason is that during these conditioning discharges the micro-cracks over the surface of the insulator are filled with metal vapors of electrode material. The metal vapor increases the surface conductivity of the insulator which in turn helps in the formation of the uniform current sheath. After some time (typically 50 - 500 ns, depending on plasma focus device parameters), the current sheath detaches from the insulator surface due to the Lorenz force ($\mathbf{J} \times \mathbf{B}$) in an inverse pinch manner. This is the end of the breakdown phase and the focus formation process enters in to the second phase i.e. the axial run-down phase.

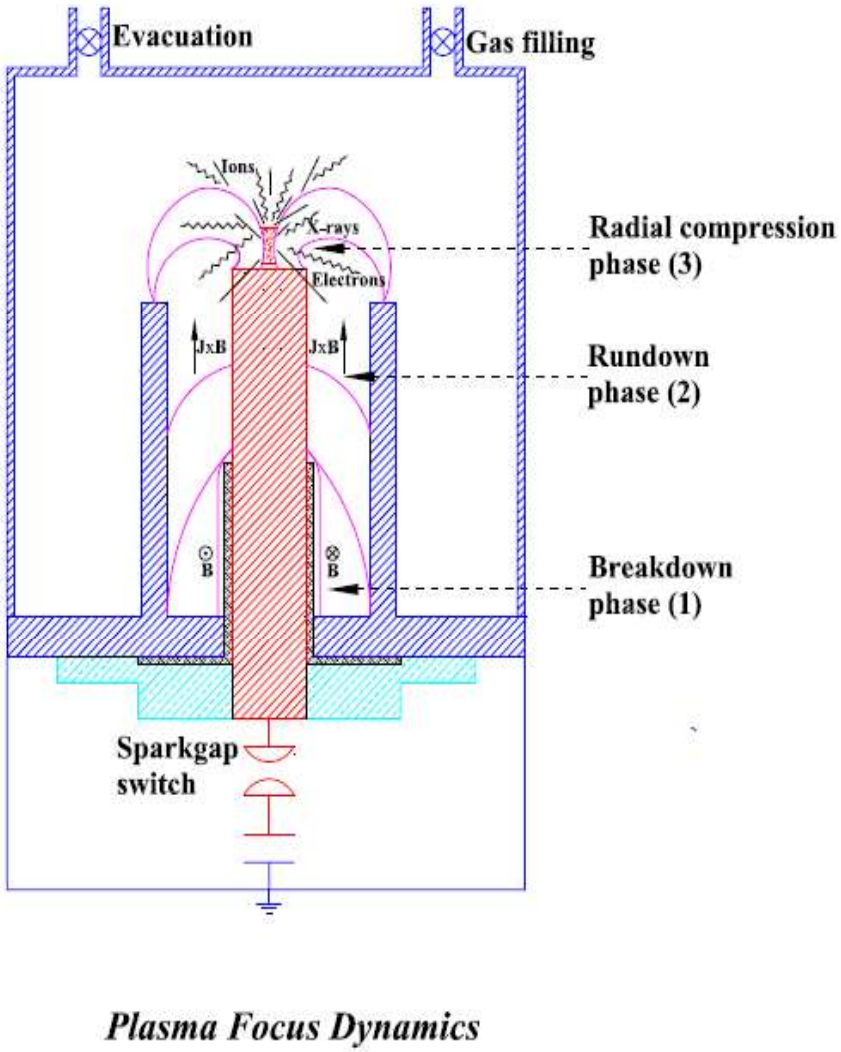

FIG. 1.2 Schematic of plasma focus device dynamics

1.2.2 Axial acceleration phase

The axial acceleration phase (or axial run-down phase) starts after arrival of the current sheath at the inner wall of the cathode. Thereafter, the current sheath is axially accelerated along the electrodes axis by the axial component ($\mathbf{F_z}$) of the $\mathbf{J} \times \mathbf{B}$ force and simultaneously pushed radially outward by the radial component ($\mathbf{F_r}$). As the $\mathbf{J} \times \mathbf{B}$ force has $1/r^2$ dependence, the current sheath evolves into a parabolic shape. The axial component is stronger near the anode and it results into higher acceleration close to the anode as shown in fig. 1.2. At the end of the axial phase, the current sheath sweeps around the end of the anode in radially inward direction whereas it continues moving up axially due to the radial and the axial components of the $\mathbf{J} \times \mathbf{B}$ force respectively.

The current sheath in axial acceleration phase is reported to be a double layered structure consisting of an ionization front and a magnetic piston [Bernard et al. 1998]. It is pushed by the magnetic piston to a supersonic speed that produces shock which subsequently heats and compresses the neutral gas in its front. Therefore, the sheath has a complex structure which includes a compressed and hot ionizing region, a plasma region carrying the current and a nearly vacuum magnetic field region behind this.

Various diagnostic techniques such as magnetic probe measurement, Schlieren imaging, shadowgraphy, interferometric investigations, and image converting camera have been employed for characterizing the axial acceleration phase. Axial sheath velocities ranging from 1.5 to 15 cm/μs have been measured and the thickness of the current sheath structure is 1 to 4 cm, for a wide energy range of plasma focus devices [Krompholz et al. 1981, Herold et al. 1989, Mather 1965]. Thickness of the current sheath and its axial velocities depend on various factors such as capacitor bank characteristics, plasma focus geometries, and filling gas pressure. The dynamics of the current sheath and its structure have been theoretically described by the "snowplow model" [Basque et al. 1968].

The axial acceleration phase is important in two aspects for a strong plasma focus formation (i) the time at which the moving current sheath reaches at the electrode axis, and (ii) structure i.e. (r, z)

profile of the current sheath. The time to reach the current sheath at electrode axis should match to the discharge current quarter time-period and this is common requirement to all pinch devices enabling them in maximization of energy transfer from the capacitor bank to the plasma at the time of pinch. The second aspect includes thin and symmetric (r, z) profiles of the current sheath.

1.2.3 Radial compression phase

The radial compression phase starts with the sweeping of current around the tip of anode in the radially inward direction as shown in fig. 1.2. This phase typically lasts for a few tens of nanoseconds to a few hundred nanoseconds depending on the plasma focus device parameters. This phase is rich in underlying science due to its extremely high energy density, transient nature and for being a copious source of intense electromagnetic radiations, high energy electrons, ions and nuclear fusion products (neutrons, protons, tritons and helium ions in case of deuterium or deuterium-tritium mixture as filling gas). Radial compression phase can further be divided into four sub phases namely compression phase, quiescent phase, unstable phase, and decay phase.

1.2.3.1 Compression Phase

The compression phase begins with the sweeping of current sheath around the end of anode and it ends with compression of the sheath to the minimum radius (r_{min}) with plasma density at its maximum (~10^{19} - 10^{20} cm^{-3}) [Mather 1965]. The current sheath collapses radially and axi-symmetrically in a non-cylindrical, funnel shaped profile [Bernard et al. 1998]. The radial compression velocity is in 6 - 60 cm/μs range and depend mainly on the current density, geometry of electrodes, filling gas pressure and current sheath structure [Krompholz et al. 1981, Herold et al. 1989, Mather 1965]. The instant at which plasma sheath compresses to its minimum radius is taken as reference point for the maximum compression of plasma i.e. when $r = r_{min,}$ $t = 0$. At the end of the compression, the pinch column forms and stagnates for a brief period. The diameter and the length of

the compressed plasma column are typically about $1/10^{th}$ and 1/2 of the anode radius respectively at the optimum operation conditions [Lee et al. 1996].

The temperature and density of plasma column are estimated using Bennett relation. Assuming radial pressure (magnetic and kinetic plasma pressure) equilibrium conditions at the time of the pinch, the temperature depends on the current (I) and line density N i.e. $T \sim I^2/N$. This indicates that lower the line density, higher will be the temperature. The magnetic field at this stage starts diffusing into the plasma column and leads to an anomalous resistance. In addition, impedance of the system increases due to increase in the inductance because of rapid radial compression of plasma sheath. Correspondingly, the sharp spike and the dip are observed in the voltage and current derivative signals respectively.

1.2.3.2 Quiescent phase

This phase marks the beginning of the expansion of the pinch plasma column. The plasma column expands in the radial as well as in the axial direction. The rate of expansion in radial direction is limited by the confining magnetic pressure. But due to funnel shape of the current sheath, it continues to expand/accelerate in the axial direction leading to formation of an axial shock front.

Earlier in compression phase, the sharp change in plasma inductance due to rapid compression of the current sheath induces high electric field in the plasma column. This electric field accelerates the ions and the electrons in the opposite direction, leading to formation of a “plasma diode”. The relative drift velocity between electrons and ions increases and approaches the electron thermal velocity. This is the condition for the onset of the micro instabilities such as the electron cyclotron and various other forms of beam-plasma instability [sausage (m = 0) and kink instability (m = 1)] [Vikhrev et al. 1993, Comisar 1969]. Due to sausage instability, the plasma column compresses and then expands repeatedly before breaking up. The time between the first compression and onset of sausage instability can be defined as the pinch lifetime t_p.

1.2.3.3 Unstable phase

During unstable phase, the pinch plasma column disrupts by the rapid development of instabilities. This phase is the richest in terms of associated phenomenon such as soft and hard X-ray emission, fast ions and electrons and fusion products. Due to the growth of m = 0 instabilities, the induced electric field gets enhanced and this accelerates the electrons and ions towards and away from the anode respectively. The accelerated ions act as an ionization wave front which moves with velocities as high as 120 cm/μs (deuterium ions in deuterium gas) [Bernard et al. 1975, Mather 1965]. This ionization front overtakes the axial shock front (formed due to continued axial expansion of the plasma column during the quiescent phase). The beginning of the ionization front coincides with the start of the hard X-rays and the neutron pulses.

1.2.3.4 Decay Phase

The last phase of radial compression and also the last stage of the plasma focus dynamics is the decay phase. During the decay phase, a very large, hot and thin plasma cloud is formed due to the complete breaking of the plasma column. A large amount of Bremsstrahlung radiation is emitted during this phase. The soft X-ray emission rises abruptly during the decay. At this stage, the neutron pulse which started at the beginning of the unstable phase, reaches its peak value.

1.3 Plasma focus radiations

As mentioned, plasma focus is a copious source of pulse energetic radiations including neutrons, X-rays, electrons and ions. They are emitted for a time duration of a few 10s ns to a few 100s ns. Their mechanisms of emission have been studied in detail but it is yet to be understood fully. Their general emission characteristics such as yield, pulse duration, energy spectrum and their correlation to plasma focus parameters viz. electrode geometry and dimension, capacitor bank energy, peak current etc. have been discussed in the following sections.

1.3.1 Neutrons

The plasma focus device is one of the most efficient pulsed sources of neutrons when filled and operated with deuterium or mixture of deuterium and tritium gas. Using deuterium or deuterium-tritium mixture gas, plasma focus devices produce fusion neutrons of ~2.45 MeV and ~14.1 MeV. Basic nuclear fusion reactions through which neutrons produced are:

$$^{2}_{1}D + {}^{2}_{1}D = {}^{3}_{1}T\ (1.01\ MeV) + {}^{1}_{1}p\ (3.03\ MeV)$$

$$^{2}_{1}D + {}^{2}_{1}D = {}^{3}_{2}He\ (0.82\ MeV) + {}^{1}_{0}n\ (2.45\ MeV)$$

$$^{2}_{1}D + {}^{3}_{1}T = {}^{4}_{2}He\ (3.52\ MeV) + {}^{1}_{0}n\ (14.06\ MeV)$$

The cross section for D - T fusion reaction is high compared to D - D fusion reaction at a given temperature [Bosch et al 1992]. Hence, the neutron yield is estimated to be enhanced by approximately two orders of magnitude (~100) when operated with D - T mixture gas instead of pure deuterium gas.

The probabilities of occurrences of first two nuclear reactions above are equal and half i.e. tritium produced in the D (d, p) T reactions are same as that of neutrons produced in the D (d, ^{3}He) n reactions. At typically reported maximum neutron yield of 10^{12} neutrons per pulse [Gribkov et al. 2007], same number of tritium is expected to generate which is too small in number to further cause D - T fusion. Hence, probability of occurrence of D - T fusion reactions would be insignificant as compared to D - D when deuterium is used as the filling gas.

Various mechanisms were proposed to explain the intense bursts of neutrons (i) Thermonuclear mechanism (ii) Quasi-thermonuclear (or “moving boiler”) mechanism and (iii) Beam-target mechanism. In thermonuclear mechanism, the neutrons are produced by thermal collision between deuterons (Maxwellian distribution) in the bulk of pinch plasma column. The rate equation for thermonuclear fusion yield can be described as:

$$Y_{th} \cong \frac{{n_d}^2}{2} < \sigma v > V_p t_p \quad \textbf{(1.1)}$$

Here, n_d is the deuterium ion number density in pinch plasma column, V_p is the volume of the pinch plasma column, t_p, is the pinch lifetime and <σv> is the average of fusion cross section multiplied with relative velocity of two particles over all the temperature T.

At the beginning of plasma focus research, thermonuclear mechanism of neutron production was considered [Mather et al. 1971]. However, the measured neutron yield and its anisotropy (ratio of neutron flux along and perpendicular to the anode axis) do not match the estimated values using the experimentally observed values of pinch density, temperature, volume and lifetime. Forrest et al. [1974] performed ion and electron temperature measurements through laser scattering and found that the temperature of Deuterium ions (T_i) ≤ 1 keV, was too low for a purely thermonuclear interpretation of neutron production. Moreover, the average neutron energy in the axial direction is also found to be more than 2.45 MeV which suggests the presence of non-thermal mechanism [Castillo et al. 2000, Milanese et al. 1978].

To explain the measured anisotropies, "moving boiler" or quasi-thermonuclear mechanism was proposed [Willenborg et al. 1976]. In the "moving boiler" or quasi-thermonuclear mechanism, neutrons are produced by a moving Maxwellian distribution of deuterium ions. Gentilin et al. [1979] performed experiments on low energy Mather-type plasma focus devices and concluded that beam-target is the dominant mechanism of neutron production. Michel et al. [1974] also concluded that the low energy deuterons (< 50 keV) contribute mainly in the neutron production. Tiseanu et al. [1994] concluded that in a small energy plasma focus device, the medium energy deuterons (50 - 100 keV) with a relatively broad angular distribution are responsible for most of the neutron yield.

The rate equation for beam-target fusion yield is given as:

$$Y_{b-t} \cong n_d n_0 (r_p^2 z_p) \sigma v t_p \quad \textbf{(1.2)}$$

Here, n_d is the number density of deuterium ion beam, n_0 is the background ion density, r_p and z_p are radius and length of pinch plasma column respectively, σ is the fusion reaction cross section, v is ion beam speed and t_p is the beam-target interaction time which is assumed as proportional to the confinement time of the pinch plasma column.

The ratio of neutron flux at any angular direction (θ), measured from the electrode axis in downstream, to the radial direction (90°) is given by the relation [Shyam 1981]:

$$\frac{Y_\theta}{Y_{90}} \cong \left(1 + 1.3{E_d}^{1/2} \cos\theta\right) \qquad (E_d << 2.45\text{MeV}) \qquad \textbf{(1.3)}$$

here E_d (in MeV) is deuterium ion beam energy. The neutron flux anisotropy i.e. ratio of neutron flux in the axial (0°) to that of in the radial direction (90°) is

$$\frac{Y_0}{Y_{90}} \cong (1 + 1.3{E_d}^{1/2}) \qquad \textbf{(1.4)}$$

The neutron flux anisotropy has typically been reported to be ~ 1.2 - 3, for a wide energy range of plasma focus devices operating in the kJ to MJ range [Koh et al. 2005, Zakaullah et al. 1998, Schmidt et al. 2002]. Stygar et al. [1982] concluded that most of the neutrons produced are correlated to 30 - 300 keV energy deuterium ions, with peak at around 100 keV. For deuterium beam energy of 100 keV, anisotropy comes out to be ~ 1.4.

The measurement of neutron yield from plasma focus devices operating at energies from sub-kilojoule range to hundreds of kilo-joule range suggests that it follows empirical scaling laws w. r. t. plasma focus device parameters i.e. operation energy (E_0), peak discharge current (I_0) and the current flowing through the plasma during focus called the pinch current (I_p). The scaling laws are expressed as [Schmidt 1980]:

$$Y_n = 10\,E^2 \quad \text{(E in Joule)} \tag{1.5}$$

$$Y_n = 1.7 \times 10^{-10}\, I_0^{3.3} \quad (I_0 \text{ in Amp}) \tag{1.6}$$

$$Y_n = 1.7 \times 10^{-13}\, I_p^{4} \quad (I_0 \text{ in Amp}) \tag{1.7}$$

The scaling exponent shows variations in some devices. [Decker et al. 1980, Krompholz et al. 1981, Lee 2008] The variation in the energy scaling exponent is mainly on account of the operating parameters of the plasma focus device, which should be optimized in terms of external inductances, charging voltage, electrode geometry, filling pressure etc. The variation in the peak discharge current scaling exponent is due to the variation in leakage current (peak discharge current – current flowing through plasma). Values of the pinch current (current flowing through plasma in radial compression phase) differ distinctly from device to device, even in a particular device operated at same energy and delivering same peak discharge current. This variation in pinch current is mainly due to snowplow efficiency and electro-dynamical processes of the plasma focus device. Therefore, pinch current (I_p) is considered to be the most appropriate parameters for scaling of the neutron yield. It is used to be numerically computed using Lee model code [Lee et al. 1996].

The scaling laws hold up to a few hundred kJ of the bank energy. Beyond this, neutron yield saturates or even decreases [Gourlan et al. 1978, Herold et al. 1989] with energy in spite of best efforts to optimize various parameters. The saturation effect has been observed at ~170 kJ in a 360 kJ device [Jerzykiewicz et al. 1984] and above ~300 kJ in a 500 kJ device [Herold et al. 1988]. It is believed that at higher energy the impurities entering into the plasma from the electrode and insulator [Herold et al 1988] spoil the plasma sheath. Moreover, at high energies the leakage current across the insulator [Oppenlander et al. 1977, Gourlan et al. 1978] most likely increases, thus reducing the pinch current. These factors result in deterioration of the neutron yield. It still remains to find the exact reason for neutron yield saturation at high bank energies.

1.3.2 X-rays

X-rays are produced in plasma focus for a time duration ranging from a few nanoseconds to a few hundred nanoseconds. The energy spectrum of X-rays is of wide range, from a few hundreds of eV to several hundreds of keV. The X-rays can broadly be categorized as soft (a few tens eV to several keV) and hard (≥ 10 keV) based on the energies. Soft X-rays are quasi-equilibrium thermal radiation from pinch plasma and hard X-rays are non-thermal radiation from electron beam interacting with non-plasma targets (plasma focus anode).

It has been inferred from various reports that soft X-ray emitting region is near the anode tip and it is cylindrical in shape [Rout et al. 1989; Choi et al. 1989]. Its dimensions vary from below 1 mm to over 10 mm in diameter and axial length from a few mm to a few cm. Spectral filtering of the X-ray image reveals a fine structure presenting intensely radiating small macroscopic entities called as "hot spots" or "micropinches" inside and along the axis of the pinch.

Rout et al. [1989] reported the observation of helical structure and hot spots using the fast optical camera and X-ray pinhole camera with Beryllium filters in a 3 kJ Mather-type plasma focus device operated with deuterium gas. They observed two pulses of X-rays, each of 10s of ns duration and separated by a few 10s of ns. The first pulse was observed to be emitted at the time of pinch formation while second pulse was observed after the onset of sausage instability. The maximum estimated temperature during the first pulse was ~ 0.1 keV, while it was ~ 1 keV during the second pulse. This indicates that the helical filament, hot spots and other areas of high temperature were produced during the second X-ray pulse i.e. after onset of sausage instability.

Choi et al. [1989] reported "hot spots" with typical dimension of about 100 μm which occur within 5 ns of first compression during the period of the stable phase of the pinch. They concluded that formation of "hot spots" are not concomitant to m = 0 instabilities which disrupt the pinch column. Favre et al. [1992] investigated the temporal and spatial characteristics of the X-ray emission

in a 3 kJ plasma focus operated with hydrogen-argon mixture. They observed two soft X-ray pulses corresponding to two successive compressions of the plasma column.

The energy spectrum of hard X-rays is determined by the accelerated electron beam. Time-resolved measurements show that the energy spectrum follows the power law: $dN/dE \sim E^{-\alpha}$, with $\alpha = 2 - 4$, E in keV and N_{HX} in photons per cm^2, for 50 - 500 keV energy range [Bostick et al. 1972, Lee et al. 1971]. On correlating hard X-ray emission with neutron emission when deuterium used as the operation gas, it was observed that total neutron yield was high when the X-ray emission was high.

The X-ray emission characteristics strongly depend on the plasma focus device parameters such as filling gas composition and pressure, capacitor bank energy, peak discharge current, electrode material and its shape. Among them, the composition of the gas and pressure has the strongest influence. For an X- rays optimized plasma focus device, the scaling law for X-ray yield Y_X as a function of peak discharge current (I_0) and the pinch radius r_p, is empirically given as [Serban et al. 1997]

$$Y_X = \frac{{I_0}^4}{r_p^2} \tag{1.8}$$

However, the exact mechanisms by which high intensity X-rays are emitted in the plasma focus are still not clear and experimental works are underway to optimize X-ray production for practical applications.

1.3.3 Electrons

Electrons are accelerated to high energies up to MeV in the unstable phase of plasma focus. Acceleration of the electrons to high energies is linked with m = 0 instabilities [Vikhrev et al. 1993, Lee et al. 1971, Paassen et al. 1970]. The growth of this instability in plasma column during unstable phase enhances the induced electric field. This enhanced electric field together with the magnetic field accelerates the electrons towards the anode. The accelerated electrons approach relativistic energies

before collision with anode. Electron beam interaction with the metallic anode was proposed as the source of hard X-ray emission [Newman et al. 1975]. Another explanation for energetic electrons is that the plasma resistance in pinch column increases rapidly, while the plasma current remains constant. Therefore, the voltage along the pinch column increases, so that the electric field along the axis also increases [Bernard et al. 1998].

Electron emissions have been studied in different plasma focus operating at energies ranging from kJ to MJ. Most experiments employ the X-ray emission from a target (which could be the anode itself) for electron beam measurement. The direct measurements of the electron beam use Faraday cups, magnetic spectrometers, nuclear emulsions among others.

Stygar et al. [1982] scaled the electron beam current as a function of pinch current: $I_p^{(2.9 \pm 0.5)}$. A total electron beam current of 17 kA was estimated from a 12.5 kJ plasma focus device. Beckner et al. [1969] studied the X-ray spectral distribution and proposed a scaling law as $I(E) \sim E^{-\alpha}$, with $\alpha = 2$ and $7 < E < 29$ keV. From time-integrated energy measurements with nuclear emulsions for fast electrons (30 – 400 keV), the energy spectrum was also described by the scaling law with $\alpha = 2.5 - 5$.

Using a Perspex Cerenkov detector on a 28 kJ / 60 kV Mather-type plasma focus device operated with hydrogen (5 torr) and Argon (0.15 torr), Choi et al. correlated the electron beam to plasma focus dynamics at nanosecond resolution. The relativistic electron beam (REB) with energy above 180 keV occurs at the time of maximum compression in contrast to various reports which states that it is concomitant to sausage (m = 0) instability [Choi et al. 1990]. It can be inferred from these reports that emission mechanism of electrons is still not clear as it requires to be probed further.

1.3.4 Ions

The plasma focus device is an intense source of ions having wide energy range varying from a few eV up to MeV. They are accelerated along axially upward direction opposite to that of electrons. Acceleration of ions to high energies and its study are of vital importance in view of the underlying

physics as well as various applications [Jiang et al. 2001, Rawat et al. 1993, Kant et al. 1998, Srivastava et al.1996, Roshan et al. 2014]. The emissions of ions over wide range of operation energies, filling gases, and electrode configurations have been characterized experimentally as well as theoretically in the past. Various mechanisms have been proposed for ion acceleration and several theoretical as well as computational models related to ion production and acceleration have been developed [Bostick et al. 1993, Bernstein et al. 1972, Jager et al. 1987, Zambreanu et al. 1992]. Most acceptable explanation is that the generation of high electric field which results from constriction of plasma column due to development of magneto-hydrodynamic instabilities mainly the m = 0 instability [Haruki et al. 2006] or from the degradation of the plasma conductivity by strong turbulences [Haines 1983]. Other proposed models assume collective acceleration of ions [Gary et al. 1974], wave particle interactions [Hsieh et al. 1976], multiple reflections from the magnetic piston layer [Deutsch et al.1988], and formation of a plasma diode [Goldstein et al.1975]. The motion of the medium energy deuterons is well described by the so called "gyrating particle model" [Jager et al. 1987] which also explains the neutron generation.

Although some qualitative conclusions are in good agreement with the experimental data, none of the above-mentioned models can explain all the characteristics of ion beam emission and evolution. Various reports on ion emission and its characteristics are often found to be contradictory. Some of the recent results as well as earlier reported results on ion emission characteristics of different plasma focus devices are briefly described below.

Gullickson et al. [1978] reported that the maximum ion emission occurs along the electrode axis (0 deg.) and they found that ion fluence decreases gradually with increasing angle. On the contrary, Sadowski et al. [1988] observed a distinct drop of ion fluence at 0 deg. However, Kelly et al. [1996] measured angular distribution of fast deuterons in a 5 kJ plasma focus and observed that the number of ions detected in the 90 deg. direction is approximately 50% of the corresponding number in the 0 deg. direction.

It has been reported that the energy spectrum of ion beam follows the power law: $\frac{dN}{dE} \alpha E^{-x}$, where E is the ion energy, N is the ion number and value of "x" ranges between 2 to 5 [Stygar et al. 1982, Sanchez et al. 1997]. Stygar et al. [1982] measured the mean deuterium ion fluence using the SSNTD technique in a plasma focus device operating at 12.5 kJ. The deuterium ion fluence was estimated to be $(6 \pm 2) \times 10^{14}$ cm^{-2} over a 15 cm diameter plate kept 20 cm away from the focus.

Mohanty et al. [2005] used multiple Faraday cup assembly to measure angular distribution of nitrogen ion beam in a low energy 2.2 kJ plasma focus device. They found that the ion flux strongly depends on the filling gas pressure. Further, they observed that the ion flux is minimum at 0 deg. i.e. along the anode axis and maximum at 5 deg. They attributed this to trapping of ions with the conical tunnel of the collapsing current sheet and lack of ions within a hole due to finite Larmor radius in an azimuthally magnetic field around the pinch column.

Bhuyan et al. [2011] measured the temporal and spatial profiles of neon ion beam in a 2.2 kJ plasma focus device using Faraday cup and CR39 nuclear track detectors. They have characterized the neon ion beam for different filling pressures as well as at axial and angular positions. Ion flux was found to be maximum at 25 deg. from electrode axis. It was found that the most probable ion densities at 0, 20, and 25 deg. were around 9.7×10^{19}, 11×10^{19}, and 15.5×10^{19} m^{-3}, respectively with the most probable energy of around 57, 20 and 12 keV respectively.

Habibi et al. [2016] reported the measurement of angular distribution of argon ion beam in a 3.5 kJ plasma focus device using different shapes of anodes i.e. cylindrical with a flat and hollow top and cone with a flat and hollow top at various filling pressures. They found that the angular distribution of ions was significantly reduced at angles higher than 11 deg. and the maximum ion emission was between 0 and 11 deg. The maximum ion flux of about 5.57×10^{12} ions/steradian was obtained with cylindrical-flat anode tip that increases to 9.82×10^{12} ions/steradian per shot for cone-flat anode tip. They attributed the reason behind more ion flux in cone-flat anode compared to cylindrical-flat anode tip to the fact that the small diameter in the case of conical anode tip resulting

into short radial compression phase and therefore enhance induced electric field. This has resulted into more acceleration of ions toward the Faraday cup detectors.

Lee et al. [2012] numerically computed ion emission characteristics for a range of plasma focus devices working at different capacitor bank energies ranging from 0.4 to 280 kJ. The computed ion fluence was (2.4 -7.8) $\times 10^{20}$ m^{-2} and it was found to be independent of stored electrical energy.

It is clear from the various reports that mechanism of ion emission and its characteristics are yet to be understood fully. It needs further study for understanding of plasma process as well as for applications.

1.4 Scope of thesis

Mechanism of radiation emissions is a matter of further investigation as none of the existing models is able to explain its general emission characteristics. Although, its emission mechanism is yet to be fully understood, they have found applications in many areas as explained earlier. In quest of understanding its emission mechanism and for various applications, plasma focus devices operating at a few joules to several hundred kJ are being developed and optimized. In the past few decades, miniaturization of plasma focus devices is of major interest due to its portability and efficient neutron emission at a low cost. The efforts are being made to construct sealed tube based plasma focus devices and improving associated pulse power systems to make it commercially viable for many of applications which requires operation away from the regular activity area. Moreover, through the improvement in associated technologies, neutron flux of the same order to that of expensive accelerator based sealed tube neutron generator can be achieved by operating them repetitively at high repetition rate. This requires a lot more research and dedicated efforts.

In view of the above, two different devices, “SPF1-P2”and “PF-P5” for operation at 200 J and 500 J respectively. The SPF1-P2 is a sealed tube plasma focus. This device is operated continuously for 200 shots without purging deuterium gas for a time spanning over 200 days. Another semi-sealed

tube but of larger volume based PF-P5 device is developed. This device is repetitively operated at a repetition rate of 10 Hz. The time average neutron yield is observed to be enhanced by a factor approximately equal to number of repetitive pulses.

In addition, three different devices, "PF-2", "MEPF-12" and "MEPF-17" devices are developed and characterized for operation at 2 kJ, 11.5 kJ and 17 kJ respectively. All three devices are of squirrel-cage geometries. The PF-2 and MEPF-12 devices are using parallel-plate transmission lines with one end of the spark electrode is connected to the capacitor bank collector plate and other end is interfaced to the anode of plasma focus. The MEPF-17 device is using coaxial cables. All the three devices have been optimized for maximum radiation output through variations of parameters such as electrodes dimensions, insulator, filling pressures and operation energies. They are used for applications in material science as an ion and plasma source such as irradiation on fusion reactor relevant materials and thin film depositions. It is demonstrated that pulsed neutrons are useful in different applications such as assaying of fissile materials and short-lived radioisotopes production as well as their half-life measurements.

The present work includes conceptualization, development and optimization of five different plasma focus devices mentioned above. The radiation emissions with emphasis on ion emissions are studied in details. This further includes the various applications using different plasma focus devices.

References:

1. "Neutron Production in Linear Deuterium Pinches", Anderson O. A., Baker W. R., Stirling A. C. et al., *Phys. Rev.,* **1958**, *110(6)*, 1375 – 1387.
2. "Observations of high-density effects on spectral line shapes in a dense ($n_e > 10^{18}$ cm^{-3}) z-pinch discharge", Baker E. A. M. and Burgess D. D., *J. Phys. B*, **1979**, *12(13)*, 2097 - 2113.
3. "Comparison of a two-dimensional snowplough model with experiment", Basque G., Jolas A., Watteau J. P., *Phys. Fluids,* **1968**, *11*, 1384-1386.

4. "Dominant source of soft x radiation from coaxial discharge tubes", Beckner E. H., Clauthiaux E. J. et al., *Phys. Fluids,* **1969**, *12*, 253-254.
5. "Feasibility analysis of a plasma focus neutron source for BNCT treatment of transplanted human liver", Benzi V., Mezzetti F., Rocchi F. et al., *Nucl. Instrum. Methods Phys. Res. B,* **2004**, *213*, 611–615.
6. "Experimental studies of the plasma focus and evidence for nonthermal processes", Bernard A., Coudeville A., Jolas A. et al., *Phys. Fluids,* **1975**, *18*, 180-194.
7. "Neutron energy and flux distributions from a crossed-field acceleration model of plasma focus and z-pinch discharges", Bernstein M. J. and Comisar G. G., *Phys. Fluids,* **1972**, *15*, 700-707.
8. "Inertial-confinement fusion with lasers", Betti R., Hurricane O. A., *Nature Phys.,* **2016**, *12*, 435-448.
9. "Temporal and spatial study of neon ion emission from a plasma focus device", Bhuyan M., Neog N. K., Mohanty S. R. et al., *Phys. Plasmas,* **2011**, *18*, 033101(1-8).
10. "First studies of plasma confined in a toroidal heliac", Blackwell B. D., Hamberger S. M., Sharp L.E. et al., *Nucl. Fusion,* **1985**, *25*, 1485-1490.
11. "Improved formulas for fusion cross-sections and thermal reactivities," Bosch H. S., Hale G. M., *Nucl. Fusion,* **1992**, *32*, 611-631.
12. "X-ray fine structure of dense plasma in a co-axial accelerator", Bostick W. H., Nardi V., Prior W., *J. Plasma Phys.,* **1972**, *8*, 7-20.
13. "Time resolved energy spectrum of the axial ion beam generated in plasma focus discharges", Bostick W. H., Kilic H., Nardi V. et al., *Nucl. Fusion* **1993**, *33*, 413-420.
14. "The initial phase in plasma focus devices", Bruzzone H., Vieytes R., *Plasma Phys. Control. Fusion,* **1993**, *35*, 1745-1754.
15. "X-ray spectra from exploded-wire plasmas", Burkhalter P. G., Dozier C. M., and Nagel D. J., *Phys. Rev. A*, **1977**, *15(2)*, 700 - 717.

16. “Evidence of thermal and non-thermal mechanisms coexisting in dense plasma focus D-D nuclear reactions,” Castillo F., Milanese M., Moroso R. et al., *J. Phys. D: Appl. Phys.* **2000***, 33*, 141.

17. “Studies of the spatial and temporal evolution of a dense plasma focus in the X-ray region”, Choi P., Wong C. S., Herold H., *Laser Particle Beams,* **1989**, *7*, 763-777.

18. “Characterization of self-generated intense electron beams in a plasma focus”, Choi P., Deeney C., Herold H. et al., *Laser Particle Beams,* **1990**, *8*, 469-476.

19. “Spectroscopic measurements on vacuum spark plasmas”, Cilliers W. A., Datla R. U. and Griem H. R., *Phys. Rev. A*, **1975**, *12(4)*, 1408 - 1418.

20. “Feasibility study of a hybrid subcritical fission system driven by Plasma-Focus fusion neutrons”, Clausse A., Soto L., Friedli C. et al., *Annals Nucl. Energy,* **2015**, *78*, 10–14.

21. “Hydromagnetic Instabilities in the Dense Plasma Focus,” Comisar G. G., *Phys. Fluids,* **1969**, *12*, 1000.

22. “Current and neutron yield scaling of fast high voltage plasma focus”, Decker G., Flemming L., Kaeppeler H. J. et al., *Plasma Phys.,* **1980**, *22*, 245-260.

23. “Ion acceleration and runaway in dynamical pinches”, Deutsch R., Kies W., *Plasma Phys. Control. Fusion,* **1988**, *30*, 263-276.

24. “The breakdown phase in a coaxial plasma gun”, Donges A., Herziger G., Krompholz H. et al., *Phys. Letter. A.,* **1980**, *76A*, 391-392.

25. “X-ray emission in a small plasma focus operating with H2-Ar mixtures”, Favre M., Lee S., Moo S. P. et al., *Plasma Sources Sci. Technol.,* **1992**, *1*, 122.

26. “High temperature dense plasma in a non-cylindrical Z-pinch”, Filippov N. V., Filipova T. I., Vinogradov V. P., *Nucl. Fusion (suppl.),* **1962**, *2*, 577-587.

27. “Measurement of the ion temperature in the dense plasma focus by laser beam scattering”, Forrest M. J., Peacock N. J., *Plasma Phys.,* **1974**, *16*, 489-498.

28. “Comments on Neutron Production Mechanisms in a Dense Plasma Focus”, Gentilini A., Maisonnier C., Rager J. P. et al., *Comm. Plasma Phys.,* **1979**, *5*, 41.

29. “Ion-Induced Pinch and the Enhancement of Ion Current by Pinched Electron Flow in Relativistic Diodes”, Goldstein S. A., *Phys. Rev. Lett.,* **1975**, *35*, 1079-1082.

30. “Energy confinement scaling in tokamaks: some implications of recent experiments with ohmic and strong auxiliary heating”, Goldstone R. J., *Plasma Phys. Control. Fusion,* **1984**, *26*, 87-103.

31. “Recent progress in 1-MJ plasma focus dynamics and scaling for neutron production,” Gourlan C., Kroegler H., Maissonier Ch. et al., *Proc. 7th Int. Conf. Plasma Phys. Control. Nucl. Fusion Res., Innsbruck, Austria,* **1978**, *2,* 122.

32. “Possible applications of a hybrid thermo-nuclear energy source based on a DPF device in modern energy complexes, in nuclear technologies in a sustainable energy system”, Gribkov V. A., Tyagunov M., ed. by Bauer G.S., McDonald A., Springer Verlag, B., H., N-Y (**1983**).

33. “On various possibilities in pulsed radiation biochemistry and chemistry”, Gribkov V. A., Orlova M. A., *Radiation Environ. Biophys.,* **2004**, *43*, 303-309.

34. “PF-6 − an effective plasma focus as a source of ionizing radiation and plasma streams for application in material technology, biology and medicine”, Gribkov V. A., Dubrovsky A.V., Scholz M. et al., *Nukleonika,* **2006**, *51(1)*, 55−62.

35. “Plasma dynamics in the PF-1000 device under full-scale energy storage: II. Fast electron and ion characteristics versus neutron emission parameters and gun optimization perspectives”, Gribkov V. A., Banaszak A., Bienkowska B. et al., *J. Phys. D: Appl. Phys.,* **2007**, *40*, 3592–3607.

36. “A dense plasma focus-based neutron source for a single-shot detection of illicit materials and explosives by a nanosecond neutron pulse”, Gribkov V. A., Latyshev S. V., Miklaszewski R. A. et al., *Phys. Scripta,* **2010**, *81*, 035502.

37. “Measurements of high energy deuterons in the plasma focus device”, Gullickson R. L., Sahlin H. L., *J. Appl. Phys.,* **1978**, *49*, 1099-1105.

38. “Angular distribution of ion beam emitted from a 3.5 kJ plasma focus device using different shapes of anodes”, Habibi M., *Phys. Lett. A,* **2016**, *380*, 439–443.

39. “Ion beam formation in an m = 0 unstable z pinch”, Haines M. G., *Nucl. Instrum. Methods Phys. Res.,* **1983**, *207*, 179-185.

40. “Recent results on dense Z pinches”, Hammel J. E., Scudder D. W., and Shlachter J. S., *Nucl. Instrum. Methods Phys. Res.,* **1983**, *207*, 161 - 168.

41. “A conceptual fusion reactor based on the high plasma density Z-pinch”, Hartman C.W., Carlson G., Hoffman M. et al., *Nucl. Fusion,* **1977**, *17*, 909-917.

42. “Simulation of high-energy particle production through sausage and kink instabilities in pinched plasma discharges”, Haruki T., Yousefi H. R., Masugata K. et al., *Phys. Plasmas,* **2006**, *13*, 0821061-5.

43. “Progress in plasma focus operating up to 500kJ bank energy”, Herold H., Kaeppeler H. J., Schmidt H. et al., *Proc. 12th Int. Conf. Plasma Phys. Control. Nucl. Fusion Res., Nice,* **1988**, *2*, 587.

44. “Comparative analysis of large plasma focus experiments performed at IPF, Stuttgart, and IPJ, Swierk”, Herold H., Jerzykiewicz A., Sadowski M. et al., *Nucl. Fusion,* **1989**, *29*,1255.

45. “Coherent ion acceleration at a density gradient”, Hsieh S. L., Bloomberg H. W., Gary S. P., *J. Plasma Phys.,* **1976**, *1*, 553-562.

46. “Fast ion kinetics and fusion reaction mechanism in the plasma focus”, Jager U. and Herold H., *Nucl. Fusion,* **1987**, *27*, 407-423.

47. “Review of spheromak research”, Jarboe T. R., *Plasma Phys. Control. Fusion* **1994**, 36, 945-990.

48. “Neutron, ion and X-ray emission from a 360kJ plasma focus device,” Jerzykiewicz A., Bielik M., Jalubowski L. et al., *Proc. 10th Int. Conf. Plasma Phys. Control. Nucl. Fusion Res., London,* **1984**, *2*, 591.

49. “Ion implantation and thermal annealing in silicon carbide and gallium nitride”, Jiang W., Weber W. J., Thevuthasan S., *Nucl. Instrum. Methods Phys. Res. B,* **2001**, *178*, 204-208.

50. “Dense plasma focus energetic ions based fullerene films on a Si (111) substrate”, Kant C. R., Srivastava M. P., Rawat R. S., *Phys. Lett. A,* **1998**, *239*, 109-l 14.

51. “Ion-beam and neutron production in a low-energy plasma focus”, Kelly H., Marquez A., *Plasma Phys. Control. Fusion,* **1996**, *38*, 1931–1942.

52. “Power limits for dynamical pinch discharges”, Kies W., *Plasma Phys. Control. Fusion,* **1986**, *28*, 1645.

53. “Optimization of the high pressure operation regime for enhanced neutron yield in a plasma focus device”, Koh J. M., Rawat R. S., Patran A. et al., *Plasma Sources Sci. Technol.,* **2005**, *14*, 12-18.

54. “A scaling law for plasma focus devices”, Krompholz H., Ruhl F., Schneider W. et al., *Phys. Lett. A,* **1981**, *82*, 82-84.

55. “Hard X-ray spectrum of a plasma focus”, Lee J. H., Loebbaka D. S., Koos C. E., *Plasma Phys.,* **1971**, *13*, 347.

56. “Neutron Production Mechanism in a Plasma Focus”, Lee J. H., Shomo L. P., Williams M. D. et al., *Phys. Fluids,* **1971**, *14*, 2217.

57. “Neutron Scaling Laws from Numerical Experiments”, Lee S., Saw S. H., *J. Fusion Energy,* **2008**, *27(4)*, 292-295.

58. “Plasma focus ion beam fluence and flux—Scaling with stored energy”, Lee S., Saw S. H., *Phys. Plasmas,* **2012**, *19*, 112703(1-5).

59. "Dimensions and lifetime of the plasma focus pinch", Lee S., Serban A., *IEEE Trans. Plasma Sci.,* **1996**, *24*, 1101-1105.

60. "Low-pressure gas breakdown in uniform dc electric field", Lisovskiy V. A., Yakovin S. D. and Yegorenkov V. D., *J. Phys. D: Appl. Phys.,* **2000**, *33*, 2722–2730.

61. "Formation of a high-density deuterium plasma focus", Mather J. W., *Phys. Fluids,* **1965**, *8(2),* 366-377.

62. "Dense Plasma Focus", Mather J.M., *Methods in Experimen. Phys.*, ed. Lovberg R. H., and Griem H. R. (Academic Press, Nueva York), **1971**, *9B*, 187-249.

63. "Neutron emission from a small 1-kJ plasma focus", Michel L., Schonbach K. H., Fischer H., *Appl. Phys. Lett.,* **1974**, *24*, 57-59.

64. "Evidence of non-thermal processes in a 1-MJ plasma focus device by analyzing the neutron spectra", Milanese M. M. and Pouzo J. O., *Nucl. Fusion,* **1978**, *18(4)*, 533.

65. "Recent stellarator research", Miyamoto K., *Nucl. Fusion,* **1978**, *18*, 243-284.

66. "Development of Multi Faraday Cup Assembly for Ion Beam Measurements from a Low Energy Plasma Focus Device", Mohanty S. R., Bhuyan H., Neog N. K. et al., *Japan. J. Appl. Phys.,* **2005**, *44(7A),* 5199–5205.

67. "Industrial application of plasma focus radiation", Moreno C., Venere M., Barbuzza R. et al., *Brazillian J. Phys.,* **2002**, *32(1)*, 20-25.

68. "Production of hard x rays in a plasma focus", Newman C., Petrosian V., *Phys. Fluids,* **1975**, *18*, 547-551.

69. "Magnetic confinement fusion", Ongena J., Koch R.,Wolf R. et al., *Nature Phys.,* **2016**, *12*, 398–410.

70. "The plasma focus current in the compression phase," Oppenlander T., G. Pross, G. Decker et al., *Plasma Phys.,* **1977**, *19*, 1075.

71. "Reversed field pinch confinement physics", Ortolani S., *Plasma Phys. Control. Fusion,* **1989**, *31* 1665-1683.

72. "The magnetic mirror approach to fusion", Post R. F., *Nucl. Fusion*, **1987**, *27*, 1579-1739.

73. "Crystallization of an amorphous lead zirconate-titanate thin film with a dense-plasma-focus device", Rawat R. S., Srivastava M. P., Tandon S. et al., *Phys. Rev. B,* **1993,** *47*, 4858-4862.

74. "Short-Lived PET Radioisotope Production in a Small Plasma Focus Device", Roshan M. V., Springham S. V., Rawat R. S. et al., *IEEE Trans. Plasma Sci.,* **2010**, *38*, 3393-3397.

75. "Potential medical applications of the plasma focus in the radioisotope production for PET imaging", Roshan M.V., Razaghi S., Asghari F. et al., *Phys. Lett. A,* **2014**, *378*, 2168–2170.

76. "Observation of Helical Structure in a Low Energy Plasma Focus Pinch", Rout R. K., Shyam A., *Plasma Phys. Control. Fusion,* **1989**, *31*, 873-877.

77. "Ion emission from plasma-focus facilities", Sadowski M., Zebrowski J., Rydygier E. et al., *Plasma Phys. Control. Fusion,* **1988**, *30*, 763-769.

78. "Comparison of characteristics of pulsed ion beams emitted from different small PF devices", Sadowski M., Skladnik-Sadowska E., Baranowski J. et al., *Nukleonika,* **2000**, *45(3)*, 179–184.

79. "The thermal evolution of targets under plasma focus pulsed ion implantation", Sanchez G., Feugeas J. N., *J. Phys. D: Appl. Phys.,* **1997**, *30*, 927-936.

80. "The plasma focus- a review", Schmidt H., *Atomker. Kertech.,* **1980**, *36(3),* 161.

81. "Review of Recent Experiments with the Megajoule PF-1000 Plasma Focus Device", Schmidt H., Kasperczuk A., Paduch M. et al., *Phys. Scripta,* **2002**, *66,* 168-172.

82. "Soft x-ray emission from a small plasma focus operated in deuterium", Serban A., Lee S., *Plasma Sources Sci. Technol.,* **1997**, *6,* 78–85.

83. "Z Pinch of a Gas Jet", Shiloh J., Fisher A., and Rostoker N, *Phys. Rev. Lett.*, **1978**, *40(8),* 515 - 518.

84. “Studies on a low energy plasma focus fusion device”, Shyam A., Ph.D. Thesis, University of Bombay, India, **1981**.

85. “BRAHMMA: A compact experimental accelerator driven subcritical facility using D-T/D-D neutron source”, Sinha A., Roy T., Kashyap Y. et al., *Annals Nucl. Energy,* **2015**, *75*, 590–594.

86. “Diode like behaviour of an ion irradiated polyaniline film”, Srivastava M. P., Mohanty S. R, Annapoorni S. et al., *Phys. Lett. A,* **1996**, *215*, 63-68.

87. “Particle beams generated by a 6–12.5 kJ dense plasma focus”, Stygar W., Gerdin G., Venneri F. et al., *Nucl. Fusion,* **1982**, *22*, 1161-1172.

88. “Introduction to gas discharges”, Braithwaite St J. N, *Plasma Sources Sci. Technol.,* **2000**, *9*, 517–527.

89. “Detection of water by neutron scattering usinga small plasma focus”, Tartaglione A., Ramos R., Gonzalez J. et al., *Brazilian J. Phys.,* **2004**, *34*, 1756.

90. “Energetic and angular characteristics of the reacting deuterons in a plasma focus”, Tiseanu I., Mandache N., Zambreanu V., *Plasma Phys. Control. Fusion,* **1994**, *36*, 417-432.

91. “A new plasma confinement geometry”, Tuck J. L., *Nature,* **1960**, *4740*, 863-864.

92. “Field Reversed Configurations”, Tuszewski M., *Nucl. Fusion,* **1988**, *28*, 2033-2092.

93. “Confinement heating and stability in the ELMO bumpy torus (EBT)”, Uckan N. A., *Plasma Phys.,* **1983**, *25*, 129-160.

94. “X-Ray Spectra from Dense Plasma Focus Devices”, Van PaassenH. L. L., Vandre R. H., White R. S., *Phys. Fluids,* **1970**, *13*, 2606-2616.

95. “Miniature Plasma Focus Device as a Compact Hard X-Ray Source for Fast Radiography Applications”, Verma R., Rawat R. S., Lee P. et al., *IEEE Trans. Plasma Sci.,* **2010**, *38(4),* 652-657.

96. “Fast Neutron Activation Analysis of goldby inelastic scattering, ^{197}Au (n, n'γ) $^{197}Au^{m}$, by means of Plasma Focus device,”Verri G., Mezzetti F., Da Re A. et al., *Nukleonika,* **2000**, *45(3),* 189.

97. “Development of sausage-type instability in a Z-pinch plasma column”, Vikhrev V. V., Ivanov V. V., Rozanova G.A., *Nucl. Fusion,* **1993**, *33*, 311-321.

98. “Design and construction of a dense plasma focus device,” Willenborg D. L., Hendricks C. D., UILU-ENG-76-2557, Charged Particle Research Lab, Dept. Elec. Engg., Univ. Illinois Urbana, Illinois, **1976**.

99. “Soft X-ray optimization studies on a dense plasma focus device operated in neon and argon in repetitive mode”, Wong D., Patran A., Tan T. L. et al., *IEEE Trans. Plasma Sci.,* **2004**, *32(6),* 2227-2235.

100. “Comparative study of ion, x-ray and neutron emission in a low energy plasma focus”, Zakaullah M., Akhtar I., Waheed A. et al., *Plasma Sources Sci. Technol.,* **1998**, *7*, 206–218.

101. “An electrodynamical model for the ion behaviour in the final plasma focus stages”, Zambreanu V., and Doloc C. M., *Plasma Phys. Control. Fusion,* **1992**, *34,* 1433-1442.

102. “A fusion-fission hybrid reactor drove by high-density pinch plasmas”, Zoita V., Lungu S., *Nukleonika*, **2001**, *46(1)*, 81–84.

Chapter-2

Diagnostics Techniques

2.0 Introduction

The plasma focus device is abundant in physical processes as well as it has found many applications across multidisciplinary areas including pulse power technology, nuclear physics radiation material science, and radiation biology among others. It is essential to characterize them to understand various physical processes related to plasma focus dynamics and fusion grade plasma as well as to maximize the radiation output. The physical processes are of transient in nature which last only for a few hundred nanoseconds to a few microseconds. Moreover, radiations (optical and X-rays) and fusion products (protons, tritons, helions and neutrons when deuterium is used as filling gas) carry information pertaining to plasma focus dynamics. Various diagnostics techniques (active as well as passive) have been in use for characterization of plasma focus and the emitted radiations over the years since its inception. The diagnostic techniques such as magnetic probe, Faraday rotation, Faraday cup, Thomson scattering, interferometric system etc. are based on active probing method whereas Rogowski coil, voltage divider, image converter camera, X-ray pinhole imaging etc. are based on passive probing method.

Several indigenously designed and developed plasma focus devices have been characterized to understand plasma focus dynamics and mechanism of radiation emission as part of the thesis work. Various parameters such as current and voltage are recorded using Rogowski coil (by passively integrating current derivative signal recorded using Rogowski coil) and voltage divider. The neutron is measured using ^{3}He proportional counter, silver activation detector, plastic-scintillator detector. Ions are measured using Faraday cup and CR39 track detector.

Plasma focus devices have been used for many applications such as irradiation on fusion reactor relevant materials, deposition of thin films, non-destructive assay (NDA) of Uranium (^{235}U), and short-lived radioisotope production. Various material characterization techniques such as scanning electron microscope (SEM), surface profilometer, X-rays diffractometer (XRD), energy dispersive X-ray spectroscopy (EDX), and Raman spectroscopy have been used. Short descriptions of them have also been also included in the subsequent sections.

2.1 Electrical diagnostics

Two basic electrical diagnostics, for measurements of the discharge current and the voltage are used. Rogowski coil and voltage divider is used to record current-derivative and voltage respectively. The working principles of these two diagnostics are discussed in details below.

2.1.1 Rogowski coil

Rogowski coil is a multi-turn air core solenoid bend into a torus which encircles the current to be measured [Rogowski et al. 1912]. It works by sensing the magnetic field produced by current as per the Ampere's law. It has several advantages e.g. fast rise time, linear response, and simple geometry as well as electrically safe as it has no direct electrical connection with the main circuit. Numerous Rogowski coils have been designed in-house using RG174 and RG58 coaxial cables. Fig. 2.1(a) shows schematic of a Rogowski coil with n turns per unit length and cross-sectional area A which encircles a conductor carrying a current I. For an alternating current the voltage output from the coil is given by the rate of change of flux:

$$V_{out} = -\frac{d\emptyset}{dt} = -\mu_0 nA\frac{dI}{dt} = -\lambda\frac{dI}{dt} \quad \textbf{(2.1)}$$

here λ (= μ_0nA) is described as self-inductance of the coil. The eq. 2.1 shows that the voltage output from the coil is independent of the way the coil is placed round the conductor.

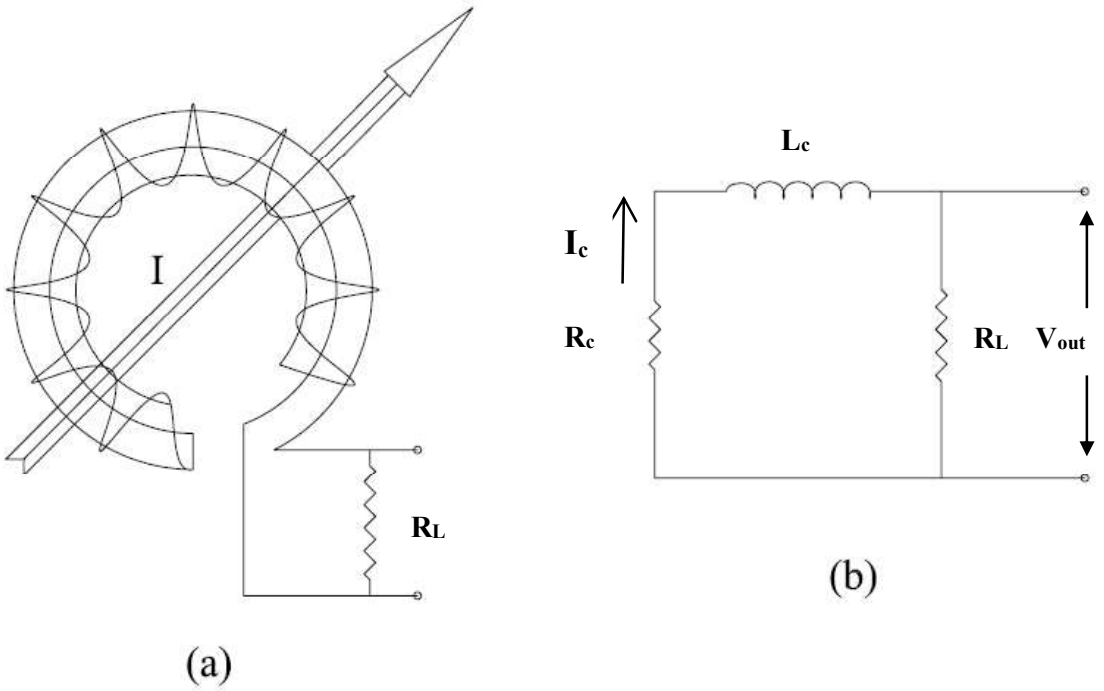

FIG. 2.1 Schematic of (a) Rogowski coil and (b) electrical equivalent circuit.

Considering the equivalent circuit shown in fig. 2.1(b)

$$\frac{d\emptyset}{dt} = L\,\frac{dI_c}{dt} + R\,I_c \qquad \textbf{(2.2)}$$

Here, L is the inductance of the coil and $R = R_c + R_L$, where R_c and R_L is the resistance of the coil and the output resistance across which the current is measured.

Combining eqs. (2.1) & (2.2), one may write

$$\lambda\,\frac{dI}{dt} = R\,(\frac{L}{R}\frac{dI_c}{dt} + I_c\,) \qquad \textbf{(2.3)}$$

For $\frac{L}{R}\frac{dI_c}{dt} < I_c$, $I_c = \frac{\lambda}{R}\frac{dI}{dt}$ and the coil is called a differentiating Rogowski coil.

And, for $\frac{L}{R}\frac{dI_c}{dt} > I_c$, $\lambda\,\frac{dI}{dt} = L\,\frac{dI_c}{dt}$ or $I_c \approx I$. The coil in this case is integrating Rogowski coil also called as "current transformer".

The current is obtained by externally integrating the Rogowski coil signal. In an LCR discharge, the maximum peak current I_0 can be expressed as:

$$I_0 = V_0\sqrt{\frac{kC_0}{L_0}} \tag{2.4}$$

The charging voltage V_0 and capacitance C_0 are known values whereas the information about inductance L_0 and voltage reversal k are obtained from experimentally observed current waveform. Thus, by obtaining values of k and L_0 from the experimentally observed signal, I_0 can be estimated and compared with the voltage V (maximum peak voltage) observed experimentally. The calibration factor *f* for the Rogowski coil can be computed from

$$f = \frac{I_0}{V_0}\frac{kA}{Volt} \tag{2.5}$$

2.1.2 Resistive Divider

Measurement of voltage is of two types: (i) measurement of high voltage (DC) on the capacitor bank and (ii) measurement of high transient (a few hundred ns) voltage across the plasma focus. For measurement of high DC voltage, resistive divider of conventional design is usually employed whereas for measurement of high transient voltage, special attention is required as frequency response of the conventional resistive dividers gets distorted due to stray capacitance of the resistive elements.

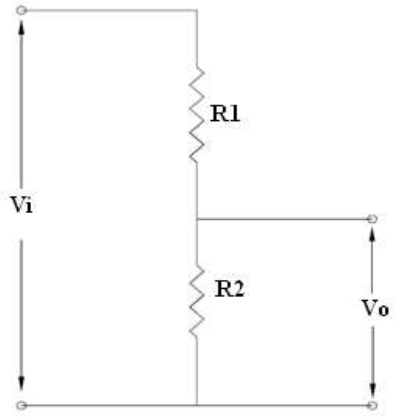

FIG. 2.2 Schematic of a resistive divider.

Here, a standard FLUKE make HV probe (Model no. 80K-40) is used to measure DC voltage and an aqueous copper-sulphate ($CuSO_4$) based resistor divider is used to record transient voltage. A schematic of resistive divider is shown in fig. 2.2. The resistances R1 and R2 are termed as the high voltage and low voltage arm respectively.

Simple aqueous resistor is proven to be a suitable alternative of the conventional resistors [Beverly 1995]. The aqueous $CuSO_4$ has low value of series inductance and this is used as high voltage arm. Low voltage arm consists of ten resisters (each 10 Ω) connected in parallel. The aqueous $CuSO_4$ resistor is chosen for its proven ability to withstand large electric fields. The solution has the advantage of being readily shaped by varying the container shapes, providing good contacts and being self- healing in the event of a voltage breakdown. The aqueous $CuSO_4$ divider has good high frequency and low frequency response. It is immune from the effects of stray inductance and capacitance due to large area and higher resistivity compared to other resistors such as carbon film resistors. The output voltage of this copper sulfate divider is terminated using 50 Ω. Thus, in a carefully designed column following features can be achieved: (i) constant divider ratio, (ii) wide bandwidth, (iii) linearity in ratio vs frequency, or amplitude, (iv) high voltage sustaining capacity, (v) better signal to noise ratio, and (vi) large energy dissipation.

2.2 Neutron detectors

2.2.1 Silver activation counter

The neutron yield is measured by the activation of metal foils. The activated nuclei decays by emitting beta and gamma rays which are then detected using the Geiger-Muller (GM) counter. Silver [White 1948] and Indium [Pedretti et al. 1985] are commonly used metal foils. In our experiments, the silver foil activation is used [Gentilini et al. 1980]. Natural silver has two stable isotopes ^{107}Ag and ^{109}Ag which occur in almost equal percentage of 51.35% and 48.65% respectively. The decay process along with the half-life ($T_{1/2}$) and reaction cross section (σ_a) for thermalized neutrons are:

$^{107}Ag\ (n, \gamma)\ ^{108}Ag \longrightarrow {}^{108}Cd + \beta\ (1.77\ MeV) + \gamma(0.63\ MeV)$

$(T_{1/2} = 162\ s,\ \sigma_a = 44\ b)$

$^{109}Ag\ (n, \gamma)\ ^{110}Ag \longrightarrow {}^{110}Cd + \beta\ (2.87\ MeV) + \gamma(0.07\ MeV)$

$(T_{1/2} = 24.5\ s,\ \sigma_a = 110\ b)$

The detector used here for measurement of neutron flux consists of eleven GM tubes of 2 cm outer diameter and 17 cm length. The outer surface of each tube is covered with 250 μm thick silver foil. The GM tubes are arranged in two rows (six in front and five in second row) inside a rectangular box ($10 \times 30 \times 30\ cm^3$) of paraffin to increase the detection efficiency. The detector box is covered with 0.2 mm thick aluminum sheet which is grounded to avoid any electromagnetic noise pickup by the detector. The GM tubes are connected in parallel to common input and output points. The output is connected to a radiation counting unit through a RG58 coaxial cable which is also used for high voltage supply to the GM tubes.

The silver activation detector is in-situ calibrated using the calibrated radio-isotopic neutron source (Pu - Be) having source strength of N_n neutrons/s. The number of activated silver atoms (A) produced per second is given by

$$A = K\ \sigma_a\ n_0\ N_n\ (1 - e^{-\lambda t}) \qquad \textbf{(2.6)}$$

Here K is a constant (for all geometrical factors), σ_a is the activation cross section, n_0 is number density of silver foil and λ is the decay constant ($= \ln 2/T_{1/2}$) and t is the duration of incident neutron flux.

For a pulsed neutron source such as plasma focus device, t can be much less than $T_{1/2}$ (i.e. $\lambda t << 1$) for the constant source such as Pu - Be, t can be more than $T_{1/2}$ (i.e. $\lambda t >> 1$). In both cases, A can be written as

$$A = K\,\sigma_a\,n_0\,N_n\,\lambda\,t \qquad \text{(for a pulsed source)} \tag{2.7}$$

$$= K\,\sigma_a\,n_0\,N\,\lambda \tag{2.8}$$

and $$A = K\,\sigma_a\,n_0\,N_n \qquad \text{(for a constant source)} \tag{2.9}$$

The number of activated atoms decline exponentially after activation ceases. If, after activation in both the cases, the decay is counted for a fixed period of time, then the ratio of count rates can be expressed as:

$$\frac{Q_p}{Q_f} = \frac{K\,\sigma_a\,n_0\,N\,\lambda}{K\,\sigma_a\,n_0\,N_n} \tag{2.10}$$

Or $$N = Q_p\left(\frac{1}{Q_f}\,\frac{N_n}{\lambda}\right) \tag{2.11}$$

Where Q_p and Q_f are the count rates (proportional to A) for a pulsed and a constant source respectively.

In silver activation counter, the value of Q_f is mainly due to the ^{110}Ag decay. For time T=10 s, the number of counts corresponding to the number of decayed ^{110}Ag and ^{108}Ag nuclei will be:

$$Q_f^{110} = A_0^{110}\left(1 - e^{-\frac{0.693}{245}\times 10}\right) = 0.25\,A_0^{110} \tag{2.12}$$

$$Q_f^{108} = A_0^{108}\left(1 - e^{-\frac{0.693}{162}\times 10}\right) = 0.042\,A_0^{108} \tag{2.13}$$

The ratio of two activities is:

$$\frac{A_0^{110}}{A_0^{108}} = \frac{0.49n_0 \times 110}{0.51n_0 \times 44} = 2.4 \quad \textbf{(2.14)}$$

Therefore, only small fractions (~7%) of decay counts are due to decay of ^{108}Ag. So the contribution of the ^{108}Ag in measurement of counts is negligible and it can be excluded during calibration with the constant source. For calibration of activation detector, a Pu-Be source of source strength 5×10^4 neutrons/s is used. Within the limit of unavoidable errors, the lower limit of neutron detection is $\approx 3 \times 10^5$ neutrons per discharge, decided by the proximity of the set up.

2.2.2 ^{3}He proportional counter

The plasma focus devices operating at energies in sub-kilojoule range are of low neutron yield (typically 10^3-10^6 neutrons/pulse). High detection threshold ($\geq 3 \times 10^5$ neutrons per discharge) of silver activation detector limits its use for measurement of low neutron yield. Helium (^{3}He) detector [Moreno et al. 2008] is the most suitable detector for low neutron yield detection because of their high neutron detection efficiency and high sensitivity (~ 5330 b) for thermal neutrons (< 0.5 eV). It has extremely low gamma sensitivity and hence it has high neutron to gamma discrimination. The neutron detection principle is based on the nuclear reaction:

$$^3\text{He} + \text{n} \rightarrow {}^3\text{H} + {}^1\text{H} + 764\ \text{keV}$$

The energy produced in the ^{3}He (n, p) ^{3}H nuclear reactions is deposited in the proportional counter which leads to ionization of the ^{3}He gas. The ionization potential of ^{3}He gas is about 25 eV.

The cross-section for neutron capture reaction ^{3}He (n, p) ^{3}H strongly depends on the incident neutron energy, having roughly $1/\sqrt{E}$ dependence [Crane et al. 1991]. Because of the strong energy dependence, to increase the detection efficiency front (plasma focus facing) and rear of ^{3}He detector

assembly is covered using 40 mm thick Perspex (two sheets, each of 20 mm thick) and a single Perspex sheet of 20 mm thickness respectively. The front and rear Perspex sheets serve as moderator and reflector respectively. Further, short pulse of neutrons (10-100 ns) is dispersed in time (a few 100s of μs) in moderator which in turn reduces any saturation effect in the detector and also facilitates the detection of pulse neutrons with the available electronics. Moreover, the moderator also ensures that neutron pulses are separated from the electromagnetic radiations produced in plasma focus devices.

It is cross calibrated using a calibrated silver activation detector for recording of pulse neutrons. Both detectors are used simultaneously to measure neutron yield of 10^6 to 10^7 neutrons per pulse from a plasma focus device. The distance of ^{3}He detector is varied and at each distance the calibration factor (ratio of number of neutron pulses in ^{3}He detector to the neutron yield measured using silver activation detector) is estimated. At 0.5 m distance, each pulse in ^{3}He detector corresponds to (1080 ± 30) neutrons which is the lower limit of neutron detection for the ^{3}He detector.

2.2.3 Plastic scintillator Detector

The measurement of time resolved emission of neutrons is performed using a plastic scintillator in combination of a photomultiplier tube. Fast neutrons (>1 MeV) create recoil protons by elastic collision in scintillator material which then produce scintillation through excitation and de-excitation of scintillator atom. The scintillation photons are then detected by the photomultiplier tube. The scintillator used here is NE102A (Polyvinyl Toluene material, maximum emission at 425 nm) of size: 2-inch diameter and 2-inch length and the photomultiplier tube is XP2012. To reduce the noise pickup, scintillator along with the photomultiplier is encased in matching brass housing. NE102A has a decay constant of ~2.4 ns **(**G. F. Knoll, 3rd Ed.**)**, but the response time of the system used is limited to 4 - 6 ns rise time due to the response of the photomultiplier.

For time resolved study, the PSD is placed radially w. r. t. electrode axis. PSD is sensitive to both the neutrons and hard X-rays. To discriminate neutron and hard X-ray pulses, a lead sheet of appropriate thickness is placed in front of the PSD. The lead sheet cuts off most of the hard X-rays. The energy of neutrons is estimated using time of flight (TOF) method. Two identical PSDs are used to record neutron signal. The neutron energy using TOF method can be estimated using the formula given as

$$E_n = \frac{1}{2}mv^2 = \frac{1}{2}m\left[\frac{c(d2 - d1)}{c(t2 - t1) + (d2 - d1)}\right]^2 \quad \textbf{(2.15)}$$

Here, d1 and d2 are the distances of PSD from the plasma focus, t1 and t2 are the neutron flight time, c is speed of light, v is speed and m (= 1.67×10^{-27} kg) is mass of neutrons.

The energy of neutrons produced in plasma focus device can also be estimated using single PSD. The hard X-rays and neutrons are produced almost at same time [Mather 1965]. The hard X-ray pulse travels with speed of light (c) and neutron pulse travels with velocity decided by its energy (E_n). The difference in travel time of hard X-rays (t_x) and neutron pulses (t_n) is used to estimate neutron energy. The detector distance is varied to see the difference in travel time of neutron pulse with respect to hard X-ray pulse. The time difference (t) can be calculated as:

$$t = (t_n - t_x) \quad \textbf{(2.16)}$$

$$t = d/(2\,E_n/m_n)^{1/2} - d/c \quad \textbf{(2.17)}$$

$$E_n = \frac{1}{2}M_n\left(\frac{d}{t + d/c}\right)^2 \quad \textbf{(2.18)}$$

Here d is detector to plasma focus distance and M_n is the mass of neutron.

2.3 Ion diagnostics

2.3.1 Faraday cup

Faraday cup is one of the simplest and inexpensive diagnostics to record time-resolved emission of ions. It can respond to a broad energy range of ions with high temporal resolution. It consists of a collector made of conducting material and an outer shield, also working as ground electrode. The collector and the ground is separated by an insulator material. A schematic of Faraday cup is depicted in fig. 2.3. Their dimensions are chosen to match with impedance of coaxial cable used for signal transmission (i.e. 50 Ω). The characteristics impedance of the Faraday cup is estimated using a simple formula given as [Mohanty et al. 2005]

$$Z = \frac{138.2}{\sqrt{\epsilon_r}} \log_{10} \frac{D}{d} \text{ ohms} \qquad \textbf{(2.19)}$$

Here D and d is the inside diameter of outer electrode and outside diameter of collector, ε_r is dielectric constant of the insulator material. Faraday cup is used both biased and unbiased. For recording of ion pulses, Faraday cup is negatively biased. The negative bias prevents the electrons accompanying the ion beam from entering the Faraday cup. The negative biasing also prohibits the secondary electrons (produced from the collector surface on bombardment of the energetic ions) from escaping the surface of the collector. The loss of secondary electrons result in current overestimation for the ion beam as it gives impression that one more ion has fallen onto the collector surface.

Faraday cup is designed and developed using indigenous components. Graphite and Brass are chosen for collector and outer shield material. The insulator material used here is of Teflon ($\varepsilon_r = 2.15$). Graphite is chosen as the collector material as it has low secondary electron emission coefficient. Further, the deep cone shape of the collector surface reduces the escaping of the secondary electrons and therefore reduced error in the measurements of ion fluence.

The values of D and d are chosen to be 17 mm and 5 mm respectively to adjust the impedance value as 50 Ω. The photographs of different components of Faraday cup and its assembly are shown in fig. 2.4(a) and (b) respectively. An aperture of 1 mm diameter is placed at the entrance of the Faraday cup to control the ion fluence falling on it. It was negatively biased at 100 V for all experiments.

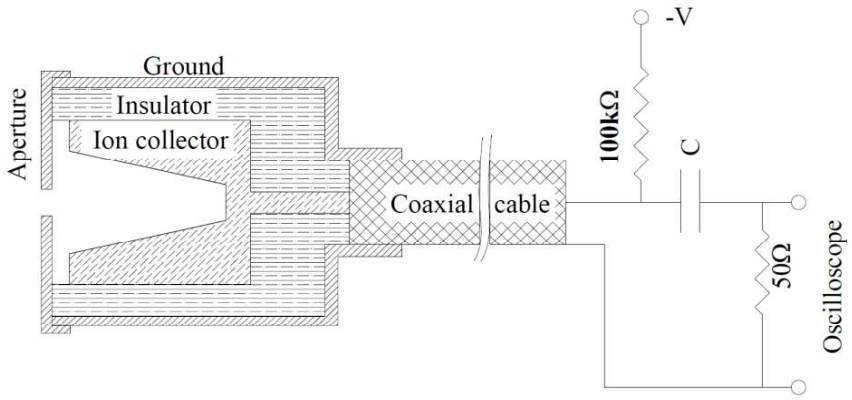

FIG. 2.3 Schematic of negative biased Faraday cup for ion measurements.

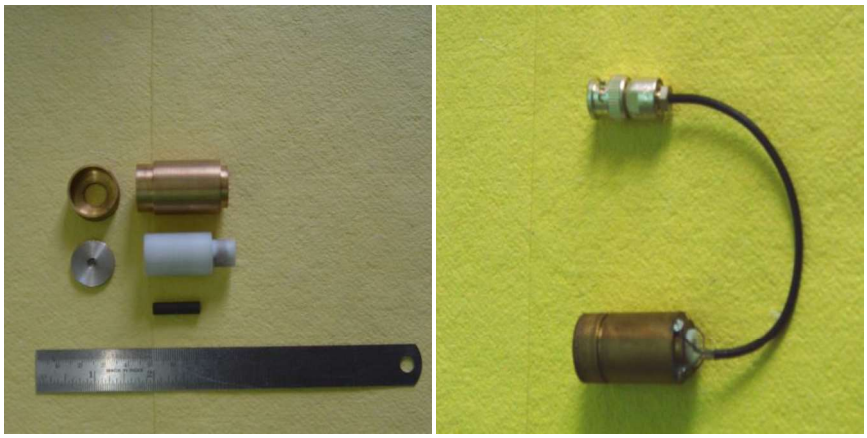

FIG.2.4 Photographs of (a) parts of faraday cup and (b) Faraday cup.

The ion energy spectrum can be determined from the time of flight of ions using Faraday cup signals. If the ions are created and accelerated in a short time interval compared to the flight time, the speed of the ions v_i can be estimated at a distance d from the source point using the relation:

$$v_i = \frac{d}{t_i} \tag{2.20}$$

here t_i is the flight time of ion. The distance d should be very large compared to the ion source size.

The energy of ion having speed v_i is estimated using time of flight

$$\text{Ion energy} = \frac{m_i v_i^2}{2} \tag{2.21}$$

Where m_i ($= 3.34 \times 10^{-27}$ kg) is mass of deuterium ion.

The number density of deuterium ions having velocity v_i can be estimated using the formula

$$n = \frac{V_i}{R\, e\, A\, v_i} \tag{2.22}$$

Here V_i is the voltage corresponding to ion time of flight t_i, R (= 50 Ω) is resistance across which ion current is measured, e ($= 1.6 \times 10^{-19}$ coulomb) is the electronic charge and A is the area of the Faraday cup aperture. The amplitude of ion pulse and its corresponding time of flight are used for evaluation of peak ion number density and most probable energy of ions.

The fluence of ions is estimated from the Faraday cup signal using the formula

$$\text{Total ions} = \frac{\int V dt}{R\, e\, A} \tag{2.23}$$

Faraday cup has certain limitations including low signal to noise ratio, the emission of secondary electrons by the energetic ions and electromagnetic radiation. Above problems are overcome by taking various measures viz. (i) the signal to noise ratio is improved by appropriately shielding the Faraday cup and (ii) the secondary electrons emissions are reduced through use of passive methods such as proper selection of ion collector material and its shape and/or using active methods such as by applying a strong transverse static magnetic field in the vicinities of the collector [Gerdin et al. 1981].

2.3.2 Solid State nuclear track detector

Solid state nuclear track detector (SSNTD) is used for measurement of spatial emission profile of ions emitted in plasma focus device. This is a passive detection technique where ionizing particles pass through a dielectric material (normally plastic) and leaves a track in the form of damages such as ionization, broken molecular bonds etc. along the trajectory of the particles. These tracks are typically of a few nm in radius which is not visible to naked eye. The tracks can be made visible upon etching in a strong acid or base solution. Generally, aqueous solution of sodium-hydroxide (NaOH) or potassium-hydroxide (KOH) is used at 70^{O} C temperature for etching of the exposed detector material. The etchant removes the material faster near the tracks and then these tracks are transformed into pits on the surface which can then be easily visible and counted using a conventional microscope.

The plastic under conventional names CR-39/PM355 are most widely used SSNTDs for the detection of charged particles. Basically, this plastic material is transparent thermo-set polymer of "Allyl Diglycol Carbonate" with the chemical formula $C_{12}H_{18}O_7$. They have threshold of specific energy loss (-dE/dx) for an ionizing particle [Ziegler et al. 2010]. The particle having –dE/dx value above this threshold can only create damages severe enough to lead to an etchable track. The threshold is well above the specific energy loss of an electron track, so SSNTDs are inherently insensitive to fast electron or photons. For filtering out the charged particles with energies below a certain threshold, filters of appropriate material and thickness can be used in front of SSNTDs.

Ionizing particles of different masses, charge states and energies can be differentiated based on appearance of the etched track. However, the quantitative measurements such as fluence and energy from the etched tracks need to be deduced carefully since the normality of the etching solution, temperature of etching solution, and duration of etching greatly influence the charge particle track diameter and depths [Gaillard et al. 2007].

2.4 Surface damage characterization techniques

The energetic ions and plasma streams emitted in plasma focus device have been used to irradiate samples of different materials. They produce damage on the surface of mirror polished samples in the forms of erosion and various other surface defects such as blisters, micro-cracks, voids and so on. The surface damage is characterized using different techniques. A brief description of these techniques has been mentioned in the following section.

2.4.1 Scanning Electron Microscope (SEM)

Scanning Electron Microscope **(**SEM) is a non-destructive technique which is used to study surface morphology of the samples. It uses a focused, high energy electron beam that interacts with the specimen to generate a variety of signal from its surface. Energetic electrons in a SEM interact with a solid sample and produce secondary electrons (SE) used to produce SEM images, backscattered electrons (BSE) gives phase contrast, characteristic X-rays are used for elemental analysis), visible light (cathodo-luminescence) for studying luminescence under an electron beam and heat. Secondary electrons and backscattered electrons are commonly used for imaging samples. A drawing in fig. 2.5 shows interaction of focused electron beam with specimen.

SEM analysis requires use of a vacuum chamber, an accelerated electron beam, multi-sample loadable stage and various detectors. In the electron gun, electrons are produced by a field emission (FESEM) or thermionic technique and an accelerated to a high voltage up to 30 kV. These electrons are focused to a narrow beam and directed on to the sample. The various signals emitted from the

sample are detected by appropriate detectors. A Carl Zeiss make Supra 55 FESEM used for the present study. The system is equipped with energy-dispersive X-ray analysis (EDX) and it is capable of qualitative as well as quantitative analysis of relative concentrations of elements present.

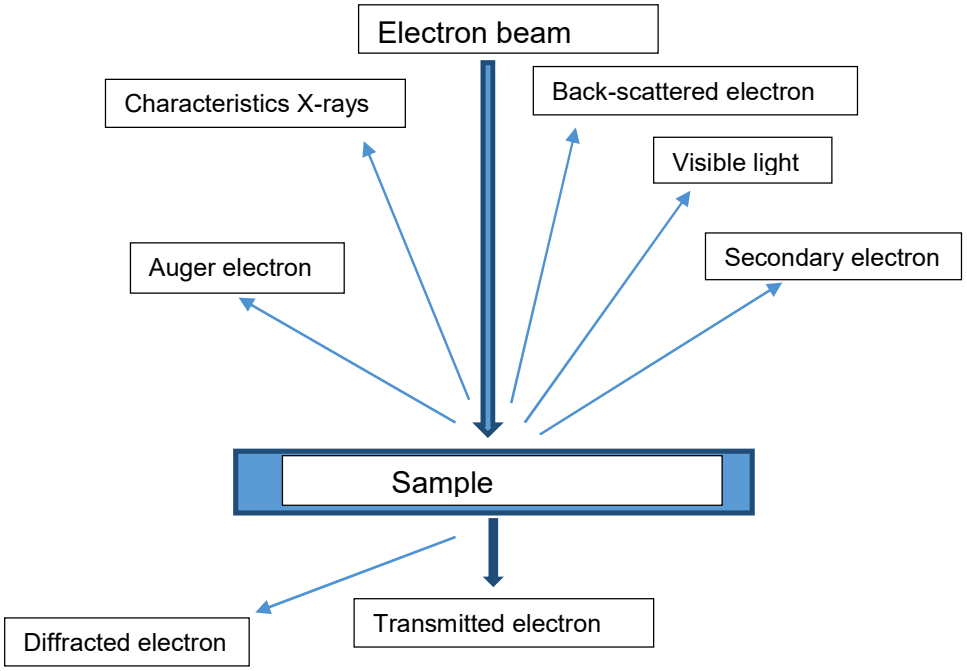

FIG. 2.5 Diagram of electron- material interaction phenomenon used in SEM & EDX.

2.4.2 Energy dispersive X-ray Spectroscopy (EDX)

The qualitative / quantitative measurement of elemental composition present in the sample is obtained by EDX. This technique operates on principle of detection of characteristic X-rays emitted by atoms of elements when electron beam interacts with the sample. The basic components of EDX are X-ray detector, pulse processor (to measure voltage corresponding to X-ray energies) and a computer. The size of voltage pulse is proportional to energy of X-rays. Elemental distribution maps or elemental line profiles can be obtained by EDX.

2.4.3 X-ray diffraction (XRD)

X-ray diffraction is a powerful tool to examine the crystal structure of the materials. The X-ray diffractometer (RIGAKU, ULTIMA-IV operated at 1.6 kW power) in the Bragg-Brentano geometry (fig. 2.6) is used to record diffraction pattern. The X-ray wavelength used is 1.54056 Å (Cu-K_α line). The principle behind X-ray diffraction is that the X-rays fall on the sample and interacts with the atoms in the lattice, causing scattering in all directions. When the sample is crystalline having a periodic arrangement of atomic planes, the X-rays scattered by each plane constructively interfere and result in interference maxima at particular angles.

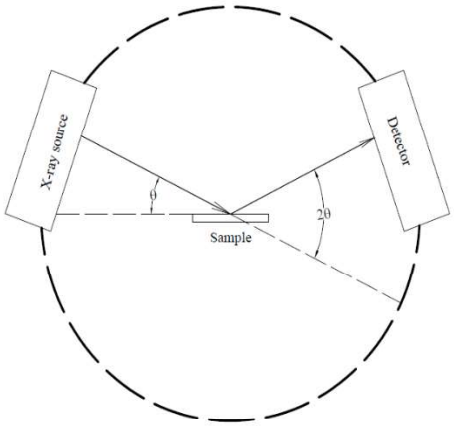

FIG. 2.6 Diagram of X-ray diffraction principle in Bragg-Brentano geometry.

This happens when the path difference of the scattered X- rays from successive atomic planes forms an integral multiple of the wave length (λ) of the X-ray. The condition for the formation of diffracted radiation is known as Bragg's law of diffraction and is expressed as $2d \sin\theta = n\lambda$, where, λ is the wavelength of the X-ray used, θ is the diffraction angle and d is the lattice pacing. Diffraction peaks observed in the X-ray diffraction profiles contain information about the lattice parameters, strain, texture etc. of the samples under probe.

2.4.4 Raman Spectroscopy

Raman spectroscopy is a class of vibrational spectroscopy primarily concerned with the qualitative and quantitative evaluation of the structural property and transformation of materials at the molecular level. The transformations may be in the form of energy of vibrational excitations, phase transformations, chemical reactivity and magnetic and electronic transitions. It probes the sample by utilizing inelastic scattering processes using an intense beam of monochromatic radiation of wave number (υ_0) in the near ultra violet, visible or infra-red region of the electromagnetic spectrum. A diagram depicting the working of Raman spectroscopy has been shown in fig. 2.7.

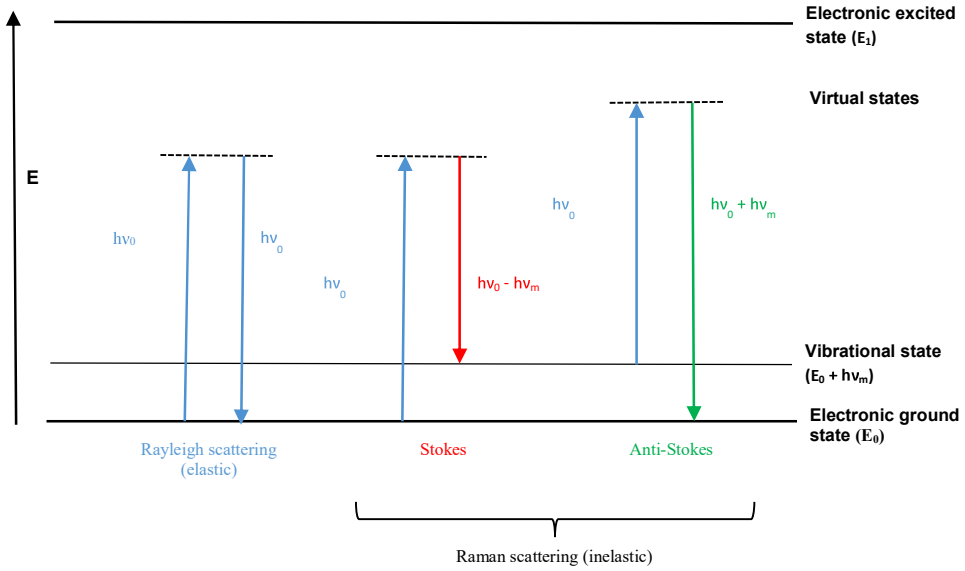

FIG. 2.7 Diagram of Raman spectroscopy principle.

Most of the radiation is scattered without a change in wave number (Rayleigh scattering). However, a small part of the scattered radiation (typically 1 out of 10^6 photons) is scattered with the wave number $\upsilon_0 \pm \upsilon_m$ where, υ_m is characteristic wave number of molecular vibration that undergo excitation. The $\upsilon_0 - \upsilon_m$ and $\upsilon_0 + \upsilon_m$ scattered radiation components are known as Stokes and anti-Stokes lines, respectively. The Raman Effect is often thought of as a vibrational or rotational frequency modulation of the electric field of the incident radiation. In the present work, a Raman

spectrograph (Jovin –Yvon HR 460 single stage) is used with liquid nitrogen cooled charge coupled device (CCD). For excitation, diode pulped solid state laser (Nd-YAG) with wavelength 532 nm is used. Usually only the stokes lines are measured, since the intensity of anti-stokes lines are much weaker than that of stokes line at ambient temperature.

2.4.5 Surface Profilometer

Surface profilometer is used to measure the surface roughness profile of materials before and after irradiation. In this technique, a diamond stylus scans along the surface of the material at a constant speed for a specified distance and under a specified force. The profilometer can measure small vertical features ranging in height from 10 nm to 1mm. The height position of the diamond stylus generates an analog signal which is converted into a digital signal stored, analyzed and displayed, and the horizontal resolution is controlled by the scan speed and data signal sampling rate. The radius of diamond stylus ranges from 20 nm to 50 μm. Smaller the tip radius of the stylus greater is the accuracy in the measurement.

References:

1. "Aqueous-electrolyte resistors for pulsed power applications", Beverly R. E. and Campbell R. N., *Rev. Sci. Instrum.,* **1995**, *66*, 5625-5629.
2. "Passive Nondestructive Assay of Nuclear Materials", Crane T. W. and Baker M. P., Chap. 13, Technical Report No. NUREG/CR-5550, LA-UR-90-732 (edited by D. Reilly et al.), Los Alamos National Laboratory, Los Alamos, NM, USA, **1991**.
3. "Study of saturation of CR39 nuclear track detectors at high ion fluence and of associated artifact patterns", Gaillard S., Fuchs J., Galloudec N. R.-L., and Cowan T. E., *Rev. Sci. Instrum.,* **2007**, *78*, 013304 (1-13).

4. “Comparison of four calibration techniques of a silver activated Geiger counter for the determination of the neutron yield on the frascati plasma focus experiment”, Gentilini A., Rager J. P., Steinmetz K. et al., *Nucl. Instrum. Methods Phys. Res. A,* **1980**, *172*, 541-552.
5. “Faraday cup analysis of ion beams produced by dense plasma focus”, Gerdin G., Stygar W., and Venneri F., *J. Appl. Phys.,* **1981**, *52*, 3269–3275.
6. “Radiation detection and measurement”, Knoll G. F., 3rd Ed., John Wiley & Sons, Inc., New York.
7. “Formation of a high-density deuterium plasma focus”, Mather J. W., *Phys. Fluids,* **1965**, *8(2)*, 366-377.
8. “Development of Multi Faraday Cup Assembly for Ion Beam Measurements from a Low Energy Plasma Focus Device”, Mohanty S. R., Bhuyan H., Neog N. K. et al., *Jap. J. Appl. Phys.,.***2005**, *44(7A)*, 5199-5205.
9. “System for measurement of low yield neutron pulses from D–D fusion reactions based upon a 3He proportional counter”, Moreno J., Birnstein L., Mayer R. E. et al., *Meas. Sci. Technol.,* **2008**, *19*, 0870021-5.
10. “Improved calibration of DD neutron counters by activation of two indium disks in the Frascati 1-MJ plasma focus”, Pedretti E., Rager J. P. and Merlo V., *Rev. Sci. Instrum.,* **1985**, *56*, 1087-1089.
11. “Die Messung der magnetische Spannung,” Rogowski W. and Steinhaus W., *Arch Electrotech,* **1912**, *1*, 141–150.
12. “The Natural Abundance of Isotopes of Stable Elements”, White J. R. and Cameron A. E., *Phys. Rev.,* **1948**, *74(9)*, 991-1000.
13. “SRIM – The stopping and range of ions in matter (2010)”, Ziegler J. F., Ziegler M.D., Biersack J. P., *Nucl. Instrum. Methods Phys Res. B,* **2010**, *268*, 1818–1823

Chapter-3

Design and Development of Plasma Focus Devices

3.0 Introduction

In view of relevance in fusion research and for applications, several plasma focus devices operating at energies in sub-kilojoule to kilojoule range are designed and developed. Sealed plasma focus tube based, "SPF-P1" and "SPF1-P2" devices operating at 200 J are developed. In SPF-P1 device, a cylindrical tube (SS) of inner diameter: 34 mm and inner length: 80 mm is used as the cathode as well as plasma chamber. The effective volume including anode (SS) and insulator (alumina) is around 73 cm^3. The plasma focus tube is assembled with single capacitor of 4 μF. Neutrons are seen to be produced in around 150 shots over a time spanning up to 120 days without purging deuterium gas [Rout et al. 2008]. In SPF1-P2, plasma chamber of the volume of 33 cm^3 (including anode and insulator) is used which makes this one of the smallest device amongst its class of miniature devices developed by various research groups [Soto et al. 2009, Soto et al. 2008, Silva et al. 2003, Verma et al. 2008, Milanese et al. 2003, Gribkov et al. 2006]. The SPF1-P2 device is operated for 200 shots over 200 days without purging deuterium gas. The details of construction of SPF1-P2 device and its optimization study are included in present work [Niranjan et al. 2011].

Repetitive operating plasma focus, "PF-P5" operating at 500 J is designed and developed. The PF-P5 device is a miniature table top neutron source having plasma chamber volume of 150 cm^3. It is operated repetitively at a repetition frequency of 10 Hz. The construction, optimization and time resolved neutron emission are studied in detail and reported [Niranjan et al. 2012].

Three different plasma focus devices, "PF-2", "MEPF-12" and "MEPF-17" operating at kilojoule range i.e. at 2 kJ, 11.5 kJ and 17 kJ respectively are developed. They have relatively large electrodes dimensions as per scalability laws for plasma focus [Soto et al. 2010, Lee et al. 1996] This allows to conveniently place different diagnostics without perturbing plasma focus processes and also

convenient for applications. Constructions and optimization studies on all three plasma focus devices have been discussed in details in this chapter.

3. 1 Design of plasma focus and associated components

Design of plasma focus device is primarily based on the scaling laws for the radiation yield. [Decker et al. 1980, Krompholz et al. 1981, Lee 2008] The parameters such as capacitor bank energy and peak discharge current are primarily decided for the required radiation yield and then matching plasma focus and associated pulse power systems are designed. In the following sections, details of design of capacitor bank, associated pulse power systems and matching plasma focus have been discussed.

3.1.1 Capacitor bank

The capacitor bank is used as an energy driver for plasma focus device. The energy E_0 ($= {}^{1}/_{2}\, C_0 {V_0}^2$) required for achieving the desired radiation yield can either be obtained by proper selection of capacitance (C_0) or operation voltage (V_0). Primarily, the operation voltage is chosen, and then accordingly, all the electrical parameters are determined. The peak discharge current ($I_0 = V_0\sqrt{kC_0/L_0}$) depends on the parameters such as capacitance, C_0, voltage V_0, equivalent series resistance (ESR), and equivalent series inductance (ESL) of the capacitor. Therefore, for a particular operation voltage, a single or an appropriate number of capacitors are connected in parallel to meet the total peak discharge current requirement. The parallel configuration of capacitors is termed as the "capacitor bank" and this effectively has reduced inductances and resistances. The capacitor bank is connected to a switch (triggered spark gap) using transmission lines for fast energy transfer to the plasma focus load in a minimum possible inductance configuration.

The connection from switch to plasma focus load is also made using transmission lines. The transmission lines are either made of parallel plates or a number of coaxial cables connected in

parallel. Each of them has associated advantages and disadvantages. The parallel plate transmission lines make the overall system compact, transportable and easy in dismantling and also have lowest possible inductance. The coaxial cable offers the flexibility but it also has disadvantage of making the system bulky and immovable. For large energy capacitor bank with multiple discharge modules operating in parallel, use of coaxial cables are beneficial, since it is easy to lower the inductance by parallelization. For small and medium energy capacitor bank, use of parallel plate transmission lines is beneficial as it reduces the overall size of the system and it is more reliable and economical.

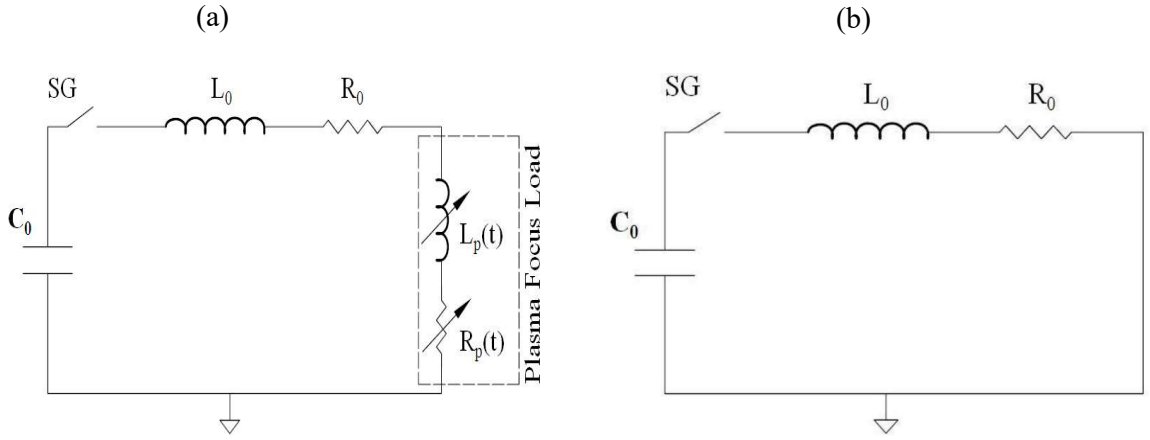

FIG. 3.1 Electrical equivalent circuit for (a) plasma focus device set up and (b) short circuit set up.

The peak discharge current is estimated using short circuit. Figs. 3.1(a) and (b) depict the electrical equivalent circuits for plasma focus device and short circuit. It consists of a capacitor bank of capacity C_0, an equivalent series inductance L_0 (including the inductances of the capacitor bank, connections and switches) and an equivalent series resistance, R_0, of the circuit. The moving plasma sheath is considered as an inductance and resistance with temporal dependence $L_p(t)$ and $R_p(t)$ respectively. The stored energy in the capacitor bank is discharged into the plasma focus load through the triggerable spark gap (SG) switch.

According to Kirchhoff's voltage law, the equations for the voltage in the plasma focus equivalent circuit [fig. 3.1(a)] can be expressed as:

$$\left(V_0 - \frac{1}{C_0}\int Idt\right) - \frac{d}{dt}(L_0 I) - R_0 I = R_p(t)I + \frac{d}{dt}(L_p I) \quad \textbf{(3.1)}$$

The plasma inductance in the axial and the radial phases can be written as

Axial Phase: $$L_p(t) = \frac{\mu_0}{2\pi}\ln\frac{b}{a}z_0 \quad \textbf{(3.2)}$$

Radial phase: $$L_p(t) = \frac{\mu_0}{2\pi}\ln\frac{b}{r_p}z_p \quad \textbf{(3.3)}$$

Here, a and b are the anode and the cathode radius respectively, z_0 is the effective anode length (exposed to plasma in run down phase), $z_p(t)$ and $r_p(t)$ are length and radius of the plasma column in the radial compression phase.

The resistance associated with the plasma column in the radial phase can be expressed as:

$$R_p(t) = \frac{z_p}{\sigma\pi r_p^2} \quad \textbf{(3.4)}$$

Here, σ is the electrical conductivity.

For short circuit [fig. 3.1(b)], the eq. (3.1) can be rewritten as:

$$\left(V_0 - \frac{1}{C_0}\int Idt\right) - \frac{d}{dt}(L_0 I) - R_0 I = 0 \quad \textbf{(3.5)}$$

The current, I (t) flowing in the short circuit is described by the following equations:

$$I(t) = \frac{V_0}{\omega L_0} e^{-\alpha t} \sin \omega t \qquad \textbf{(3.6)}$$

Here, $\alpha = \frac{R_0}{2L_0}$; $\omega = \sqrt{\frac{1-r^2}{L_0 C_0}}$ with $r = \sqrt{\frac{R_0 C_0}{4L_0}}$

For plasma focus, value of R_0 is low (typically in mΩ), therefore the peak discharge current (I_0) and discharge time-period (T) can be expressed as:

$$I_0 = V_0 \sqrt{\frac{kC_0}{L_0}} \quad ; \qquad k = e^{\frac{-\pi r}{\sqrt{(1-r^2)}}} \qquad \textbf{(3.7)}$$

$$T = \frac{2\pi}{\omega} = 2\pi\sqrt{L_0 C_0} \qquad \textbf{(3.8)}$$

Here, k is a constant, defined as voltage reversal (i.e. ratio of two consecutive current/voltage amplitudes). The peak discharge current I_0 and rise time (T/4) are used for determination of plasma focus dimensions.

3.1.2 Triggered spark gap

The triggered spark gap switch is used to transfer capacitor bank energy to the plasma focus load. It consists of two electrodes, termed as "spark electrodes" separated by a dielectric medium (gas, liquid or solid). It is preferred over other available pulse power switches like Rail-gaps, Thyratron, Ignitron, Pseudo spark etc [Burkes et al.1978], because of its simple design, reliable operation low cost as well as lesser maintenance. This operates by inducing a dielectric breakdown through high

amplitude (25 - 30) kV, fast rise (<1 μs) trigger pulse in the dielectric medium between the two electrodes. The electrode materials are chosen based on the peak current transfer from the capacitor bank to the load. The commonly used electrode materials are SS304, brass or an alloy of tungsten. The SS304 is usually preferred over other materials because of low erosion rate, easy machinability and availability at cheaper rate.

All spark gap switches used here are using open air as the dielectric medium. The spark electrodes are of hemispherical shape and they are made of SS304 material. The center pin triggered and edge triggered spark gap geometry are used here. In the center pin triggered, the trigger electrode is inserted in the middle of the discharge end of the spark electrode whereas in the edge-triggered, a trigger electrode is fixed over the discharge end of spark electrode. In center pin triggered switch, trigger pin is insulated from spark electrode using tube made of Ultra High Molecular Weight (UHMW).

3.1.3. High Voltage Charging Supply

The constant current charging is used to charge the capacitor bank. A schematic of constant current supply is shown in fig. 3.2. The input of the main supply (0 - 230 V AC) through an isolation transformer and a motorized variac is fed to a high voltage step up transformer. The output of high voltage step up transformer is converted to DC voltage using a half-wave rectifier circuit. A shorting device based on electrically activated solenoid valves (230 V AC normally closed type) with ceramic resistors is placed in power supply to enable charging of the capacitor bank. The constant charging rate of 1 kV/s is kept for all the capacitor banks. The ratings of the components of the power supply are chosen to achieve the desired charging rate. The diodes of correct PIV (peak inverse voltage) are important to place in order to avoid the damage to the power supply due to voltage reversal. The voltage reversal can damage the diodes, if the magnitude of the reversal is high enough to cause

excessive current flow in the diodes. To avoid this, a chain of diode of PIV $\geq 2V_{max,}$ must be placed. Here, V_{max} is the maximum output voltage of the power supply.

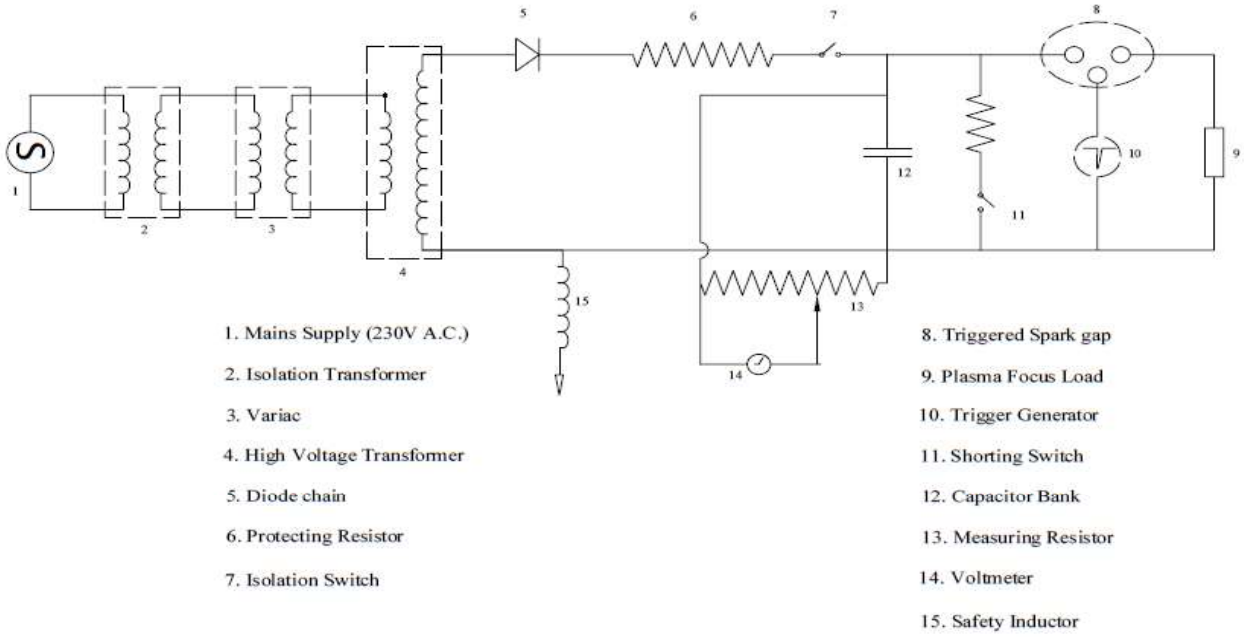

FIG. 3.2 Schematic of high voltage power supply.

3.1.4 Plasma focus

Design of plasma focus load is based on the short circuit time-period and the peak current. The electrode dimensions are chosen such that the axial run-down time of the current sheath coincides with the current rise time. The axial run down time of the plasma sheath is calculated using formula given below [Lee et al. 1996]

$$t_a = \left(\frac{4\pi^2(b^2-a^2)z_0^2\rho}{\mu \ln\left(b/a\right)I_0^2}\right)^{1/2} \quad \textbf{(3.9)}$$

Where I_0 is peak current, ρ is mass density of the gas, μ is permeability of the free space.

A comparison of plasma focus devices operating at different energies reveals an interesting facts i.e. constancy of energy density (E/V_p) and drive parameter $I_0/a.p^{1/2}$ (where V_p is the pinch plasma volume, I_0 is maximum peak discharge current, a is anode radius and p is the filling gas pressure) at the optimal working conditions. For all plasma focus devices with deuterium as filling gas, the values of energy densities are typically in the range of $(1 - 10) \times 10^{10}$ J/m^3 and the values of drive parameters are in the range of (77 ± 7) kA/cm.mbar$^{1/2}$. This is termed as "plasma focus scalability" which essentially means that plasma focus devices of all the energies have same characteristics i.e. density and temperature [Soto et al., 2010]. This means that a similar radiation spectrum, although at a different scale can be achieved with energies in the range vary from subkilo-joule to mega-joule. The scalability of the plasma focus devices has major implications in designing electrodes i.e. higher the capacitor bank energy and the peak discharge current, bigger will be the electrodes dimension. Similar, if capacitor bank energy is reduced to subkilo-joule range, then the electrodes dimension must be reduced to match the energy density and the current drive parameters.

The value of anode radius "a" is calculated using energy density i.e. $28E/a^3$ [Soto et al. 2010, Lee 1996]. The values of cathode radius "b" and anode length "z_0" are chosen to match the quarter discharge time-period i.e. $\pi/2(LC_0)^{1/2}$ with axial run down time of the plasma sheath as given in eq. (3.9). Here, values of L [$= L_0 + L_p$(axial)] can be estimated from short-circuit (electrodes shorted at tip) time-period. The optimum filling pressure is determined from experiments.

Ceramic insulators (Quartz, Pyrex glass, Alumina) are mostly used because of high melting point, low thermal expansion coefficient and high dielectric breakdown voltage. The length of the insulator is chosen to ensure uniform current sheath and therefore efficient snowplow of plasma and neutron gas ahead in the axial run-down phase. The effective length of insulator (over which the surface discharge takes place in breakdown phase) depends on operation voltage i.e. 2.5 mm per kV. [Zakaullah et al. 1995, Rout et al. 1995, Yusefi et al. 2007].

3.2 Sub-kilojoule range operating plasma focus device

Sub-kilojoule range operating devices having neutron yield of 10^3 to 10^6 neutrons/pulse are important for many applications including field applications such as soil humidity measurement, hidden material detection. The electrodes are of short dimensions for sub-kilojoule range operation according to plasma scalability. The cathode is of tube shape and it also works as plasma chamber which make them compact, portable and feasible for field applications. Two different plasma focus devices, SPF1-P2 and PF-P5, operating in sub-kilojoule range have been designed, developed and optimized for neutron emission. The details about their constructions have been discussed in the following section.

3.2.1 SPF1-P2 plasma focus device

3.2.1.1 200 J Capacitor bank

The capacitor bank of SPF1-P2 device consists of single capacitor (4 μF, 10 kV). The capacitor is of dimension: 18 cm × 15 cm × 13 cm and of weight: 6.5 kg. A triggerable spark gap switch is assembled at the top of the capacitor in a compact geometry. One of the spark electrodes is connected to high voltage terminal of capacitor and the other end (discharge end) is directly interfaced to the plasma focus load. The spark gap switch is housed inside an enclosure made of SS304.

The capacitor bank is charged by a battery based constant current supply through a remotely held control panel. The details of the supply have been described in the subsequent section. The total weight including the power supply and the control panel is 23 kg only. It is estimated from the short circuit measurement that the capacitor bank can deliver maximum peak current of 83 kA at 10 kV charging voltage. Typical parameters of 200 J capacitor bank for SPF1-P2 device are presented in table 3.1.

Table3.1: Typical parameters of 200 J capacitor bank

Capacitance (μF)	4
Inductance (nH)	44
Operating voltage (kV)	10
Energy (J)	200
Voltage reversal (%)	80
Time-period (μS)	2.7
Peak discharge current (kA)	83

3.2.1.2 Battery based high voltage power supply

Batteries based power supply is used to charge the capacitor bank. The input in the power supply is provided using two rechargeable batteries (each, 12 V, 150 Ah). The output voltage of maximum of 15 kV with adjustable current can be derived from the supply. It also supplies a negative trigger pulse of amplitude 30 kV and of less than 5 μs rise time. The overall dimension of the power supply is 28 cm × 24 cm × 20 cm. The power supply is remotely operated using a handheld control panel of size 28 cm × 12 cm × 12 cm. A photograph of the power supply along the control panel is shown in fig. 3.3.

FIG. 3.3 Photograph of battery based capacitor charging power supply.

3.2.1.3 Plasma focus

Plasma focus is a sealed tube which consists of two co-axial electrodes made of SS304. The inner diameter and effective length of the anode are of 10 mm and 20 mm respectively. The inner diameter and effective length of the cathode are of 29 mm and 50 mm respectively. The cathode also works as the plasma chamber. An alumina insulator of effective length of 12 mm separates the anode and the cathode. The volume of plasma chamber including the anode and the insulator is 33 cm^3. It is an all metal sealed tube and the metal to ceramic sealing is done by silver based active alloy brazing. The schematic of the sealed tube plasma focus is shown in fig. 3.4(a). A quarter inch bellow sealed valve (Swagelok mode: SS4BW) is connected to the nozzle of plasma chamber for evacuation and filling of the deuterium gas. The bellow sealed valve is then used to seal plasma chamber for long duration operation. The weight of the plasma focus unit is 0.5 kg. A photograph of the sealed tube is shown in fig. 3.4(b).

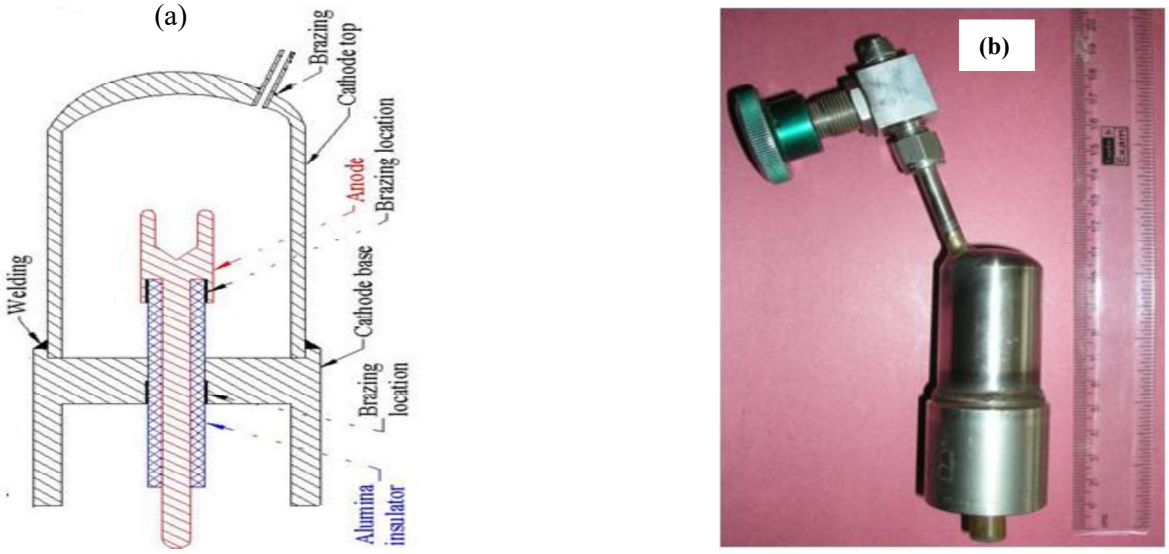

FIG. 3.4 (a) schematic and (b) photograph of sealed-tube.

A photograph of SPF1-P2 device is shown in fig. 3.5. The height of the plasma focus device along with the capacitor and the spark gap assembly is 29 cm. For operation, plasma focus tube is evacuated to a base pressure $\leq 10^{-5}$ mbar before filling with the optimum filling pressure. Once filled at optimum filling deuterium gas pressure (8 mbar), there has not been seen any drop or increase in filling pressure after 200 days. This makes this tube suitable for long duration operation without refilling.

FIG. 3.5 Photograph of sealed tube based SPF1-P2 plasma focus device.

3.2.2 Repetitive operating PF-P5 plasma focus device

3.2.2.1 500 J Capacitor bank

Single capacitor (10 μF, 30 kV) is used to drive the PF-P5 device. The dimension and weight of the capacitor is 24 cm × 34 cm × 50 cm and 50 kg respectively. A triggered spark gap is installed right above the capacitor with one end of the spark gap is connected to its high voltage terminal. The discharge end of the spark gap is attached to the plasma focus anode similar to SPF1-P2 device. The trigger pulse is provided at the center of the spark gap. The spark gap is enclosed using a cylindrical enclosure made of SS304.

The capacitor bank is charged to 10 kV using a repetitively charging supply. The peak current of 85 kA is estimated to be delivered to plasma focus at 10 kV charging voltage. Typical parameters of 500 J capacitor bank are depicted in table 3.2.

Table 3.2 Typical parameters of 500 J capacitor bank.

Capacitance (μF)	10
Inductance (nH)	110
Operating voltage (kV)	10
Energy (J)	500
Voltage reversal (%)	80
Time-period (μS)	6.6
Peak discharge current (kA)	85

3.2.2.2 Repetitive charging power supply

A repetitive charging power supply is used to charge and discharge the capacitor bank. This can charge up to maximum of 11 kV at the tunable repetition frequency of 1-10 Hz. The power supply also supplies negative trigger pulse of amplitude of 20 kV to the spark gap.

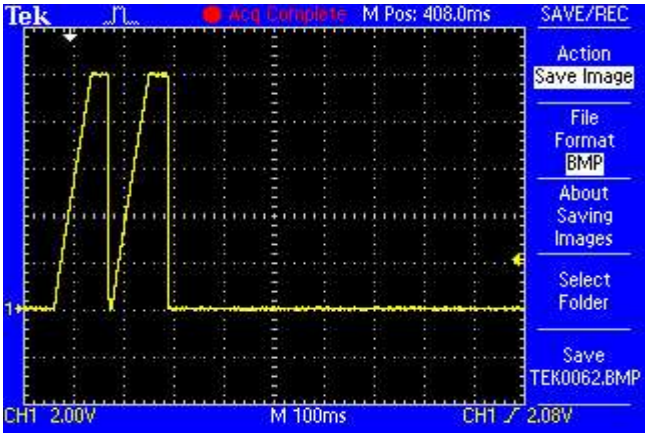

FIG. 3.6 Typical voltage profile for 2 shots at repetition rate of 10Hz.

The repetitive operation is achieved by sequentially synchronizing charging and sequentially providing the triggering pulse to the spark gap for switching purpose. The input to power supply is supplied through a three phase 420 V AC (20 A).

A typical charge-discharge cycle of the repetitive charging power supply for two cycles at repetition rate of 2 Hz is shown in fig. 3.6. The profile depicts the charging voltage as a function of time. At 10 Hz, the charge-discharge cycle consists of charging time (90 ms) during which the capacitor bank charges and then the dwell time (10 ms) during which the capacitor voltage is maintained at the preset operation voltage. The capacitor bank is then discharged on supply of trigger pulse to the spark gap.

3.2.2.3 Plasma focus

Plasma focus of PF-P5 device is of tubular geometry. The anode and the cathode are made of SS304. The diameter and effective (exposed) length of the anode are 10 mm and 60 mm respectively. The outer diameter and the effective length of the cathode are 50 mm and 120 mm respectively. The cathode also worked as the plasma chamber with a volume of 150 cm^3 including anode and insulator. An alumina tube of 10 mm diameter and 2 mm wall thickness separates the anode and cathode at the bottom. The effective length (length exposed to plasma) of alumina is kept at 20 mm. The alumina insulator is brazed to anode as shown in fig. 3.7a and between insulator and cathode silicon O-ring is used at the bottom for vacuum sealing. Schematic and photograph of PF-P5 device are shown in figs 3.7(a) and (b).

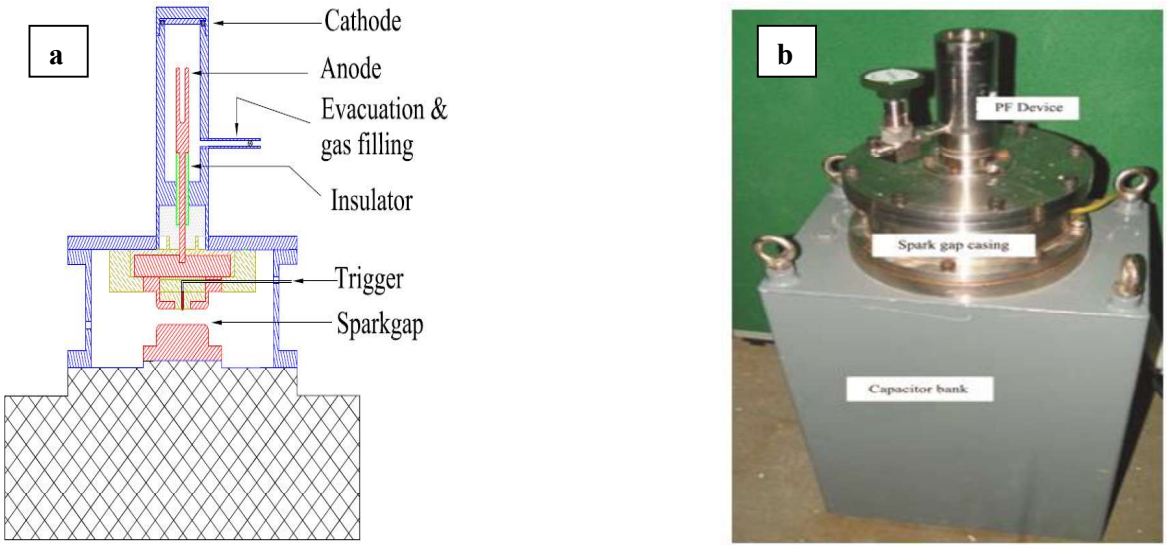

FIG. 3.7(a) Schematic and (b) photograph of repetitive operating PF-P5 device.

3.3. Kilo-joule range operating plasma focus device

Three different plasma focus devices, namely PF-2, MEPF-12 and MEPF-17 operating at energies 2 kJ, 11.5 kJ and 17 kJ have been developed and optimized. The construction and optimization of these plasma focus devices are discussed in details in the following section.

3.3.1 PF-2 plasma focus device

3.3.1.1 2 kJ Capacitor bank

Single capacitor (10 μF, 30 nH, 30 kV) is used to drive the PF-2 device. The dimension and weight of the capacitor are 24 cm × 34 cm × 60 cm and 50 kg respectively. A triggered spark gap is used to transfer the energy to the plasma focus. Parallel plate transmission lines are used to connect the capacitor to the spark gap switch and switch to the plasma focus. One end of the spark gap is connected to the capacitor and other one is directly interfaced to the plasma focus anode. A cylindrical casing made of SS304 is used as the enclosure for the spark gap switch. The plasma focus load is placed over this casing in a compact geometry. This type of connections makes the device easy in assembly and maintenance. The capacitor bank is charged to desired voltage using a constant

current power supply (22 kV, 15 mA). The power supply also supplies a negative trigger pulse of 25 kV and of < 1 μs rise time.

Electrodes of the PF-2 device are shorted at the tip for the short circuit measurements. The short shirt circuit time-period is measured to be 5.0 μs. The estimated inductance and peak discharge current are estimated to be 63 nH and 225 kA. A typical short circuit current derivative waveform is shown in fig. 3.8. Typical parameters of capacitor bank with short circuit peak discharge current are tabulated in table 3.3.

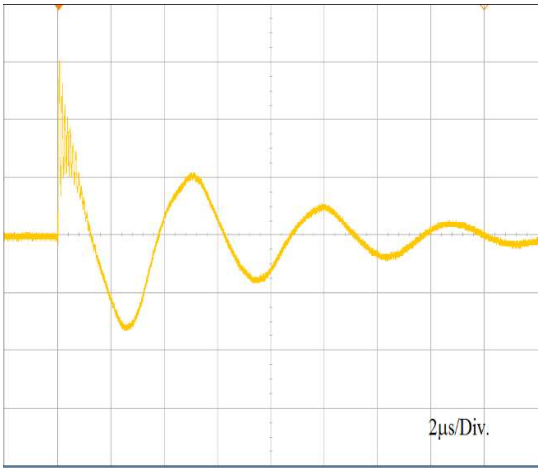

FIG.3.8 Typical short circuit current derivative waveform from PF-2 device.

Table 3.3 Typical parameters of 2 kJ capacitor bank.

Capacitance (μF)	10
Inductance (nH)	63
Operating voltage (kV)	20
Energy (kJ)	2
Voltage reversal (%)	80
Time-period (μS)	5
Peak discharge current (kA)	225

3.3.1.2 Plasma focus

Plasma focus unit in PF-2 device is of squirrel-cage geometry. The anode and the cathode are made of SS304 material. The diameter and the exposed length of the anode are 30 mm and 60 mm respectively. The cathode is in form of squirrel cage consisting of eight rods, each of 10 mm diameters. These rods are fixed around the anode at a diameter of 80 mm. The quartz tube of 25 mm diameter and 1.5 mm thickness covers the anode at the bottom. The length of quartz tube inside plasma chamber is 45 mm. The schematic and photograph of the PF-2 device are shown in figs 3.9(a) and (b).

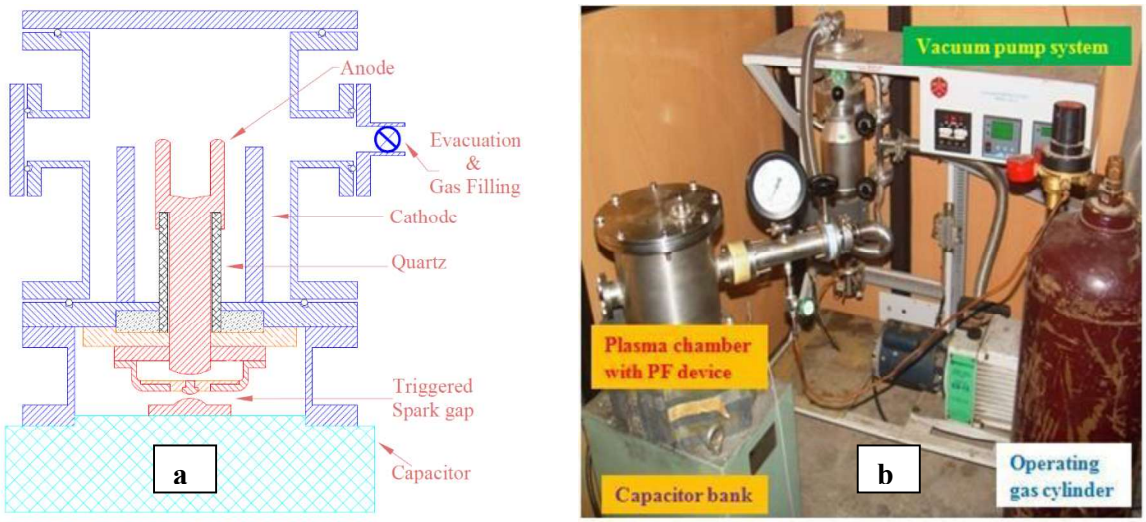

FIG. 3.9 (a) Schematic and (b)Photograph of PF-2 device.

3.3.2 MEPF-12 plasma focus device

3.3.2.1 11.5kJ Capacitor bank

The capacitor bank consists of four capacitors (each 10 μF, 30 nH, 24 cm × 34 cm × 60 cm, 50 kg). High voltage terminals of all four capacitors are connected using a plate of dimension (l × w × t): 400 mm × 300 mm × 12 mm and it is made of SS304 which is termed as “collector plate”. The grounds of all capacitors made common through a plate made of Brass of dimension: 700 mm × 450

mm × 2 mm (l × w × t). The ground and high voltage is separated using novel method. The ground plate is raised right above the high voltage plate using thirty-two brass rods, each of 12 mm diameters and 135 mm long. An edge triggered open-air spark gap switch is mounted in the gap between the high voltage and ground plates. One end of switch is screwed to the collector and other end to the plasma focus. Such connections make the setup easily demountable and transportable. This also allows easy access of spark gap switch assembly for regular maintenance work. The bank is charged using a constant current charging power supply (30 kV, 40 mA). The power supply also supplies negative trigger pulse of amplitude up to 50 kV to the spark gap switch.

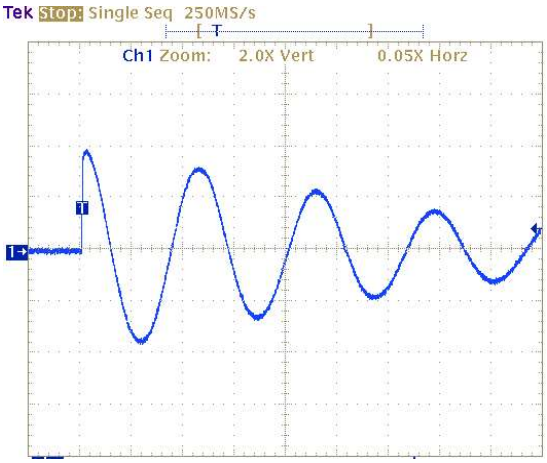

FIG. 3.10 Typical short circuit current derivative waveform from MEPF-12 device.

The anode and the cathode are shorted at the top for short circuit measurement. The short circuit time-period is measured to be 10.8 μs and the estimated inductance is 74 nH. Typical short circuit current-derivative waveform is shown in fig. 3.10. The maximum peak current estimated to be delivered to the plasma focus load is 499 kA at 11.5 kJ. Typical parameters of the MEPF-12 capacitor bank are presented in table 3.4.

Table 3.4 Typical capacitor bank parameters of 11.5 kJ capacitor bank

Capacitance (μF)	40
Inductance (nH)	74
Operating voltage (kV)	24
Energy (kJ)	11.5
Voltage reversal (%)	80
Time-period (μS)	10.8
Peak discharge current (kA)	499

3.3.2.2 Plasma focus

Plasma focus of MEPF-12 device is of squirrel cage geometry. The electrodes are made of SS304 material. The anode is of 77 mm effective length (exposed to plasma) and 60 mm diameter. The cathode consists of twelve rods, each of 12 mm diameter and 112 mm effective length. The rods are mounted at 122 mm pitch circle diameter around the anode. A quartz tube of 54 mm effective length and 54 mm outer diameter is placed over the anode at the bottom to separate it from cathode. The anode is of hollow shape at the top to minimize erosion due to impact of high energy electrons. The electrode assembly is put inside a high vacuum compatible experimental plasma chamber as shown in fig.3.11 (a). The plasma chamber is made of SS304 material and having volume of about 7.5 L. The chamber has four side ports with opening of 100 mm diameter each. Three of the ports are meant for the diagnostics and the fourth port is used for the evacuation and the gas filling. Fig. 3.11(b) shows photograph of the MEPF-12 device.

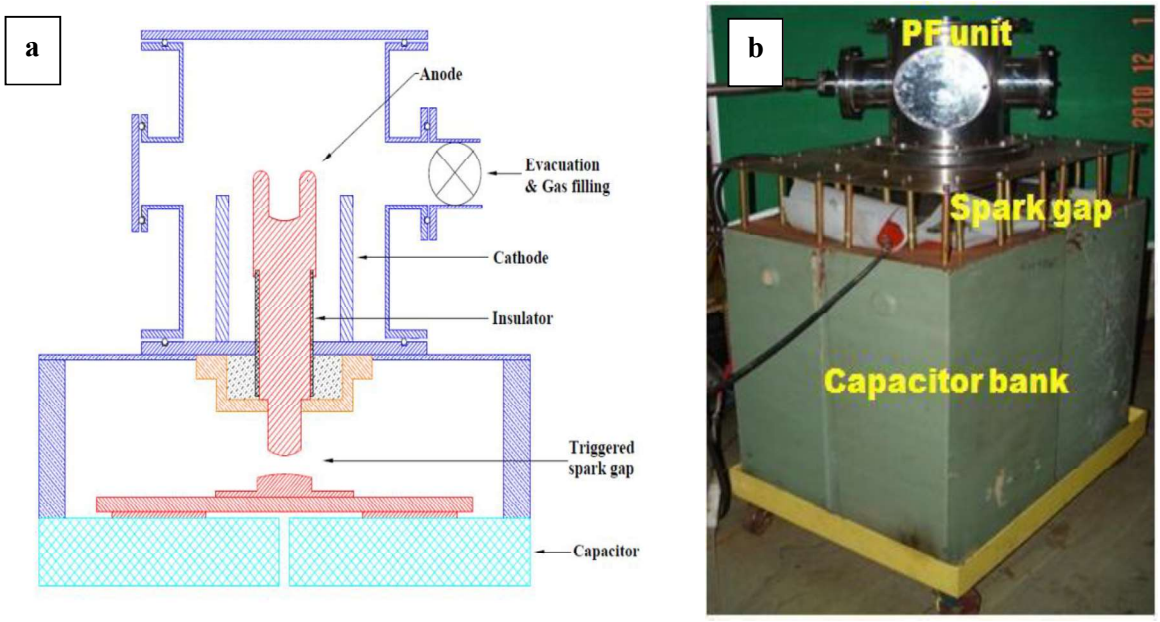

FIG. 3.11 (a) Schematic and (b) Photograph of MEPF-12 device.

3.3.3 MEPF-17 plasma focus device

3.3.3.1 17kJ Capacitor bank

The capacitor bank consists of six capacitors (each, 10 μF, 30 nH, 25 kV, 240 mm × 340 mm × 600 mm, 50 kg). High voltage terminals of all capacitors are connected using a common plate made of SS304 and of dimension: 560 mm × 410 mm × 12 mm (l × w × h). The grounds are made common using 2 mm thick and 25 mm wide brass strip. A center pin triggered spark gap switch is assembled right over the top of the capacitor bank. One end of the spark gap switch is screwed to capacitor bank and the discharge end is fixed to another plate connecting to the plasma focus load. Total forty-eight RG213 cables, each five-meter long, are used to connect the discharge end to plasma focus load. The capacitor bank is charged to the required voltage using a constant current power supply (40 kV, 60 mA). This also supplies the negative trigger pulse of amplitude up to 50 kV with rise time less than 1 μs.

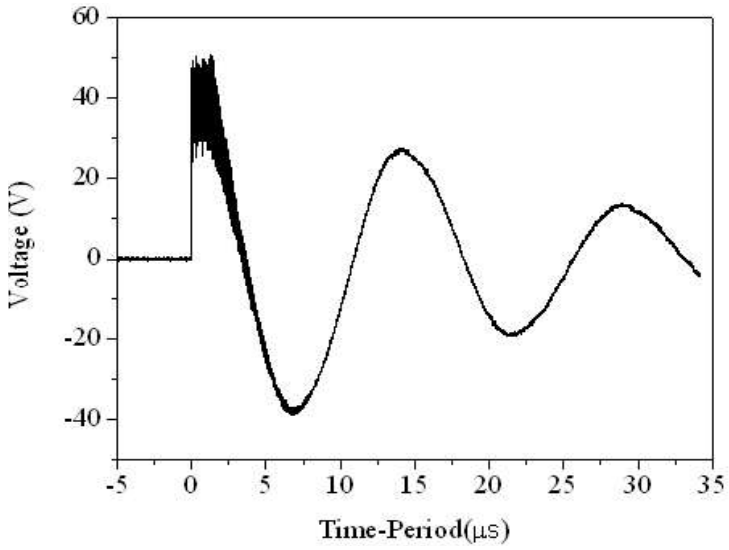

FIG. 3.12 Typical short circuit current derivative waveform from MEPF-17 device.

All forty-eight coaxial cables have been connected in steps. The short circuit inductance and current are estimated at each step. A typical short circuit current-derivative waveform is shown in fig. 3.12. The inductance decreases by a factor of 2.6 i.e. from 1080 nH for 2 cables to 421 nH for 6 cables. It further decreases by a factor of 2.5 i.e. to 169 nH for 24 cables. A plot of inductance with number of coaxial cables is shown in fig. 3.13. The variation of inductance (L) with number of cables is fitted using a power function as:

$$L = A + B.N^{C} \qquad \textbf{(3.10)}$$

where N is the number of RG213 cable. A, B and C are constants and their values are given in table 3.5. This closely matches with the expected variation of inductance of a system having fixed inductance A and N number of cables each of inductance B.

Forty-eight cables are chosen for the minimum possible inductance of the plasma focus system and for convenience in mechanical assembly. The short circuit time-period and the inductance with forty-eight cables are 16 μs and 108 nH respectively. Maximum current of 506 kA is estimated to be discharged to the plasma focus unit at 24 kV charging voltage. Typical capacitor bank parameters have been presented in table 3.6.

Table 3.5. Values of fitting parameter and standard error.

Constant	Value	Standard error
A	71.41	21.3
B	1962.03	74.3
C	-0.96	-0.06

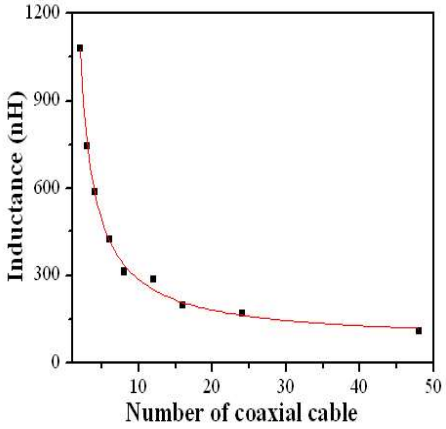

FIG. 3.13 Variation in short circuit inductance with no. of coaxial cables

Table 3.6 Typical parameters of 17kJ capacitor bank.

Capacitance (μF)	60
Inductance (nH)	108
Operating voltage (kV)	24
Energy (kJ)	17.3
Voltage reversal (%)	80
Time-period (μS)	16
Peak discharge current (kA)	506

3.3.3.2 Plasma Focus

Design parameters of plasma focus of MEPF-17 device is kept same as that of MEPF-12 device. The collector and ground plates are modified for connecting forty-eight RG213 coaxial cables in a compact assembly. The plasma chamber is made out of SS material. It has a volume of ~ 4.5 ltrs. This is high vacuum ($\leq 10^{-6}$ mbar) compatible. A side port in plasma focus chamber is used for evacuation and operation gas filling during operation. The weight of the plasma focus head along with the experimental plasma chamber is around 35 kg. The weight of all the coaxial cables is around 40 kg. Hence, relatively light weight of plasma focus head and flexibility of coaxial cables due to relatively long lengths allow the neutron source to be kept in any orientations specific to applications. This kind of arrangement is incorporated for the first time in a medium energy plasma focus device. The schematic and photograph of the MEPF-17 device are depicted in fig. 3.14 and fig. 3.15 respectively.

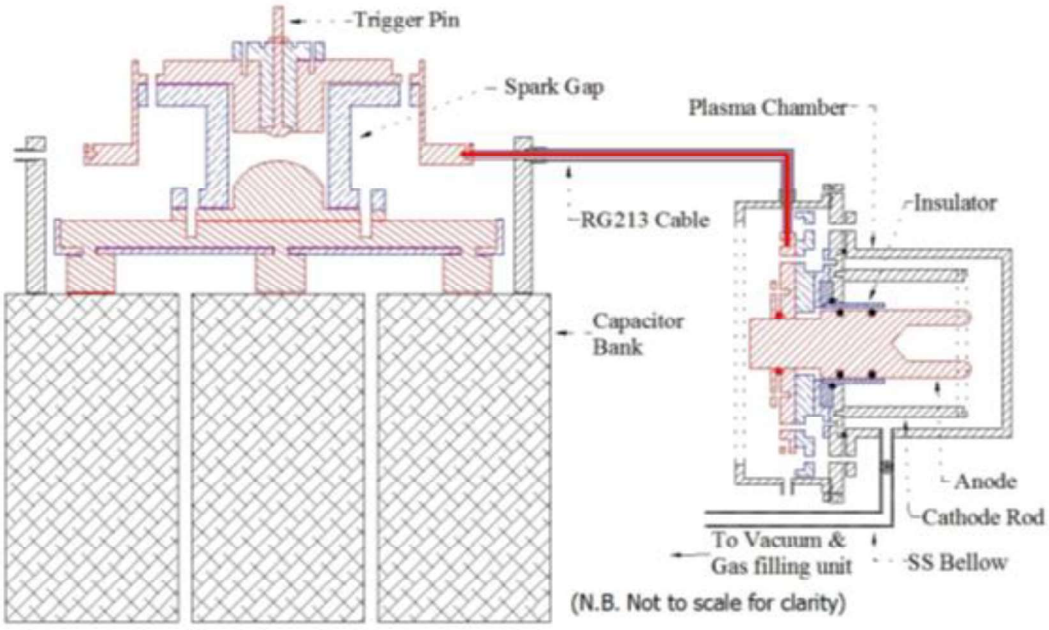

FIG.3.14 Schematic of MEPF-17 device

FIG. 3.15 Photograph of MEPF-17 device.

References

1. "A critical analysis and assessment of high power switches", Burkes T. R., Hagler M. O., Kristiansen M. et al., Texas Tech University, Lubbock, Texas, NP30/78, **1978**.
2. "Current and neutron yield scaling of fast high voltage plasma focus", Decker G., Flemming L., Kaeppeler H. J. et al., *Plasma Phys.,* **1980**, *22*, 245-260.
3. "PF-6 − an effective plasma focus as a source of ionizing radiation and plasma streams for application in material technology, biology and medicine," Gribkov V. A., Dubrovsky A. V., Scholz M., *Nukleonika,* **2006**, *51(1)*, 55−62.
4. "A scaling law for plasma focus devices", Krompholz H. , Ruhl F. , Schneider W. et al. *Phys. Lett. A,* **1981**, *82*, 82-84.
5. "Neutron Scaling Laws from Numerical Experiments", Lee S. and Saw S. H., *J. Fusion Energy,* **2008**, *27(4)*, 292-295.
6. "Dimensions and lifetime of the plasma focus pinch", Lee S. and Serban A., *IEEE Trans. Plasma Sci.,* **1996**, *24*, 1101-1105.

7. "D-D neutron yield in the 125 J dense plasma focus Nanofocus", Milanese M., Moroso R., Pouzo J., *Eur. Phys. J.,* **2003**, *27*, 77-81.

8. "Development and study of 13kJ capacitor bank and plasma focus device", Niranjan R., Rout R. K., Srivastava R. et al., *25th National Symp. Plasma Sci. Technol. (PLASMA-2010), Guwahati, India*, **2010**, 79.

9. "Note: A Portable pulsed neutron source based on the smallest sealed-type plasma focus device", Niranjan R., Rout R. K., Mishra P. et al., *Rev. Sci. Instrum.,.***2011**, *82*, 026104.

10. "The smallest plasma accelerator device as a radiation safe repetitive pulsed neutron source", Niranjan R., Rout R. K., Srivastava R. et al., *Indian J. Pure Appl. Phys.,* **2012**, *50*, 785.

11. "Influence of electrode and insulator materials on the neutron emission in a low energy plasma focus device," Rout R. K., Garg A. B., Shyam A. et al., *IEEE Trans. Plasma Sci.,* **1995**, *23(6)*, 996-1000.

12. "Battery powered tabletop pulsed neutron source based on a sealed miniature plasma focus device", Rout R. K., Mishra P., Rawool A. M. et al., *J. Phys. D: Appl. Phys.,* **2008**, *41*, 205211.

13. "Palm top plasma focus device as a portable pulsed neutron source", Rout R. K., Niranjan R., Mishra P. et al., *Rev. Sci. Instrum.,* **2013**, *84(6)*, 063503.

14. "Neutron emission from a fast plasma focus of 400 Joules," Silva P., Moreno J., Soto L. et al, *Appl. Phys. Lett.,* **2003**, *83*, 3269.

15. "New trends and future perspectives on plasma focus research", Soto L., *Plasma Phys. Control. Fusion,* **2005**, *47*, A361.

16. "Nanofocus: an ultra-miniature dense pinch plasma focus device with sub-millimetric anode operating at 0.1 J", Soto L., Pavez C., Moreno J. et al, *Plasma Sources Sci. Technol.,* **2009**, *18*, 015007.

17. "Studies on scalability and scaling laws for the plasma focus: similarities and differences in devices from 1MJ to 0.1J", Soto L., Pavez C., Tarifeno A. et al., *Plasma Sources. Sci. Technol.,* **2010**, *19*, 055017.

18. "A plasma focus driven by a capacitor bank of tens of joules," Soto L., Silva P., Moreno J. et al, *J. Phys. D: Appl. Phys.,* **2008**, *41*, 205215.

19. "Compact sub-kilojoule range fast miniature plasma focus as portable neutron source," Verma R., Roshan M. V., Malik F.et al, *Plasma Sources Sci. Technol.,* **2008**, *17*, 045020.

20. "Effect of cathode structure on neutron yield performance of a miniature plasma focus device", Verma R., Rawat R.S., Lee P. et al., *Phys. Lett. A,* **2009**, *373*, 2568–2571.

21. "Effect of the insulator length on Mather-type plasma focus devices", Yousefi H. R., Aghamir F. M. and Masugata K., *Phys. Lett. A,* **2007**, *361*, 360-363.

22. "Comparative study of low energy plasma focus devices", Zakaullah M., Murtaza G., Ahmad I. et al., *Plasma Sources Sci. Technol.,* **1995**, *4*, 117-124.

Chapter 4

Experimental Results and Discussion

4.0 Introduction

The plasma focus devices developed here are optimized for maximum radiation output for various applications. To maximize radiation output, effects of various parameters (electrical, geometrical as well as operational) on emission of radiations including neutrons and ions have been investigated. The correlation of neutron yield with electrical parameters (current and operation energy), geometrical parameters (electrodes dimensions and geometry) and gas filling pressure is experimentally studied in different plasma focus devices. For characterizing the SPF1-P2 device as a portable neutron source, quasi-continuous shots over long time-span are taken without purging the deuterium gas and reported [Niranjan et al. 2011]. It has been demonstrated that in SPF1-P2, neutrons are produced for maximum shots (more than 200 shots) and for longest time-span (more than 200 days) with single gas filling. Enhancement in time averaged neutron is achieved by PF-P5 device in a repetitive mode up to 10Hz [Niranjan et al. 2012].

The gas filling pressure and operation energy in MEPF-12 device are varied for time resolved measurements of neutrons and ions. Attempts are made to find correlation between emission of neutrons and ions. The spatial emission profile of ions in MEPF-12 device is experimentally studied at different gas filling pressure. In MEPF-17 device, the time resolved measurements of neutrons and hard X-rays in the axial and the radial direction in MEPF-17 device are performed and reported [Niranjan et al. 2016]. Anisotropies in neutron yield and its energy are also measured at different filling gas pressures. For characterization of PF-2 device as a compact source of ions and plasma, acetylene gas at various filling pressure is filled and optimized. The experimental investigations on time resolved emission of ions in PF-2, MEPF-12 and MEPF-17 have also been discussed in the present work.

4.1 Experimental results of SPF1-P2 device

The miniature, table top SPF1-P2 device is developed to study neutron emission over long time-span without refilling deuterium gas. Plasma focus chamber is evacuated to a base pressure of $\leq 10^{-5}$ mbar using rotary-diffstac pump before filling the deuterium gas. Two plastic scintillator detectors, each kept inside a cylindrical casing made of lead of 25 mm thickness are employed to record time-resolved neutron emissions. The hard X-rays from the plasma focus get significantly attenuated by the lead. This is also confirmed by operating the plasma focus with Hydrogen gas. They are placed at two different locations, 0.2 m and 1.2 m from plasma focus in the radial direction. The neutron signals recorded in the two detectors are used to estimate neutron yield.

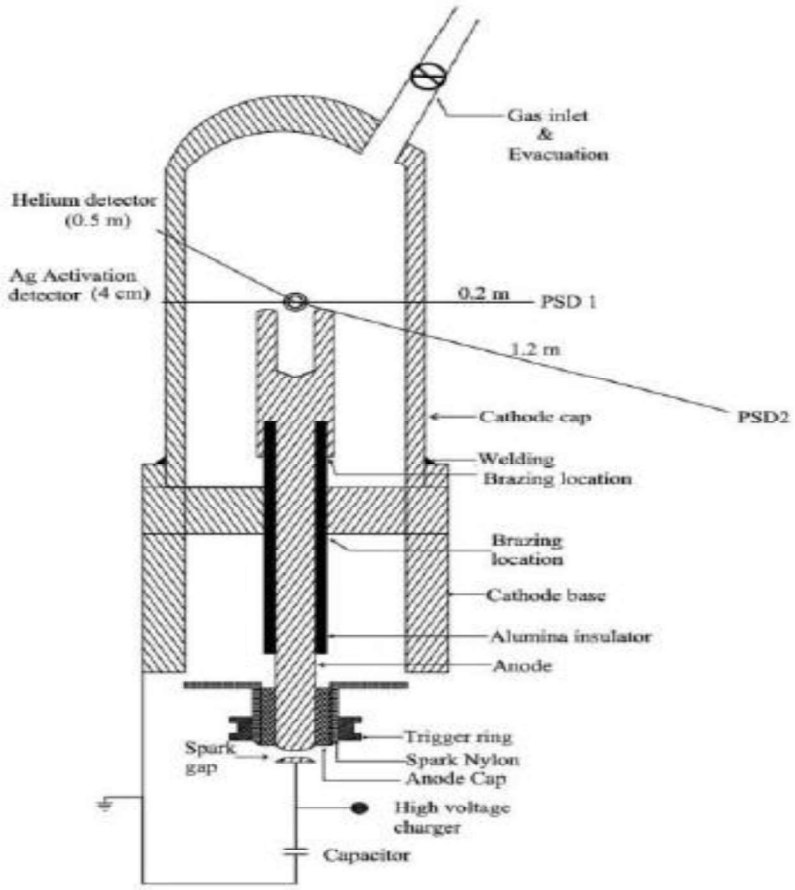

FIG. 4.1 Schematic of SPF1-P2 device with diagnostics.

energy using TOF method. A ^{3}He detector is located at 0.5 m in the radial direction to record neutron yield. The schematic of plasma focus device with diagnostics is depicted in fig. 4.1.

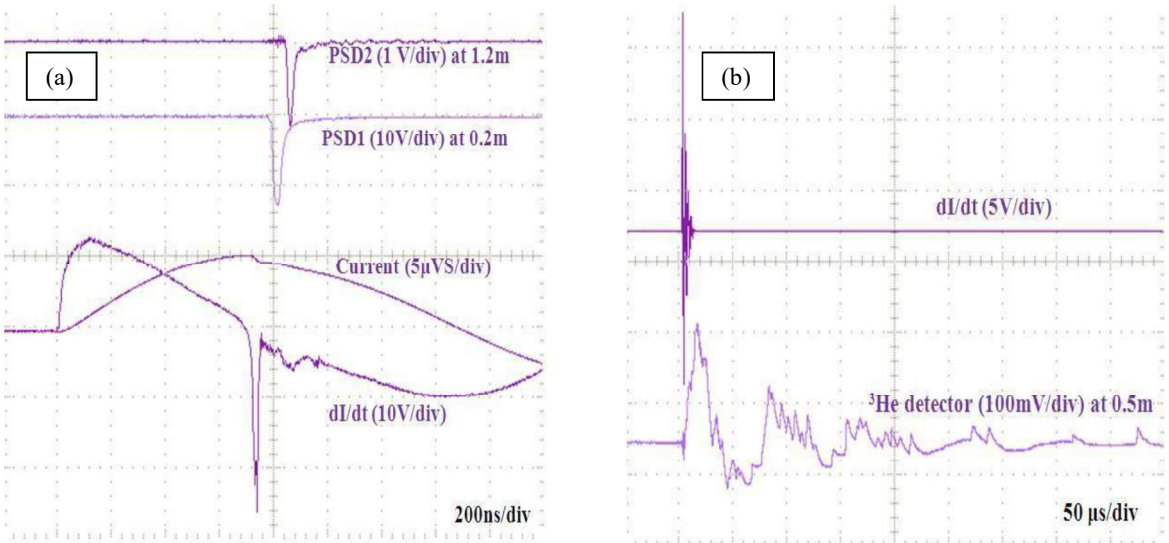

FIG. 4.2(a)Typical signals of current derivative, current and neutron and (b) Typical current-derivative and neutron from SPF1-P2 device.

Initially, a few shots are taken at low filling pressure (1 mbar) at operation energy of 200 J for conditioning of insulator surface. The sharp dip in the current derivative signal is observed after six shots. The filling pressure is varied in the range of 1 - 10 mbar to obtain optimum pressure of operation. In each shot, plasma chamber is evacuated and fresh filled with deuterium gas. The optimum pressure is found to be 8 mbar. Typical signals of the current derivative, current and neutron (recorded using two PSDs) are shown in fig.4.2(a). Single pulse of neutrons in both PSDs is observed corresponding to strong pinch observed in current derivative and current waveforms. Fig. 4.2(b) presents the typical signals of the current derivative and neutron pulse (registered by ^{3}He detectors). The repetitive pulses in ^{3}He detector are manifestation of the fact that the pulse fast neutrons generated in the PF shot are dispersed in time (several hundred of μs) in the moderator material as discussed in section 2.2.2.

The neutron yield is measured to be maximum of $(7.8 \pm 0.7) \times 10^4$ neutrons/pulse with a pulse width (FWHM) of (24 ± 5) ns at a filling pressure of 8 mbar. The average neutron energy estimated using signals from two PSDs is (2.49 ± 0.27) MeV. The average values are obtained using ten shots at optimized operation conditions with fresh filling in each shot. The expected neutron yield as per scaling law is 2.9×10^6 neutrons/pulse (peak current 83 kA). The possible reason for the difference between observed and expected neutron yield could be attributed to the use of tubular cathode. The operation with tubular cathode increases the current leakage i.e. the fraction of peak discharge current that actually flows through plasma sheath is less which in turn reduces the neutron yield. Also in operation with tubular cathodes, addition of impurities (due to back reflected particles from the cathode wall) during the axial flow, may result in a substantial drop in temperature due to increased radiation loss which is also consistent with the reduction in neutron output. Similar observations were by reported by Verma et al. [2009].

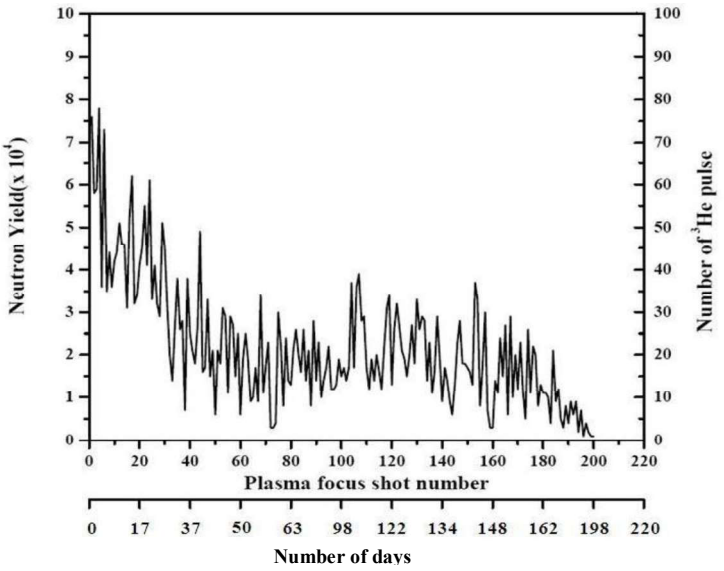

FIG. 4.3 Variation in neutron yield of SPF1-P2 device with shots and days.

Once optimized for its neutron emission, SPF1-P2 device is evacuated to a base pressure of $\leq 10^{-5}$ mbar and then it is filled with deuterium gas at optimum pressure of 8 mbar. The SPF1-P2 device was sealed using a bellow-sealed valve (Swagelok SS-4BW) for continuous operation without

refilling deuterium gas. The emission of neutrons from SPF1-P2 device is observed in about 200 shots over a time-span of around 200 days with a single filling. The average 2 to 3 PF shots on normal working days are taken. The variation in neutron yield over the number of shots as well as number of days is plotted as shown in fig. 4.3. Neutron yield is observed to be deteriorating in subsequent shots. The possible reason could be the impurities inserted into plasma due to electrode material erosion during axial acceleration phase of current sheath and in post pinch phase in every PF shot as well as accumulation of hydrogen and ^{3}He ashes [Burns et al 1988], the products of the D-D nuclear fusion, over PF shots.

The average neutron yield for first 50 shots is estimated to be $(3.8 \pm 1.7) \times 10^4$ neutrons/pulse while it has decreased to $(1.9 \pm 0.8) \times 10^4$ neutrons/pulse in next 100 shots. In the last 50 shots, the yield is seen to be decreased further to (1080 ± 30) neutrons/shot. The yield values further represent the average of best 10 shots in respective group of that. The dip in the current-derivative signal is observed even after 200 shots but neutron signal is not observed in ^{3}He detector. This is due to the reason that neutron yield is below the detection threshold of ^{3}He detector [(1080±30) neutrons/pulse at 0.5 m]. There are six out of total 200 shots where dip in the current-derivative are not observed due to mis-fire of the spark gap and therefore neutrons are not produced. After cleaning spark gap electrodes, the device is again consistently operated for neutron emission. After completion of 200 shots, the device can again be evacuated and refilled with deuterium gas at 8 mbar optimum pressure for another long duration operation.

4.2 Experimental results of PF-P5 device

The plasma focus device, PF-P5 is characterized for enhancement in neutron yield by operating repetitively. Time resolved measurement of neutron emission (along with X-rays) is performed using a PSD detector placed at 30 cm from plasma focus in the radial direction. A SAD detector is placed at 10 cm from plasma focus in the radial direction to measure neutron yield. The

plasma chamber is evacuated to a base pressure of $\leq 10^{-5}$ mbar before filling deuterium gas. The optimum gas filling pressure is measured to be 5 mbar at 500 J. The neutron yield of $(1.3 \pm 0.2) \times 10^5$ neutrons/shot (1 shot = 1 pulse) with pulse duration of (22 ± 5) ns. The expected neutron yield as per scaling law is 3.1×10^6 neutrons/pulse (85 kA peak discharge current). The possible reason for the difference between observed and expected neutron yield could be attributed to the use of tubular cathode as discussed in section 4.1.

The PF-P5 device is operated for single and multiple shots (at repetition frequency of 10 Hz). Typical voltage on the capacitor bank in a single shot operation is shown in fig. 4.4(a). As shown, the power supply charges the capacitor bank to 10 kV in 90 ms, holds the voltage for around 10 ms till the arrival of trigger pulse by which capacitor bank is discharged through plasma focus. In fig. 4.4(b) typical signals of the current-derivative and time resolved hard X-rays and neutrons are presented. The first and second pulses recorded in PSD are of hard X-rays and neutron. The hard X-rays and neutrons are produced at the same time but get separated due to the difference in TOF of the two. The difference in TOF is used to estimate energy of neutrons in the radial direction. The energy of neutrons in the radial direction is estimated to be (2.45 ± 0.3) MeV.

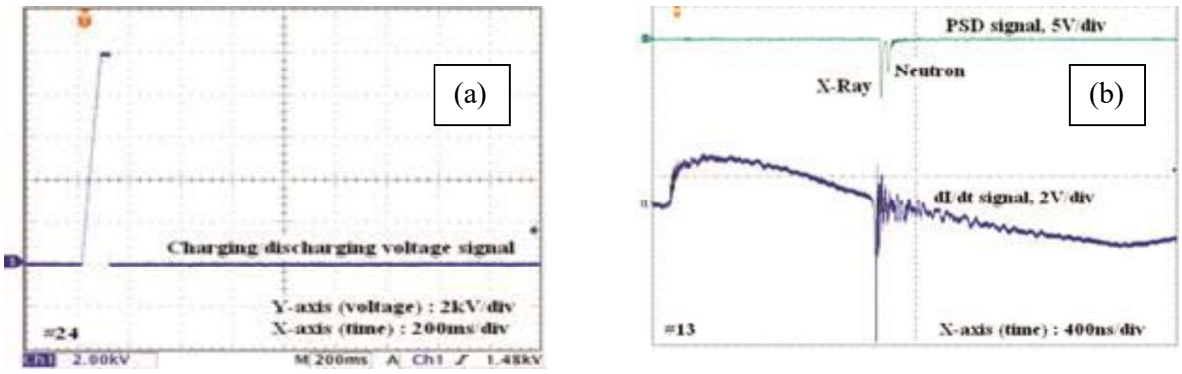

FIG. 4.4 (a)Typical charge-discharge voltage signal and (b) current-derivative waveform and neutron signal measured from the PF-P5 device when operated for single shot .

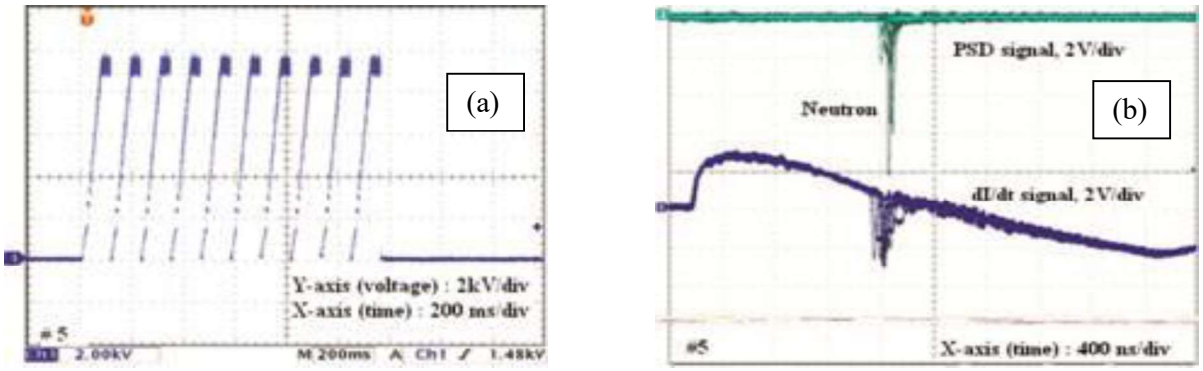

FIG. 4.5(a) Typical voltage across capacitor bank and (b) typical signals of current-derivatives and neutrons in ten shots.

For repetitive shots, PSD is placed inside a cylindrical casing made of 25 mm thick lead to record neutron signals only. Fig. 4.5(a) shows typical voltage across the capacitor bank and fig. 4.5(b) shows typical signals of current derivatives and neutrons when operated for ten repetitive shots. The area under neutron pulse is calculated to estimate neutron yield in each shot. The neutron yield/pulse is observed to be varying but the time average neutron yield is enhanced to $(1.4 \pm 0.3) \times 10^6$ neutrons/shot (1 shot=10 pulse). The possible reason of variation in neutron yield/pulse could be impurities and fraction of peak bank current that flows through plasma which may vary from shot to shot [Shyam et al. 1997].

4.3 Experimental results of PF-2 device

4.3.1 Optimization study

For characterization of PF-2 device as an ion and plasma source, it has been operated with different gases e.g. deuterium and acetylene (C_2H_2). The plasma chamber is evacuated to a base pressure of $\leq 10^{-5}$ mbar before filling with working gas. Various characteristics e.g. current derivative, time resolved hard X-rays and time resolved ion emission are measured using Rogowski coil, PSD detector and Faraday cup respectively. A PSD detector is kept at 2 m in the radial direction of plasma

focus. The filling pressure of deuterium and acetylene are varied from 0.5 to 5 mbar. The optimum filling pressures of deuterium and acetylene gas are found to be 1 mbar and 0.5 mbar respectively. Typical current-derivative waveform and X-rays are shown in fig. 4.6. with acetylene filling gas. The pulse duration (FWHM) of hard X-rays was measured to be (25 ± 5) ns at acetylene filling pressure of 0.5 mbar.

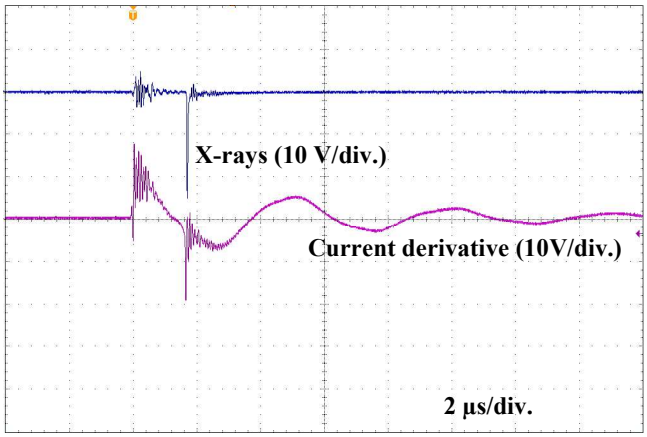

FIG. 4.6 Typical current derivative waveform and X-rays signal from PF-2 device.

4.3.2 Ion emission from PF-2 device

Time resolved measurements of ions in PF-2 device are performed when operated with deuterium filling gas. A Faraday cup is placed at 5 cm from the anode in the axial direction. It is biased at -100 V. Typical signals of current-derivative and ions are shown in fig. 4.7. It is seen that ion pulse consists of a small hump followed by a distinct high amplitude peak. This hump is seen to be coincident with the dip in current derivative and it is termed as photo-peak since it is possibly generated by the photoelectric effect caused by soft X-rays [Ghareshabani et al. 2010]. The time of the photo-peak is taken as time at which the ions are accelerated. To confirm the ion pulse, the entrance of pinhole was blocked using Al foil filters of 50 µm thick to cut-off ions and also to see effects of electromagnetic radiations. There was no pulse except some noise coincident to dip in

current derivative signal observed in Faraday cup with this. In order to reduce the electromagnetic noise, the BNC connections was shielded with grounded Al foils. Typical ion fluence is measured to be $(8.7 \pm 0.5) \times 10^{14}$ cm^{-2} at 1 mbar. The effects like ablation plasma produced on the entrance aperture of the Faraday cup [Kelly et al. 1998], impurity ions emitted due to the interaction of electrons to anode tip [Pimenov et al. 2006] have been ignored while calculating the ion fluence.

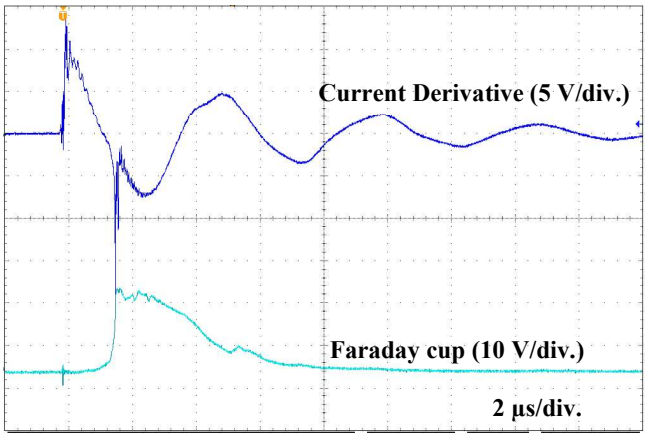

FIG. 4.7 Typical signals of current derivative and ion pulse from PF-2 device.

4.4 Experimental results of MEPF-12 device

The MEPF-12 is characterized as neutron and ion source to understand various physical processes as well as applications. The plasma chamber of MEPF-12 device is evacuated to a base pressure of $\leq 10^{-5}$ mbar before filling it to required pressure. Various diagnostics employed are e.g. Rogowski coil, silver activation detector, PSD detector and Faraday cup to measure current derivative, neutron yield, time resolved neutron emission and time resolved ion emission respectively. Initially, a few shots are taken at a filling pressure of 2 mbar and at a capacitor bank charging voltage of 20 kV for conditioning of insulator. On observation of dip in the current derivative signal, the optimum filling pressure is obtained by operating at varying deuterium gas filling pressures (1 - 10 mbar). The

optimum filling pressure is found to be 4 mbar at an operation energy of 11.5 kJ. Typical signals of current-derivative and neutrons along with hard X-rays are shown in fig. 4.8.

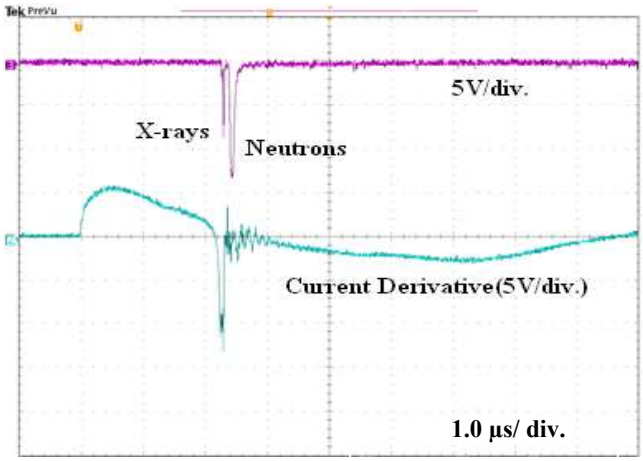

FIG. 4.8 Typical signals of current derivative, hard X-rays and neutrons MEPF-12 device.

The maximum neutron yield is measured to be $(1.2 \pm 0.3) \times 10^9$ neutrons/pulse with pulse duration of (46 ± 5) ns at 4 mbar and 11.5 kJ which is close to the estimated neutron yield of 1.1×10^9 neutrons/pulse at 499 kA peak discharge current using scaling laws for neutrons. The neutron energy estimated from the time of flight is (2.45 ± 0.20) MeV.

The filling deuterium gas pressure and the operation energy are varied and their effects on time resolved emissions of ion and neutron are studied. Faraday cup is kept at 14 cm from the anode tip in the axial direction and silver activation detector is placed at 1.5 m from the plasma focus in the radial direction. The biasing voltage applied to the Faraday cup is -100 V for all shots. For time resolved measurements of ions, filling pressure is varied from 1 to 10 mbar at 9.7 kJ while operation energy is varied from 3.9 to 9.7 kJ at 4 mbar. Typical ion pulse and current-derivative waveform are shown in fig. 4.9. As seen from fig. 4.9, the ion pulse consists of a small hump (photo-peak) followed by a main peak. The time of the photo-peak is taken as reference to estimate energy of ion using TOF method. The area under ion pulses is evaluated to estimate the ion fluence.

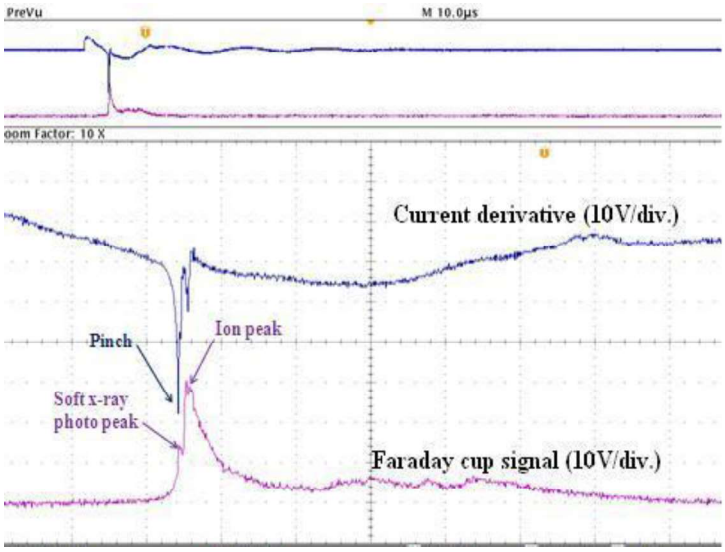

FIG. 4.9 Typical signals of current derivative and ions from MEPF-12.

The pinch in the current derivative signal is observed consistently in each shot up to filling pressure of 10 mbar, beyond which focus is not observed consistently (either mild focus or no focus is observed). Hence, ion characteristics are estimated in filling pressure range of 1 to 10 mbar. Typical Faraday cup signals obtained at different filling pressures have been shown in fig. 4.10. Ion pulses at some filling pressure consist of main peak followed by many small humps and sometime two different ion peaks. The main ion peak is always correlated to dip in the current derivative. Strong and sharp dip in the current derivative signal result into high density of energetic ions. It can be attributed to instability induced acceleration of ions after onset of pinch disruption phase [Gary et al. 1974]. The possible reason of the other small peaks could be the low energy ions being trapped inside the magnetic field and escaping at different instants. Fig. 4.11 presents typical ion pulses observed at different operation energies and at a filling pressure of 4 mbar.

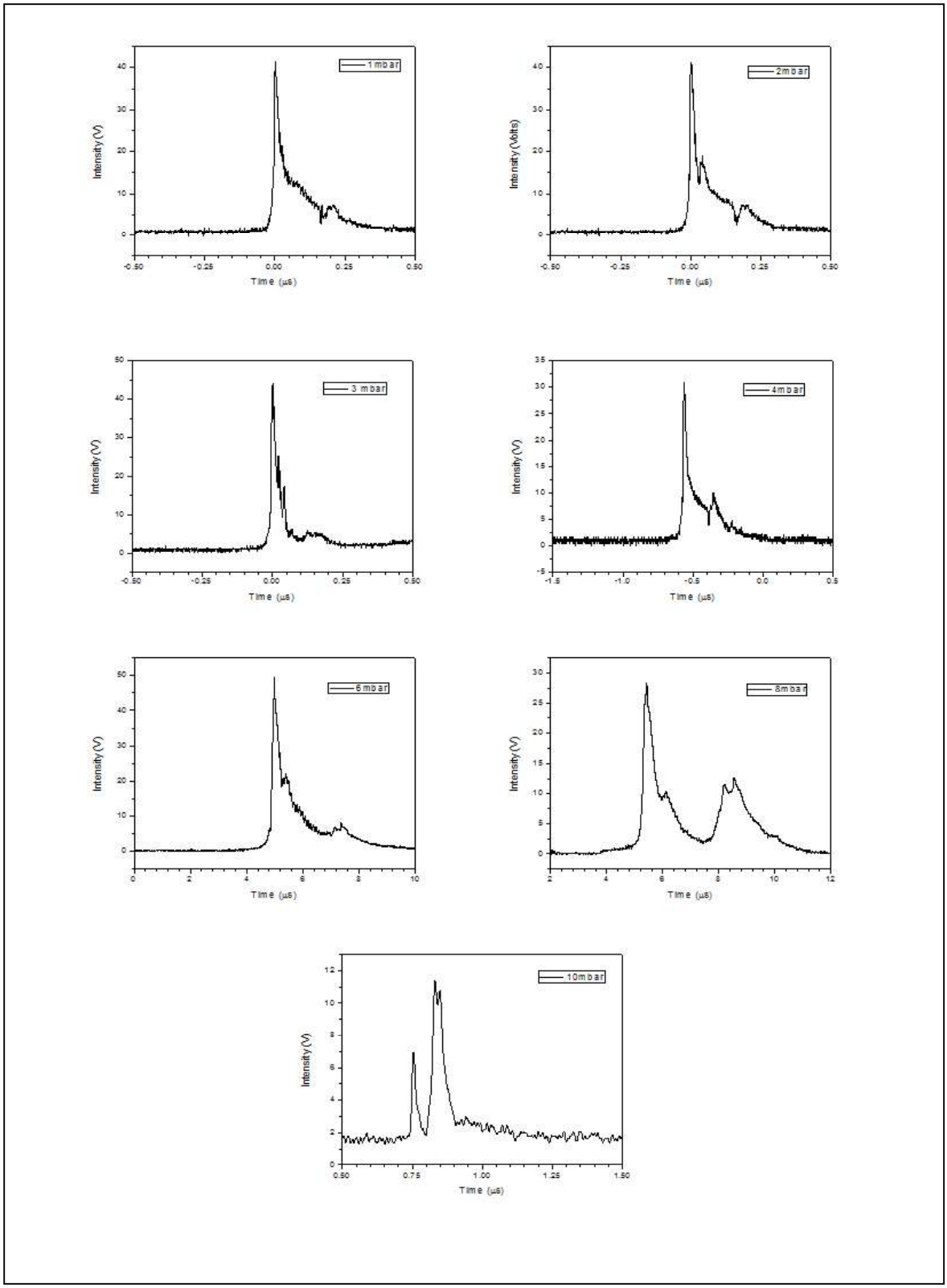

FIG. 4.10 Typical Faraday cup signals in deuterium gas filling pressure range of 1 - 10 mbar.

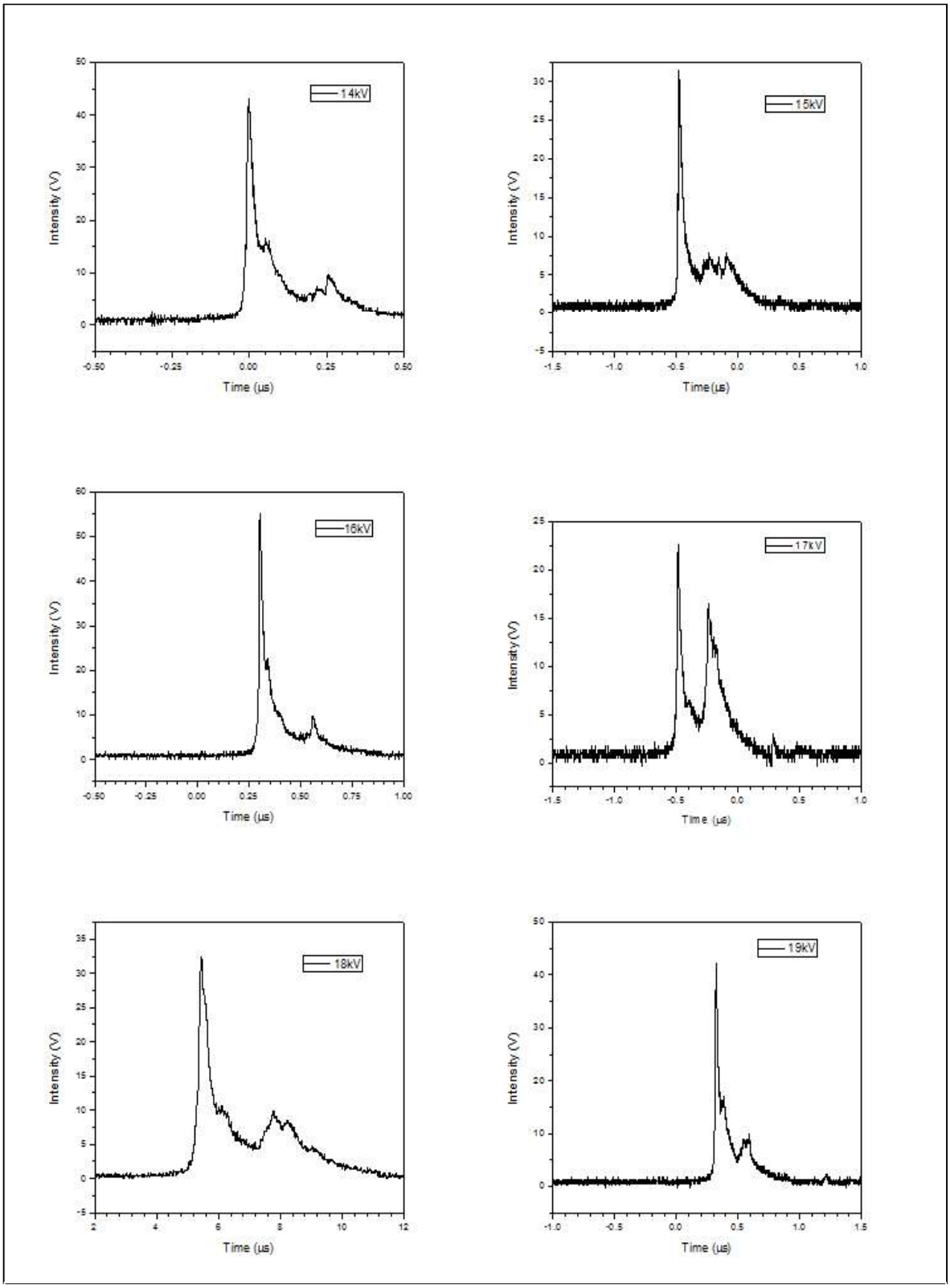

FIG. 4.11 Typical Faraday cup signals at different operation energy range of 3.9 – 9.7 kJ.

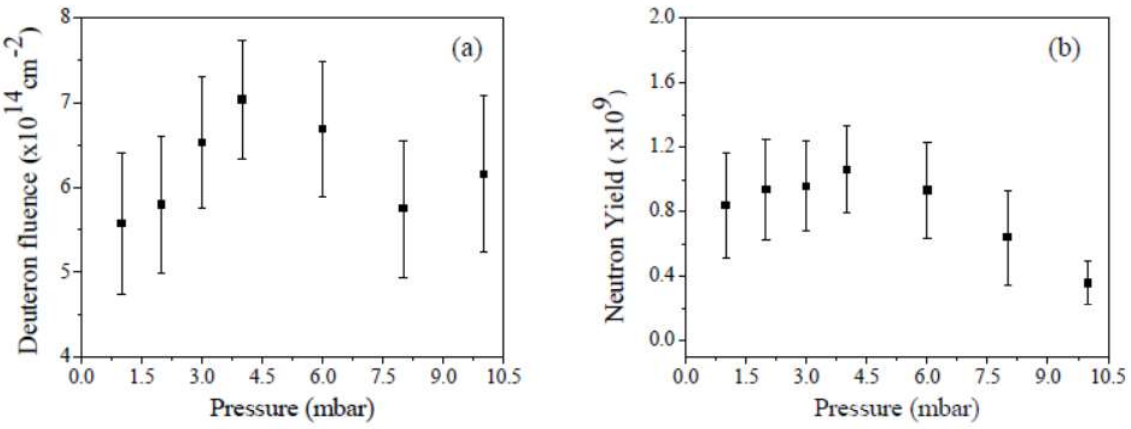

FIG. 4.12 Variations in (a) deuteron fluence and (b) neutron yield with deuterium gas filling pressures at 9.7 kJ.

The ion characteristics like ion fluence, peak ion number density and most probable ion energy are estimated at each filling pressures using Faraday cup signal. The deuterium ion fluence is observed to be varying with filling pressure. Variation in deuterium ion fluence with filling pressure is shown in fig. 4.12(a). The value of deuterium ion fluence is found to be maximum of $(7.0 \pm 0.7) \times 10^{14}$ cm^{-2} and minimum of $(5.7 \pm 0.8) \times 10^{14}$ cm^{-2} at 4 mbar and 8 mbar respectively. The pulse duration [full width at half maximum (FWHM)] is measured to be in the range of 190 ns to 440 ns over the filling pressure range. Variation in deuteron fluence (w. r. t. maximum value) is 19% for filling gas pressure range of 1 - 10 mbar. It appears that the observed variation in ion fluence with filling pressure is not significant as it is possibly because of well-known poor shot to shot reproducibility under apparently identical operating conditions (electrodes geometry, pressure, voltage). [Calkeret al. 1985, Bruzzone et al. 2008, Tarifeno-Saldiviaa et al. 2012]. Variation in current flowing through plasma (capacitor bank discharge current – leakage current) is one of the several other reasons such as multiple weak pinch formations instead of single and strong focus formations, impurities as well as error in measurement techniques that may be attributed for shot to shot variation. Considering this, it may be concluded that deuterium ion fluence is nearly independent of filling gas pressure range of 1 - 10 mbar.

The peak number density and most probable energy of deuterium ions are found to be increasing with increase in filling pressure and they reach a maximum at 4 mbar. Beyond 4 mbar, they decrease with further increase in filling pressure as seen in fig. 4.13(a) and (b) respectively. The maximum values of peak deuteron number density and most probable deuteron energy are found to be $(6.7 \pm 0.7) \times 10^{12}$ cm^{-3} and (228 ± 34) keV respectively. These variations led to variation in the neutron yield at each filling pressure.

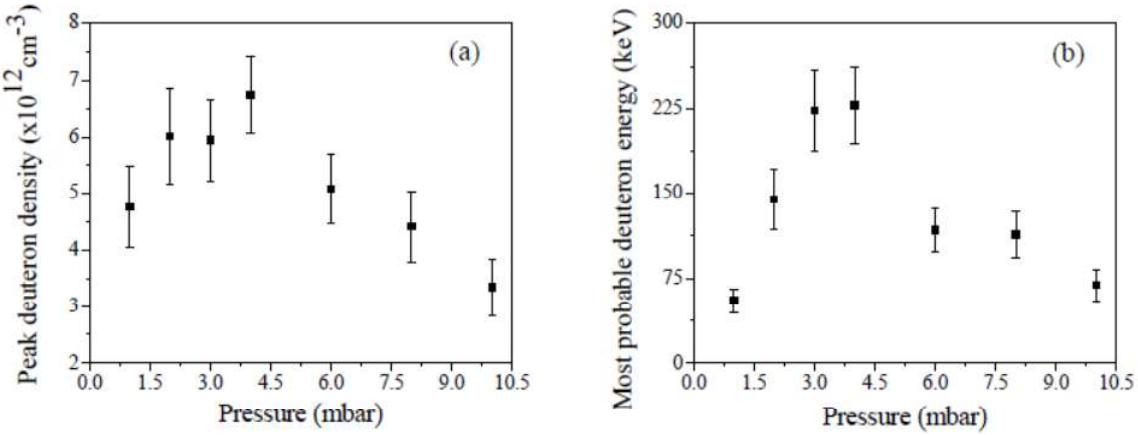

FIG. 4.13 Variation in (a) peak deuteron density and (b) most probable deuteron energy with deuterium gas filling pressure at 9.7 kJ

The neutron yield is seen to be varying from $(8.4 \pm 0.3) \times 10^{8}$ neutrons/shot over 4π Sr at 1 mbar to $(3.6 \pm 1.4) \times 10^{8}$ neutrons/shot over 4π Sr at 10 mbar. The maximum neutron yield of $(1.1 \pm 0.3) \times 10^{9}$ neutron/shot with pulse duration of (42 ± 6) ns is measured at 4 mbar. The variation in neutron yield with filling pressure at operation energy of 9.7 kJ has been shown in fig. 4.12(b).

The deuterium ion fluence measured over operation energies ranging from 3.9 kJ (14 kV, 40 μF) to 9.7 kJ (22 kV, 40 μF) has similar trend as that for filling gas pressures. Variation in deuterium ion fluence with operation energies (capacitor charging voltage) is shown in fig. 4.14(a). The deuterium ion fluence varies from $(7.3 \pm 1.1) \times 10^{14}$ cm^{-2} to $(7.0 \pm 0.7) \times 10^{14}$ cm^{-2} in the given

operation energy range. The maximum ion fluence is found to be $(8.1 \pm 0.9) \times 10^{14}$ cm^{-2} at charging voltage of 18 kV. The ion pulse duration (FWHM) varies from 240 ns to 340 ns. Variation in deuterium ion fluence is 13% (w.r.t. maximum deuterium ion fluence) over operation energy range. This again appears to be not significant which suggests that variation in deuterium ion fluence does not really depend on operation energy. It could also be a result of well-known poor shot to shot reproducibility of the plasma focus device as mentioned earlier.

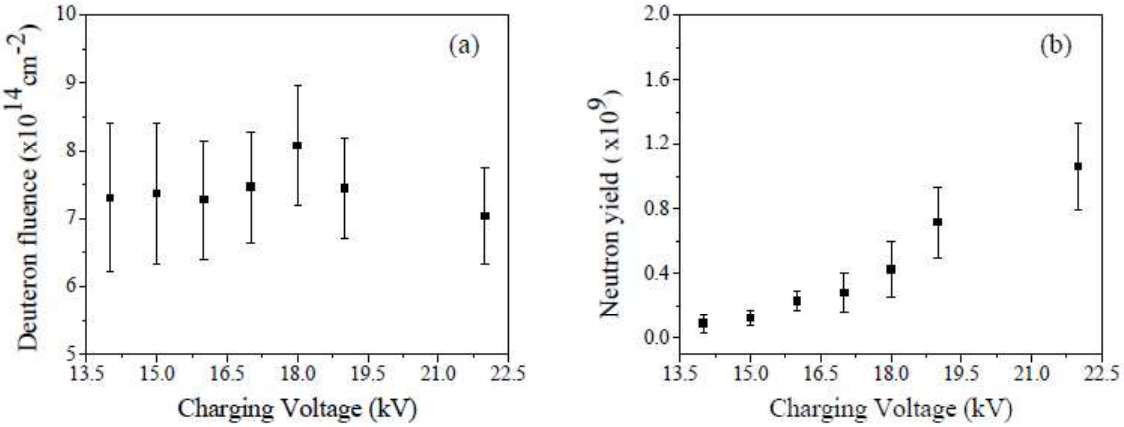

FIG. 4.14 Variations in (a) deuteron fluence and (b) neutron yield with operation energy at 4 mbar.

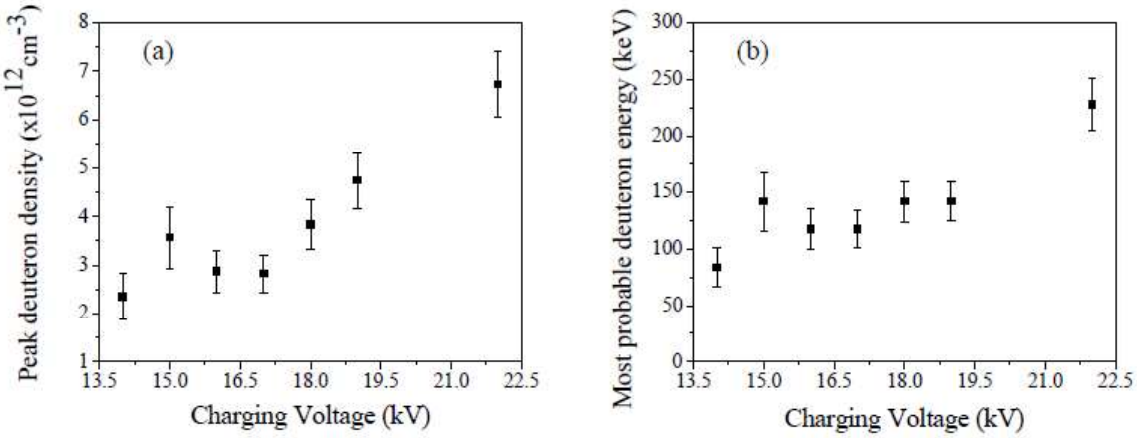

FIG. 4.15 Variation in (a) peak deuteron density and (b) most probable deuteron energy with operation energy at 4 mbar.

The peak number density and most probable energy of deuterium ions are found to be increasing with increase in operation energy as shown in fig. 4.15(a) and (b) respectively. The minimum and maximum values of peak deuteron number density are found to be $(2.3 \pm 0.5) \times 10^{12}$ cm^{-3} and $(6.7 \pm 0.7) \times 10^{12}$ cm^{-3} at 3.9 kJ and 9.7 kJ respectively. The minimum and maximum values of the most probable deuteron energy are found to be (84 ± 17) keV and (228 ± 34) keV and at 3.9 kJ and 9.7 kJ respectively. The neutron yield increases from $(9.1 \pm 5.6) \times 10^{7}$ neutrons/shot at 3.9 kJ to $(1.1 \pm 0.3) \times 10^{9}$ neutrons/shot at 9.7 kJ. Variation in the neutron yield with operation energy is shown in fig. 4.14(b). Variation in neutron yield is due to change in density and energy of deuterium ions with operation energy.

Measurements of deuterium ion fluence, peak ion number density, most probable deuterium ion energy and their correlation to neutron yield confirms that beam-target fusion is the main mechanism of neutron production in plasma focus device. The beam-target neutron yield is approximated as:

$$\sim \int n_D(v)\, n_0\, \sigma(v)\, v dv \qquad \textbf{(4.1)}$$

Here, $n_D(v)dv$ is velocity distribution of deuterium ions, v is the deuterium ion relative velocity w. r. t. neutral deuterium atoms/molecules, which are assumed to be at rest, σ is fusion cross section and n_0 is number density of background deuterium gas in the plasma chamber. The variation in neutron yield suggests that the deuterium ion velocity distribution, $n_D(v)dv$ is different at different filling pressure/operation energy. Moreover, it can also be inferred that, although ion fluence is nearly independent of filling pressures and operation energies, it is variations in number density and energy of ions which is resulting into variation in neutron yield as estimated by eq. 4.1. In order to substantiate this fact anisotropy in neutron yield/energy i.e. ratio of neutron yield/ energy in the axial direction to that of in the radial direction is measured using MEPF-17 device described in next section.

The values of deuterium ion fluence closely match with the reported results as discussed further. **Stygar et al. 1982** experimentally measured deuterium ion fluence in a plasma focus operating at 12.5 kJ using the SSNTD technique and the value they obtained was $(6 \pm 2) \times 10^{14}$ cm^{-2} at 20 cm distance from the plasma focus anode tip and it close to measured deuterium ion fluence in MEPF-12. The deuterium ion fluence numerically computed using Lee Model Code is also falls in the range of $(2.4 - 7.8) \times 10^{16}$ cm^{-2} for plasma focus devices operating from 0.4 to 486 kJ at their optimum operating conditions. [**Lee et al. 2012]** They derived an expression for ion fluence using first principle calculation and it is expressed as [**Lee et al. 2013**]

$$\text{Ion Fluence}(\text{per m}^2) = 8.5\text{x}10^8 \, I_{\text{pinch}}^2 \, Z_p \left(\frac{\ln \frac{b}{r_p}}{\pi \, r_p^2 \, U^{1/2}} \right) \qquad \textbf{(4.1)}$$

Here, I_{pinch} is current flowing through the pinch, r_p and Z_p are the final pinch radius and length, b is cathode radius, U is the disruption caused voltage which is equal to $3 \times V_{max}$, where V_{max} is the maximum voltage induced by radially collapsing current sheath (All quantities are in SI unit). We run Lee Model Code to obtain various parameters and they are inserted in eq. 4.1 to compute the ion fluence and average ion energy.

Typical MEPF-12 configuration parameters used are: 9.7 kJ: $L_0 = 74$ nH, $C_0 = 40$ μF, b = 5.5 cm, a = 3 cm, $Z_0 = 11.5$ cm, $r_0 = 2$ mΩ operated at 22 kV and P = 3 torr deuterium. Fitted mass and current factors are $f_m = 0.075$; $f_c = 0.7$; $f_{mr} = 0.15$ and $f_{cr} = 0.7$. Typical experimental and simulated current waveforms are shown in fig.4.16. Relevant outputs computed from the code are: $I_{pinch} = 261$ kA; $r_p = 0.43$ cm; $Z_p = 4.4$ cm and $U = 3 \times 38.4$ kV=115.2 kV. The ion fluence is estimated to be 3.3×10^{16} cm^{-2} with average energy of ≈ 115 keV. The computed ion fluence for MEPF-12 device falls in the range i.e. $(2.4 - 7.8) \times 10^{16}$ cm^{-2} for operating energy range from 0.4 to 486 kJ. The difference in experimentally measured and computed values of deuterium ion fluence is due to the

fact that the computed value of ion fluence is of pinch column which will decrease as $1/r^2$ with distance from the pinch column.

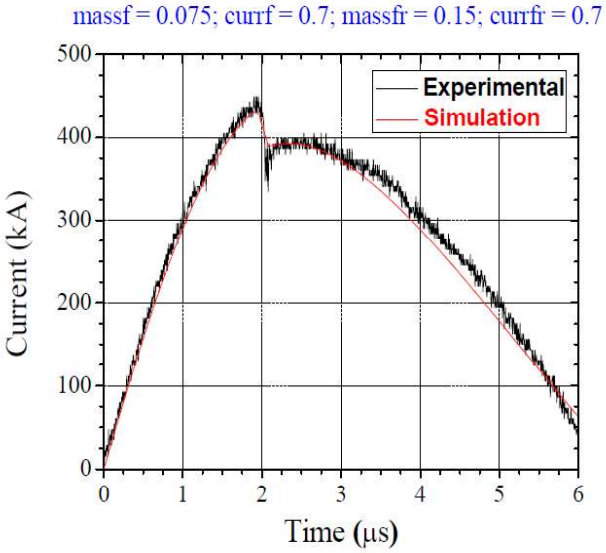

FIG. 4.16 Typical experimental and simulated current waveform from MEPF-12 device.

Angular emission profile of ions is measured using CR39 nuclear track detectors. Three different CR39 detectors are placed at three different angular positions i.e. 0, 30 and 90 deg. at 9 cm from the plasma focus anode tip. The angular positions are w. r. t. plasma focus anode axis. The experimental chamber is filled with hydrogen gas at pressures varying from 1 to 7 mbar. Protons of energies ranging from a few 10s eV to several hundred keV are expected to produce in each plasma focus shot. Proton tracks in two consecutive shots are recorded at each filling pressures to get countable tracks. The exposed CR39 detectors are etched in 6N potassium-hydroxide (KOH) solution at 60 ^{o}C for two hours. The tracks are counted using a Zeiss-microscope. Typical microscope images of proton tracks in CR39 detectors at 30 and 90 deg. are shown in fig. 4.17 (a) and (b). The CR detectors placed along the electrode axis is seen to be overexposed due to high fluence of proton and

therefore it is not possible to count tracks. A typical image of such proton tracks at 0 deg. is presented in fig. 4.18.

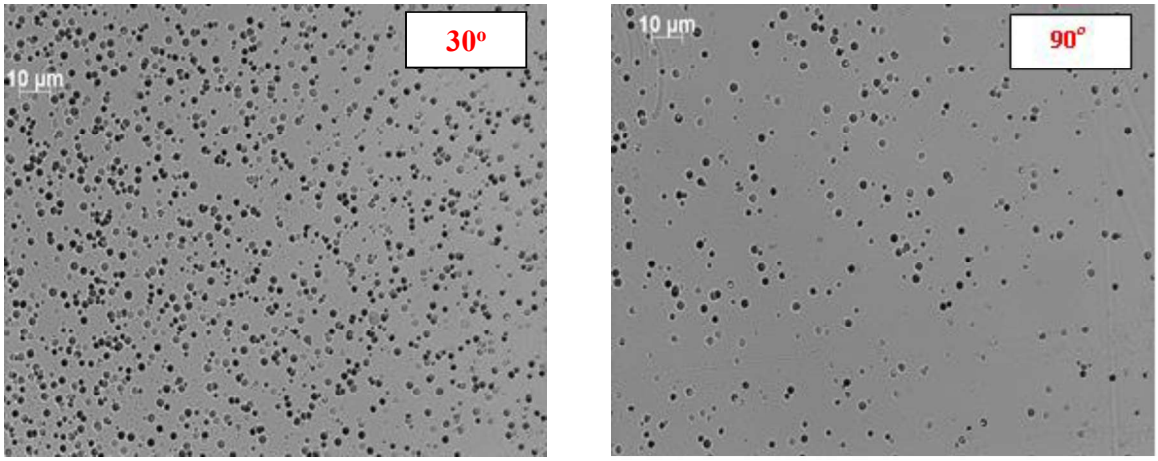

Fig. 4.17 Typical proton tracks in CR39 detector placed at 30 and 90 deg.

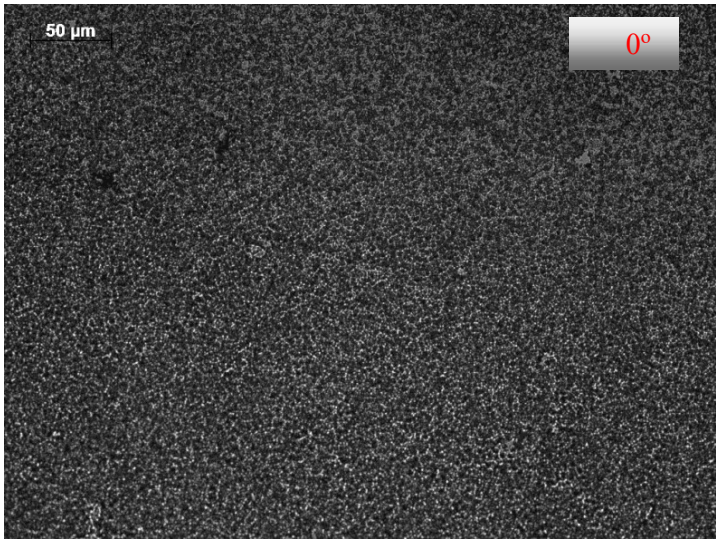

FIG 4.18 Typical microscope image of tracks observed in CR39 detectors placed along the axial direction.

An Al foil of 25 μm thick is used as filter to avoid overexposure of CR39 detectors by protons but in axial direction (0 deg.), it is found to be ruptured after plasma focus shot. The filters at 30 and 90 deg. are found to be intact after shot. The possible reason could be melting and evaporation of filters due to high heat flux produced by the intense and energetic protons along the axis. Therefore, to compare proton fluence at three different angular positions in identical conditions, bare CR39 detectors were used. The proton track densities recorded at 30 deg. and 90 deg. angular positions are considered for estimation of anisotropy factor. The proton track densities are observed to be more at 30 deg. compared to 90 deg. This indicates that the emission of ions is anisotropic i.e. ions accelerated along the axially forward direction is more than in the radial direction in conformity with other reports [Aliaga-Rossel et al. 1998]. For each filling pressure, the anisotropy factor i.e. the ratio of track densities in the 30 deg. to that of in the 90 deg. is calculated. Fig. 4.19 shows the variation of anisotropy factor with filling hydrogen gas pressures. The anisotropy factor is found to be increasing with filling pressure up to 5 mbar and then decrease with further enhancement in filling pressure. The value of anisotropy is estimated to be maximum of 1.43 at 5 mbar and minimum of 1.04 at 1 mbar of hydrogen gas filling pressure.

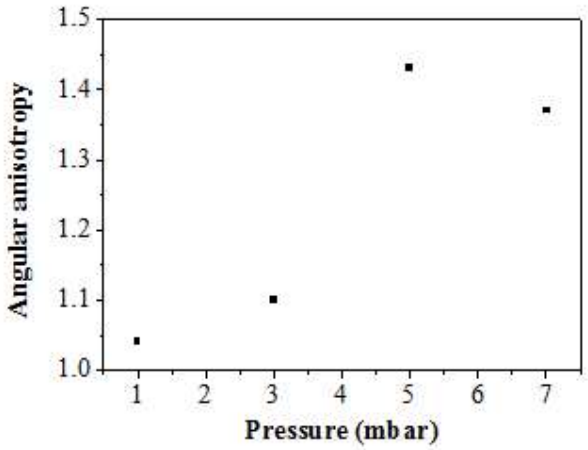

FIG. 4.19 Variation of angular anisotropy of protons in MEPF-12 device.

4.5 Experimental results of MEPF-17 device

The MEPF-17 is characterized as a neutron and ion source for understanding of emission mechanism as well as applications. The plasma focus head of MEPF-17 device can be placed conveniently in any orientation suitable for required applications as well as to study neutron emission characteristics such as anisotropy in neutron yield and its energy.

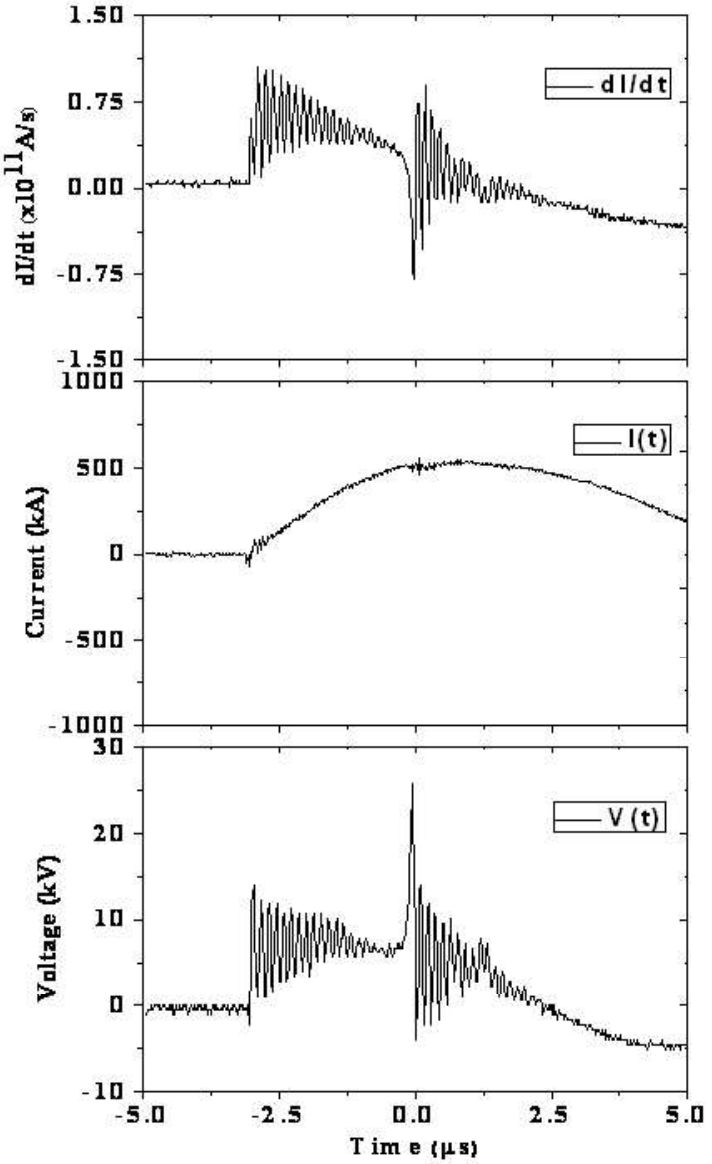

FIG. 4.20 Typical signals of current derivative, current and voltage signals (top to bottom) from MEPF-17 device.

Two silver activation detectors and two PSD detectors are placed in the axial and radial directions simultaneously to measure time integrated neutron yield and time resolved emission of neutrons. Rogowski coil and aqueous copper-sulphate ($CuSO_4$) based voltage divider are used to record current derivative and voltage across plasma focus. The current is obtained by passively integrating the current derivative signal. For experiments, the plasma chamber of MEPF-17 device is evacuated to a vacuum of $\leq 10^{-5}$ mbar before filling deuterium gas to pressures of (1 - 10) mbar and operated at maximum of 17 kJ. The optimum filling pressure is found to be 5 mbar. Typical signals of the current derivative, current and voltage from MEPF-17 device are shown in fig. 4.20. Fig. 4.21 depicts typical signals of time resolved neutrons (along with hard X- rays) and the current-derivative.

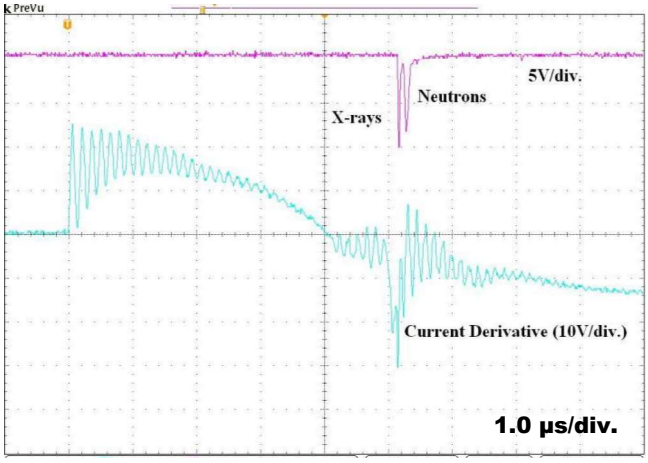

FIG. 4.21 Typical current derivative waveform, neutrons and X-rays signal from MEPF-17 device.

In this particular device, the current – derivative waveform is observed to have oscillatory structures. The reason may be attributed to the impedance mismatch between plasma focus load and coaxial cables (48, each 5 m) used for connecting it to the capacitor bank. The hard X-rays pulse is ascertained by putting 25 mm thick lead brick in front of the PSD detector in a few plasma focus shots. The first pulse is either attenuated or completely cutoff after passing through lead brick. Also, the separation between the two pulses changes by changing the location of PSD detector away from

plasma focus. It is because of different TOFs of hard X-rays pulses and neutron pulses. The TOF method is used to measure neutron energy assuming that hard X-rays and neutrons are produced at the same time [Gribkov et al. 2007].

The neutron yield is measured at each filling pressures in both directions. The variation in the neutron yield in the radial direction with the deuterium gas filling pressure is shown in fig.4.22. The average neutron yield increases to a maximum of $(7.1 \pm 1.4) \times 10^8$ neutrons/shot into 4π Sr at 5 mbar and then starts decreasing with further increase in filling pressure. The average values are obtained from 10 consecutive plasma focus shots.

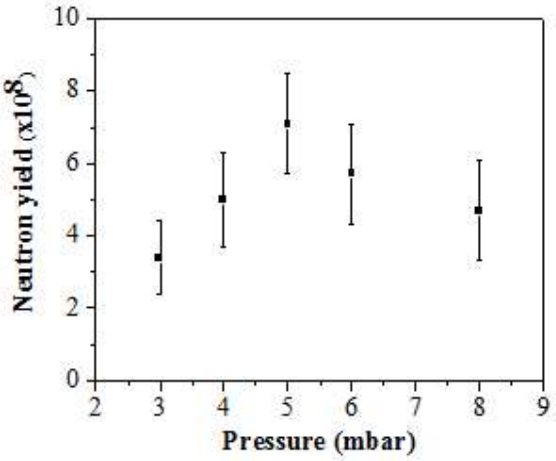

FIG. 4.22 Variation in neutron yield in the radial direction with deuterium gas pressure.

The neutron yield anisotropy Y_0^o/Y_{90}^o i.e. ratio of the neutron yield in the axial direction to that of in the radial direction is evaluated at each filling pressure. It is found to be increasing with increase in filling pressure and a maximum of (1.33 ± 0.18) is observed at 5 mbar. It decreases with further increase in filling pressure as shown in fig. 4.23(a). Also, the neutron energy anisotropy E_0^o/E_{90}^o i.e. ratio of the neutron energy in the axial to that of in the radial directions is estimated using signals recorded in two PSDs kept in the axial and radial directions. Similar to neutron yield, the anisotropy in neutron energy initially increases with increase in filling pressure reaching a maximum

of (1.35 ± 0.09) at 5 mbar, and then decreases with further increase in filling pressure. The variation of neutron energy anisotropy is shown in fig. 4.23(b). The maximum values of neutron energies in the axial and the radial directions are found to be (2.90 ± 0.20) MeV and (2.58 ± 0.20) MeV respectively. As observed in figs. 4.23(a) and (b), the variations in the anisotropies of neutron yield and its energy has similar trends. This is possibly due to change in deuterium ion energy spectrum i.e. deuterium ion number density and its energy in the axial and the radial direction with filling pressures [Roshan et al. 2009, Kelly et al. 1996]. The maximum of anisotropy factors for neutron yield and its energy are observed at 5 mbar which is the optimum pressure at 17 kJ operations. This suggests that deuterium ions have maximum fluence as well as energy at optimum filling pressure for a plasma focus device.

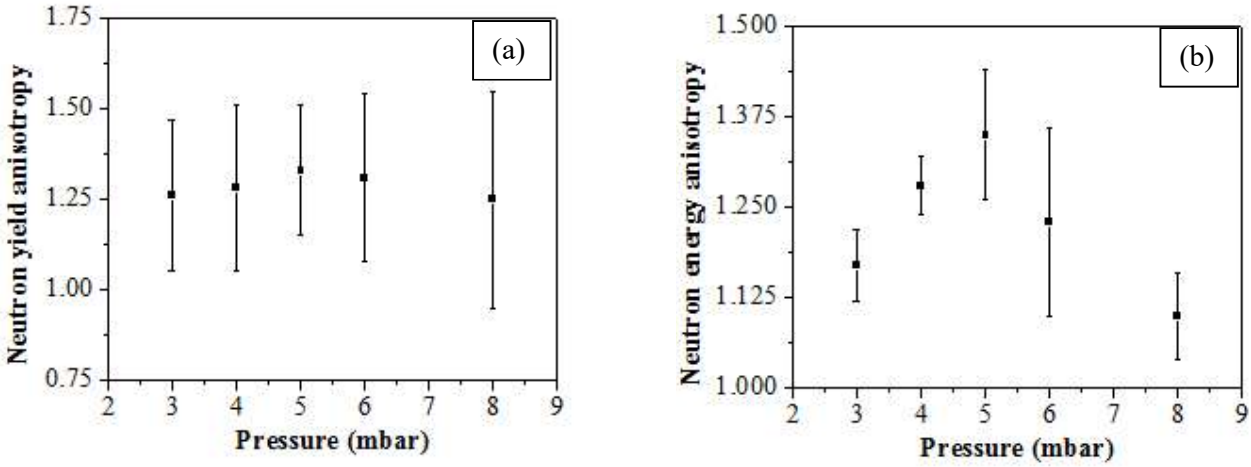

FIG. 4.23 Variations in (a) neutron yield anisotropy and (b) neutron energy anisotropy with filling pressure.

The measurements of time resolved emission of deuterium ions is performed using Faraday cup located at distance of 14 cm from the anode tip. Typical signals of current-derivative and Faraday cup are shown in fig. 4.24. The average ion fluence per pulse is measured to be $(5.1 \pm 0.5) \times 10^{14}$ cm^{-2} at optimum 5 mbar deuterium gas filling pressure. The measured values of peak number density and most probable energy of deuterium ions are $(2.7 \pm 0.7) \times 10^{12}$ cm^{-3} and (180 ± 50) keV respectively at 5 mbar.

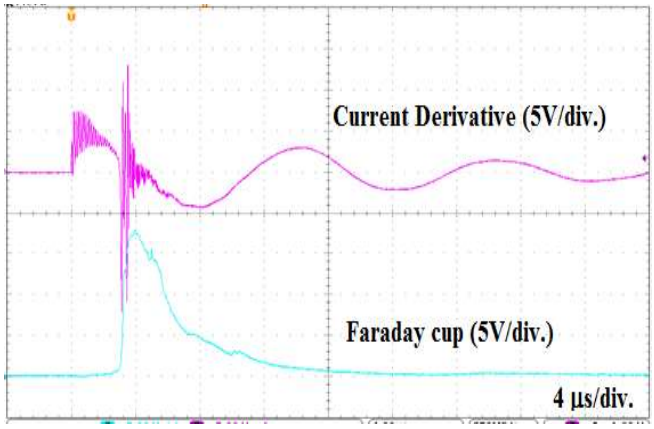

FIG. 4.24 Typical signals of current derivative and ion pulse MEPF-17 device.

4.6 Summary and Conclusions

Miniature sealed tube based plasma focus device, SPF1-P2, operating at 200 J is characterized as portable neutron source for long duration operation without purging deuterium filling gas. Neutron emission in SPF1-P2 device is observed for 200 shots over 200 days without refilling deuterium gas. It has smallest plasma chamber of volume of 33 cm^3 among known miniature devices developed by various research groups across the world. The neutron emission is observed to be deteriorating in each shot. The possible reason of neutron yield deterioration is impurities due to electrode material erosion and accumulation of hydrogen and ^3He ashes (nuclear fusion products). In repetitive PF-P5 device, enhancement in time averaged neutron yield has been achieved by repetitively operating at 10 Hz. Time resolved measurements of neutrons revealed that neutron emission varies from one pulse to other but total neutron yield multiplies to a factor approximately equal to the number of pulses. The pulse to pulse variation in neutron emission may be attributed to impurities and variation in leakage current that flows through insulator backwall.

Three different plasma focus devices, PF-2, MEPF-12 and MEPF-17 are characterized for radiation emission mechanism and their correlation to different parameters. A compact PF-2 is

characterized as a pulse ion source. MEPF -12 is characterized as neutron and ion source. It is found that the measured neutron yield of (1.2 ± 0.3) × 10^9 neutrons/pulse with pulse width of (46 ± 5) ns. The neutron energy estimated from the time of flight is (2.45 ± 0.20) MeV in the radial direction. The variation in neutron energy is due to deuterium ions of wide energy range that participate in nuclear fusion process. The measurement of time resolved emission of ions suggests that peak ion density and average energy of ions change with changing operation parameters (filling pressure and operation energy) but ion fluence remains nearly independent of each of them. The present study finds that it is velocity distribution of deuterium ions that changes with operation parameters but not the total deuterium ions. Study of spatial profiles of ion using CR39 track detector confirms anisotropic emission of ions with more energy and fluence in the axial direction than in the radial direction of plasma focus.

In MEPF-17, the neutron yield measured in the radial direction is (7.1 ± 1.4) × 10^8 neutrons/shot into 4π Sr at 5 mbar. The maximum values of neutron energies in the radial direction is estimated to be (2.58 ± 0.20) MeV respectively. Anisotropies in neutron yield and their energy are measured in MEPF-17 device. The anisotropy factors vary with filling pressures and it follows similar trend for neutron yield and its energy. The maximum values are obtained as (1.33 ± 0.18) and (1.35 ± 0.09) for neutron yield and neutron energy respectively at 5mbar. The reason of anisotropy may be attributed to beam-target fusion mechanism of neutron emission in conformity with other reports.

References:

1. "Experimental observations of the spatial anisotropy of the neutron emission in a medium energy plasma focus", Aliaga-Rossel and R. and Choi P., *IEEE Trans. Plasma Sci.,* **1998**, *26*, 1138-1145.
2. "Neutron Correlations with Electrical Measurements in a Plasma Focus Device", Bruzzone H., Acuna H, Clausse A., *Brazilian J. Phys.*, **2008**, *38(1)*, 117-122.

3. "A high-neutron-output dense plasma focus", Burns E.J.T., Falacy S.M., Hill R.A. et al., *Phys. Lett. A,* **1988**, *133*, 144-148.
4. "Pinch formation and reaction proton spectra of SPEED 1 focus discharges", Calker C. V., Decker G., Jager U. et al., *Phys. Lett. A,* **1985**, *113A*, 203-206.
5. "Ion acceleration in a plasma focus", Gary S. P., *Phys. Fluids,* **1974**, *17*, 2135.
6. "Low energy repetitive miniature plasma focus device as high deposition rate facility for synthesis of DLC thin films", Ghareshabani E., Rawat R.S., Verma R. et al., *Appl. Surf. Sci.,* **2010**, *256*, 4977–4983.
7. "Plasma dynamics in the PF-1000 device under full-scale energy storage: II. Fast electron and ion characteristics versus neutron emission parameters and gun optimization perspectives", Gribkov V. A., Banaszak A., Bienkowska B. et al., *J. Phys. D: Appl. Phys.,* **2007**, *40*, 3592–3607.
8. "Ion-beam and neutron production in a low-energy plasma focus", Kelly H. and Marquez A., *Plasma Phys. Control. Fusion,* **1996**, *38*, 1931–1942.
9. "Analysis of the Nitrogen Ion Beam Generated in a Low-Energy Plasma Focus Device by a Faraday Cup Operating in the Secondary Electron Emission Mode", Kelly H., Lepone A., M´arquez A., *IEEE Trans. Plasma Sci.,* **1998**, *26 (1)*, 113 – 117.
10. "Numerical experiments providing new insights into plasma focus fusion devices", Lee S. and Saw S. H., *Energies,* **2010**, *3*, 711-737.
11. "Plasma focus ion beam fluence and flux-scaling with stored energy", Lee S., and Saw S. H., *Phys. Plasmas,* **2012**, *19*, 112703(1-5).
12. "Plasma focus ion beam fluence and flux-for various gases", Lee S. and Saw S. H., *Phys. Plasmas,* **2013**, *20*, 062702(1-10).

13. “Surface and bulk processes in materials induced by pulsed ion and plasma beams at Dense Plasma Focus devices”, Pimenov V. N., Maslyaev S. A., Ivanov L. I. et al., *Nukleonika,* **2006**, *51(1)*, 71−78

14. “Note: A Portable pulsed neutron source based on the smallest sealed-type plasma focus device”, Niranjan R., Rout R. K., Mishra P. et al., *Rev. Sci. Instrum.,* **2011**, *82*, 026104.

15. “The smallest plasma accelerator device as a radiation safe repetitive pulsed neutron source”, Niranjan R., Rout R. K., Srivastava R. et al., *Indian J. Pure Appl. Phys.,* **2012**, *50*, 785.

16. “A 10^9 neutrons/pulse transportable pulsed D-D neutron source based on flexible head plasma focus unit”, Niranjan R. , Rout R. K. , Srivastava R. et al., *Rev. Sci. Instrum.,* **2016**, *87*, 033504.

17. “Neutron and high energy deuteron anisotropy investigations in plasma focus device”, Roshan M. V., Rawat R. S., Talebitaher A. et al., *Phys. Plasmas,* **2009**, *16*, 053301.

18. “Effect of anode and insulator materials on plasma focus sheath (pinch) current”, Shyam A. and Rout R. K., *IEEE Trans. Plasma Sci.,* **1997**, *25*, 1166-1168.

19. “Statistical characterization of the reproducibility of neutron emission of small plasma focus devices,” Tarifeno-Saldiviaa A., Soto L., *Phys. Plasmas,* **2012**, *19*, 092512 (1-10).

Chapter-5

Material Science Investigations using Plasma Focus

5.0 Introduction

The plasma focus devices, as an ion and plasma source, have been used for irradiation on materials. They have also been used for deposition of thin films. The neutrons are used for non-destructive assaying of materials, and short-lived radioisotope productions. Different investigations in material sciences are described in following sections.

5.1 Ion irradiation and surface damage study of fusion relevant materials

The major challenge in realization of fusion power is selection of materials for various components of thermonuclear fusion reactor. The thermonuclear fusion reactor such as ITER has many components (structural and functional) namely first wall, blanket, diverter, vacuum vessel, cryostat with superconducting magnets, and various support structures [Barabash et al. 2007]. They will be exposed to heat loads (steady and transient) in form of energetic ions and electromagnetic radiations [Brooks et al. 2009, Hirai et al. 2005, Renk et al. 2005]. Steady state heat load of 5 to 20 MW/m^2 for the diverter and 0.5 MW/m^2 for the first wall are estimated during ITER operations. Transient heat load, such as plasma disruptions is estimated to deposit energy densities of several ten MJ/m^2 for durations of the order of 1ms on the diverter. Other transient events namely type-I edge localized modes (ELMs) and vertical displacement events (VDEs)are expected to deposit large energy density in short time typically of sub-ms to a few hundred ms [Hirai et al. 2005]. In addition to heat flux, exposure to energetic (14.1 MeV) neutrons is expected to change structural properties of the wall materials through displacement damage and nuclear transmutations. The neutron flux at the first wall of ITER is estimated to be the order of $\sim 10^{17}\ m^{-2}s^{-1}$ [Hirai et al. 2005]. As a consequence, there are stringent requirements regarding the properties of plasma facing materials (PFM) of fusion reactor

such as high thermal conductivity, good thermo-mechanical properties, low activation by neutrons, resistance to radiation damage, low retention of fusion fuels among others. Thus, it is essential to understand materials behavior under conditions similar to that in fusion reactors which will help in selection of materials from existing materials and also in developing new materials as well as predicting their behavior in fusion reactor environment.

For experimental simulations of materials behavior under the fusion reactor relevant heat flux, different heat sources e.g. electron beam, ion beam, IR, plasma guns, and high power lasers, have been applied. An accelerator-driven intense neutron source, International Fusion Material Irradiation Facility (IFMIF), is being designed for simulation of effects of 14.1 MeV neutrons on materials. The neutron emission rate of typically 10^{17} $n.s^{-1}$ is estimated in IFMIF, which would result in a flux of some 10^{14} $n.cm^{-2}.s^{-1}$ at the reactor first wall. Therefore, displacement damage and transmutation in the irradiated material would match the neutron-induced effects anticipated in the fusion reactor environment. Each of the above facilities is used to see effects due to particular radiation only and they do not provide manifestation of fusion reactor environment.

The plasma focus device is proven to be an excellent simulator for materials behavior under fusion relevant conditions. This provides a fusion reactor environment for several tens ns with all sort of radiations including X-rays, ions, electrons and neutrons. Using plasma focus device, it is possible to attain heat flux required for fusion research with a relatively compact and at a cost lesser than other experimental facilities. Energetic ions with the average energy of ~ 100 keV and plasma jet of temperature ~ 0.1–1.0 keV as well as of extremely high power density (up to P ~ 10^{12} W/cm^2) are generated [Pimenov et al. 2008]. It has been reported that a combined interaction of energetic ions, plasma jet and electro-magnetic radiation in a wide range of power density: 10^7 to 10^{12} W/cm^2 with the target materials produce significant changes in materials properties [Pimenov et al. 2002]. Another advantage is high neutron yield with right energy spectra. Also, though repetitive operations at high

repetition rate, high neutron flux required for fusion research can be attained with relatively small size device at low cost.

Bostick et al. [1976] used plasma focus devices for irradiation of deuterium ions on the plates of polycrystalline Al, Cu and single crystal Si for the first time. They used two plasma focus devices in 5 to 10 kJ range to expose samples to the pulsed deuteron beams. They presented the preliminary results on radiation damage (blistering and pitting) in the metal (Al, Cu) and Si plates.

Pimenov et al. [2008] used different plasma focus devices for irradiating plasma facing materials (W and stainless steel) by high power density pulses of ion beam and plasma streams. They used PF-1000, PF-6 and PF-5M devices with the hydrogen and/or deuterium as the filling gas. They have studied the influence of high power density ions and plasma streams upon surface damage, evolution of microstructure and subsequent properties of the materials.

Bhuyan et al. [2013] used 2.2 kJ plasma focus device for irradiation of protons on the tungsten plates using multiple shots (5, 10 and 20 shots). They observed various damage features such as micro-cracks (w-type and r-type cavitation) on the tungsten surface after irradiations. Dutta et al. [2014] used 2.2 kJ plasma focus device to study the helium ion induced changes in the tungsten material. They have exposed polycrystalline tungsten sample using multiple shots (5 and 10) and studied their surface damage characteristics.

In present work, five different materials viz tungsten (W), nickel (Ni), stainless steel (SS), molybdenum (Mo) and copper (Cu) are chosen to study their surface damage characteristics under pulse ion irradiation using a medium energy plasma focus device. These materials and/or their alloys have been considered as candidate materials for many of the components of ITER and other fusion devices [Barabash et al. 2007, Brooks et al. 2009]. Tungsten has been considered as the first wall materials and ferritic-martensitic steel has been selected as the main structural material for the ITER vacuum vessel and in vessel components. Molybdenum has been used for the first wall materials in the Alcator C-Mod TOKAMAK [Hutchinson et al. 1994]. Copper is proposed to be used as clad in

vacuum vessel while copper alloy e.g. CuCrZr is proposed to be used in ITER first wall and diverter applications. The Ni alloy e.g. NiAl bronze has been selected for vacuum vessel and blanket support in ITER. Moreover, comparative analysis of surface damages on materials having different physical, thermal and mechanical properties exposed to same power flux density will prove to be useful in understanding the interaction of fusion grade plasma with material. Different properties of interest for the material investigated here are described in table 5.1.

Table 5.1 Various properties of materials.

Materials	Crystal Structure	Melting point (K)	Thermal Conductivity (W/(m·K))	Elastic Constant (GPa)
W	BCC	3695	173	411
Mo	BCC	2896	138	329
SS	Duplex (FCC and BCC)	1658-1716	19	193
Ni	FCC	1728	90.9	200
Cu	FCC	1358	401	120

5.1.1 Experimental procedures

The samples of materials are cut into discs of 2 mm thickness and 10 mm in diameter. The samples are polished to reduce surface roughness (R_a) to a few μm and are rinsed ultrasonically in alcohol to remove dust particles before irradiations. The sample is mounted at 6 cm from the anode tip along the axial direction in the plasma chamber. Initially it is at room temperature. A schematic of experimental set up is presented in fig. 5.1. The plasma chamber is evacuated to a base pressure of $\leq 10^{-5}$ mbar using a rotary-diffstac pump. A shutter is placed before sample. It is used to prevent the samples from exposure of thermal plasma in initial insulator conditioning shots. During these shots (5 - 6 shots), either no focus or mild focus is observed. Once strong focus is observed, the shutter is removed without breaking the vacuum in experimental chamber. The MEPF-12 device is operated

with optimum deuterium gas filling pressure of 4 mbar at capacitor bank energy of 11.5 kJ. Each sample is exposed to twenty plasma focus discharges at a gap of minimum 30 minutes. In each plasma focus discharge, the deuterium ion and neutron fluence at sample position are measured to be ~ 10^{14} ions/cm^2 and ~ 10^6 neutron/cm^2 respectively. The energies of deuterium ions are estimated to be in the range of 100s of eV to 100s of keV at sample position. Along with the pulsed energetic deuterium ions and neutrons, dense plasma jet of velocity ~10^7 cm/s and shock wave fronts are reported to be formed in the plasma focus discharge [Pimenov et al. 2008].

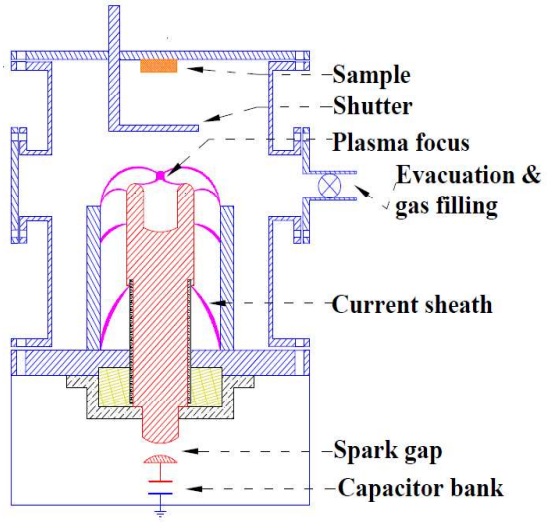

FIG.5.1 Schematic of ion irradiation setup.

5.1.2 Analysis of irradiated samples

Irradiated samples along with virgin samples of all the materials are characterized using various experimental techniques namely SEM, surface profilometer, XRD and EDX. Surface damage features e.g. surface morphology, surface roughness, crystallinity and elemental compositions of all samples after and before irradiations are analyzed and a comparative analysis is presented here.

5.1.2.1 SEM characterizations

The SEM micrographs of the irradiated surfaces indicate multifold melting, recrystallization and various surface defects such as blisters, pores, craters and cracks whereas the virgin surface is smooth and only a few traces of mechanical treatment during polishing are observed. The SEM micrographs of the W surface before and after irradiations are shown in fig.5.2(a) and figs.5.2(b) to (d) respectively. It is seen erosions due to evaporation and sputtering of the surface layer. The formations of the cracks, blisters of different shape and size over the entire W surface are visible.

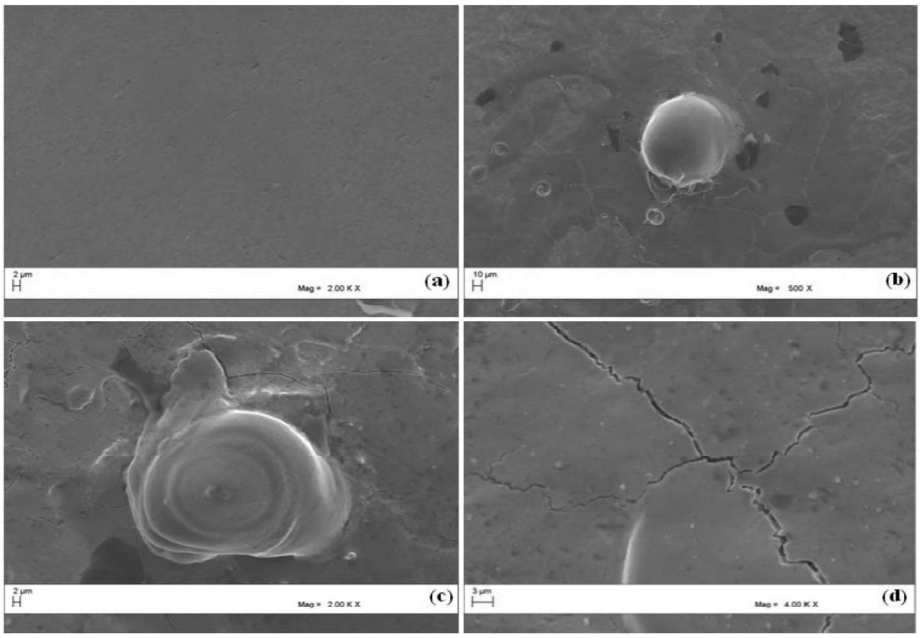

FIG. 5.2 SEM micrographs of the surface of tungsten sample (a) before and (b), (c) and (d) after exposed to 20 PF discharges.

Figs. 5.3 to 5.6 display the surface morphologies of Ni, SS, Mo and Cu respectively before and after exposure to twenty shots. The irradiated surfaces of W, Mo and Ni samples have cracks all over as evident from the micrographs. The micrographs reveal that the cracks propagate along and penetrate the surfaces of the samples. The cracks in the W and Mo propagate along the surface up to lengths varying from tens to hundreds of micrometers. They are connected to each other in the shapes

like x- and w-type cavitation whereas the cracks on the Ni sample are isolated from each other. They mostly propagate unidirectionally along the surface like r-type cavitation. The lengths of the cracks in the Ni sample are in the range of a few to tens of micrometers. The widths of the cracks are in the range of 0.1 - 1.1 μm, 0.1 - 1.4 μm and 0.3 - 2.7 μm in W, Mo and Ni respectively. Similar patterns of the cracks are reported to be observed in the W when irradiated with deuterium ion [Bhuyan et al. 2013], and with helium ion [Dutta et al. 2014] in the plasma focus device. These materials indicate "brittle fracture" tendencies under pulse irradiations.

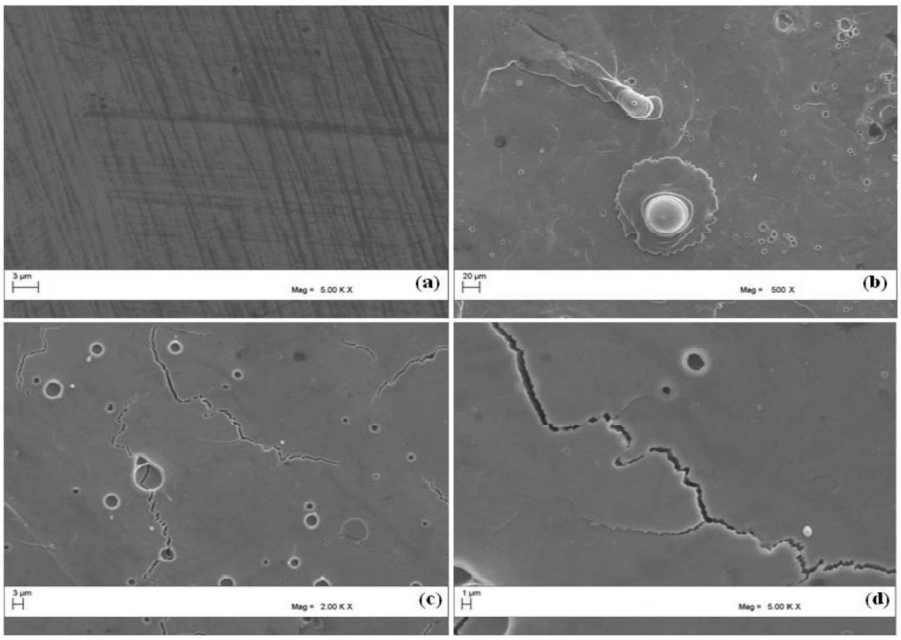

FIG.5.3 SEM micrographs of the surface of nickel sample (a) before and (b), (c) and (d) after exposed to 20 PF discharges.

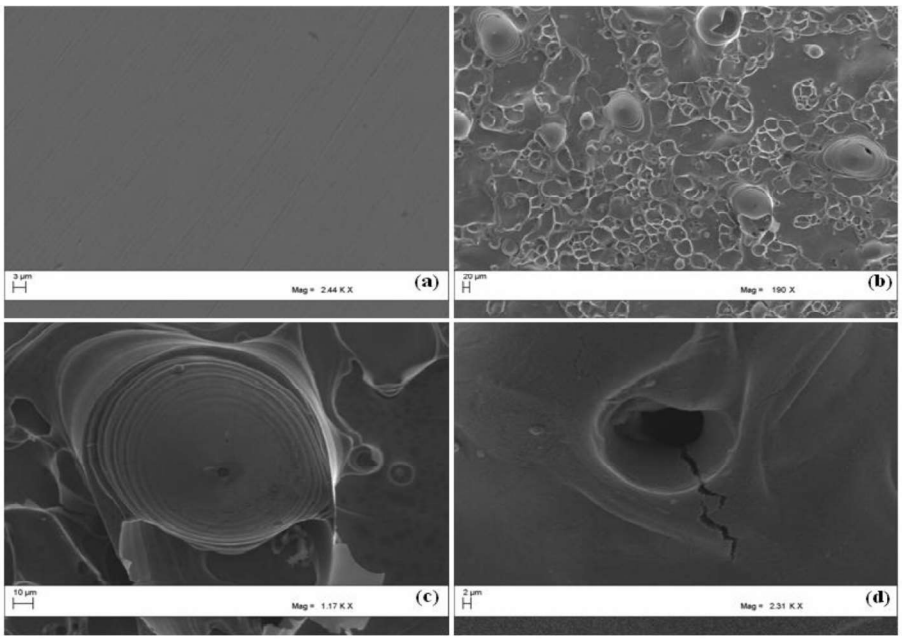

FIG. 5.4 SEM micrographs of the surface of stainless steel (a) before and (b), (c) and (d) after exposed to 20 PF discharges.

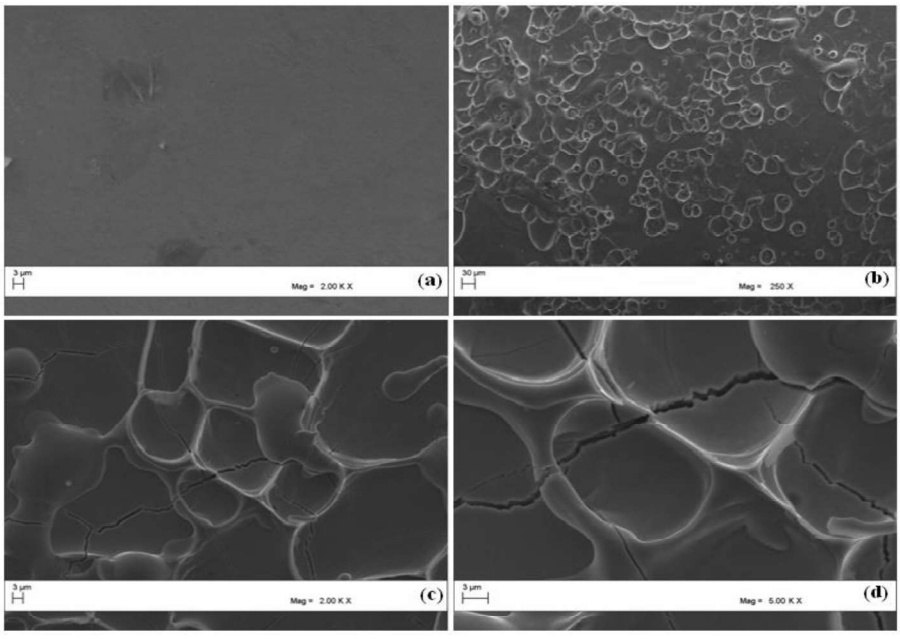

FIG. 5.5 SEM micrographs of the surface of molybdenum (a) before and (b), (c) and (d) after exposed to 20 PF discharges.

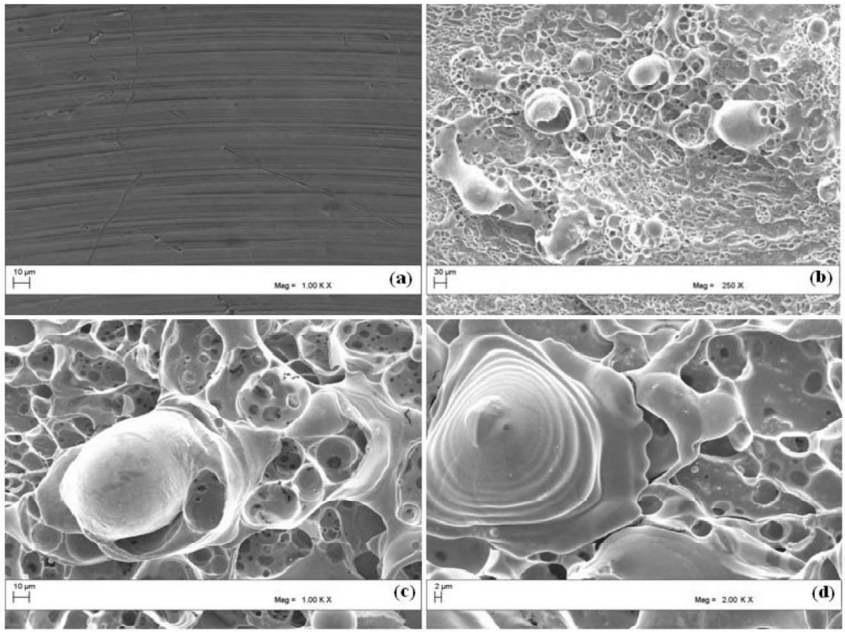

FIG. 5.6. SEM micrographs of the surface of copper sample (a) before and (b), (c) and (d) after exposed to 20 PF discharges.

The micrograph [fig.5.4(d)] of the irradiated SS surface show a few micro-cracks of 25 - 30 µm lengths and of widths in the range of 0.7 - 1.4 µm. The irradiated copper surface has no cracks as shown in SEM micrographs [fig.5.6(b) to (d)]. The Copper being a ductile material and having low melting point (1358 K) and low threshold for sputtering (36 eV), has more melting and erosion. Moreover, the melted surface layer due to ion beam irradiation may get splashed by the high-speed plasma jets. This results in craters formation rather than the microcracks. The variation in dimension and shape of the cracks are possibly due to variation in the thermal stress developed on different materials under exposure to multiple pulsed deuterium plasma streams [Pimenov et al. 2002].

The surface temperature profile and thermal evolution of the samples are of transient (a few hundred ns) and to a depth of a few micrometers as the range of 100 keV deuterium ion is typically a few microns in different samples [SRIM- 2008]. The measurements of surface temperature profile of sample under irradiation require diagnostics having time resolution of a few ns and depth resolution of 100s of nm which is technologically not viable to achieve simultaneously. Therefore, thermal evolution of the samples is mainly used to studied theoretically.

Sanchez et al. numerically estimated surface temperature profile of SS, Cu and Ti under irradiation of pulsed nitrogen and argon ion beam in plasma focus device **[Sanchez et al. 1997].** They used one dimensional heat equation for estimation of temperature using finite difference method:

$$\frac{\partial^2 T}{\partial x^2} + \frac{\dot{\varphi}}{k} = \frac{1}{\alpha}\frac{\partial T}{\partial t} \qquad \textbf{(5.1)}$$

here T is the temperature, $\dot{\varphi}$ the energy flux, x denotes the variable depth in the target, t is the time, k the thermal conductivity and α the thermal diffusivity of the material given by

$$\alpha = \frac{k}{\rho c_p} \qquad \textbf{(5.2)}$$

where ρ is the density and c_p is the specific heat of the material.

For calculation, the energy transfer from the ion beam to the target is considered as an energy flux. It is assumed for simplicity that the whole kinetic energy of the ions is transformed into thermal energy of the target and there is negligible loss due to radiation and convection. The calculation showed that fast heating of the surface layer of target material under strong temperature gradients (~10 $K.ns^{-1}$ and ~700 $K.\mu m^{-1}$ respectively for SS under nitrogen ion irradiation) takes place and peak temperatures sometime reach high enough for melting and even vaporization of thin surface layers. This strong heating process has a depth of several micrometers into the material, and it is followed by a fast cooling down (through a thermal conduction process to the sample bulk) which leads to its thermal relaxation within a few microseconds.

The blisters/bubbles are observed in the SEM micrographs of irradiated surfaces of W, Ni, SS and Cu. The diameters of the blisters are in the range of 30 - 70 μm, 3 - 24 μm, 7 - 80 μm and 25 - 100 μm on the surfaces of W, Ni, SS and Cu respectively. These blisters/bubbles are formed due to accumulation of deuterium atoms around the crystalline defects such as vacancies, interstitials, and lattice dislocations, under pulsed irradiation of energetic deuterium ions [Evans et al.1978, Yoshida et

al. 2005, Shu et al. 2009]. Moreover, thermal evolutions of the crystalline defects e.g. thermal densities of vacancies/interstitials, vacancies coalescence, thermal migration of interstitials, deuterium atom diffusion rate etc are controlled by temperature. The temperature of surface layer of sample increases up to a few thousand degrees centigrade under the action of pulsed deuterium ions and plasma streams. It mainly depends on radiation power flux density and samples properties namely density, specific heat and thermal conductivity [Sanchez et al. 1997, Krivobokov et al 2013, Carslaw et al. 2001]. The thermal evolution of various crystalline defects under the enhanced sample temperature is different for different samples which results into the formation of blisters of different sizes under exposure to the same irradiation conditions. These blisters increase the integrated lateral stress in the surface layer which causes the formation of cracks as interpreted from the inter bubble fracture model proposed by Evans et al. [1978]. According to this model, the bubbles grow and coalesce which creates a local stress sufficient to form surface micro-cracks. The evolution of various features e.g. blisters, cracks on Ni under the increasing radiation power flux density are studied and reported [Niranjan et al. 2013].

The surface defects such as open bubbles, craters are observed in the SEM micrographs of the Ni, SS and Cu [figs.5.3(c), 5.4(d) and 5.6(c)]. These surface defects are formed possibly because of blisters explosion. Figs. 5.4(d) and 5.6(d)reveal that the craters of typically 10 μm diameter and of 7 to 100 μm diameters are formed on the surfaces of the SS and the Cu respectively after irradiation. The SEM micrographs of SS, Mo and Cu reveal splashing and motion of melted surface layer due to momentum transferred by energetic ions and dense plasma streams as seen in figs.5.4(b), 5.5(b) and 5.6(b) respectively. The irradiated surface of the Mo has no other surface defects such as blisters, pores, and craters but only has micro cracks of different shapes [figs.5.5(b) to (d)]. The possible reason may be that the surface defects are formed on exposure and are removed thereafter due to the erosion on exposures to successive pulses. Pimenov et al. [2002] have similar observations on

surfaces of pure vanadium after exposure to powerful hydrogen plasma jets and fast hydrogen ion beams in the PF-1000 plasma focus device.

The Cu has surface damage deep down to depths of tens to hundreds of micrometers into the sample. This is possibly due to high thermal conductivity (401 W/mK), low melting temperature (1358 K) and boiling temperature (2835 K) of Cu. The rise in the surface temperature of the Cu by multiple irradiations and increased heat transfer from the surface to the bulk due to high thermal conductivity leads to erosion and defects formation more deep into the sample.

5.1.2.2 Surface profilometry analysis

The surface profilometer measurements have been carried out in all the samples under investigation. It is revealed that the average surface roughness (R_a) values of the irradiated surfaces of different samples increase after exposures to twenty shots. The profilometer scanned over 7 mm length of the samples show many sharp ridges on the irradiated surfaces. The surface defects such as blisters, pores, craters, and cracks as well as the erosion due to evaporation and sputtering of materials, resulted into high roughness of the irradiated surfaces. Figs.5.7(a) and (b) present the surface roughness profiles of W before and after irradiations respectively.

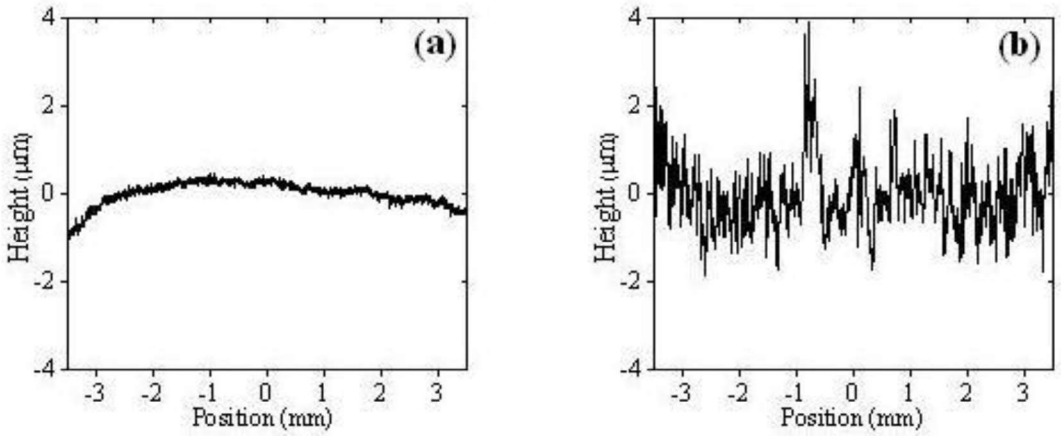

FIG. 5.7 Roughness profile of tungsten sample (a) before and (b) after exposed to 20 PF discharges.

The R_a value of W has increased by threefold (0.2 to 0.6 μm) after irradiations. The R_a values are measured within error of ± 2%. The maximum peak to peak roughness of the W before and after irradiation were 1.7 μm and 5.7 μm respectively. Figs. 5.8, 5.9, 5.10 and 5.11 show surface roughness profiles of the Ni, SS, Mo and Cu respectively. The high R_a value (~ 4.0 μm) of virgin Ni surface is because of mechanical treatment during polishing and it remains unchanged.

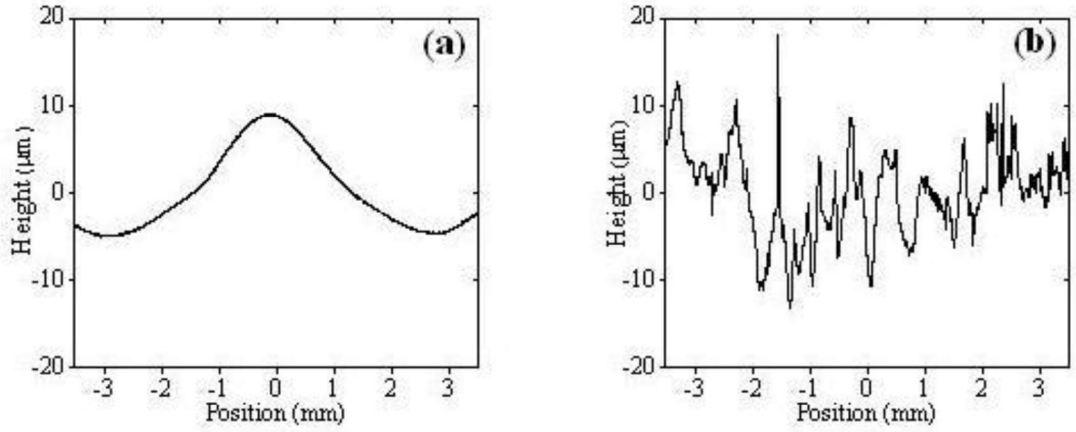

FIG.5.8 Surface roughness profile of nickel sample (a) before and (b) after exposed to 20 PF discharges.

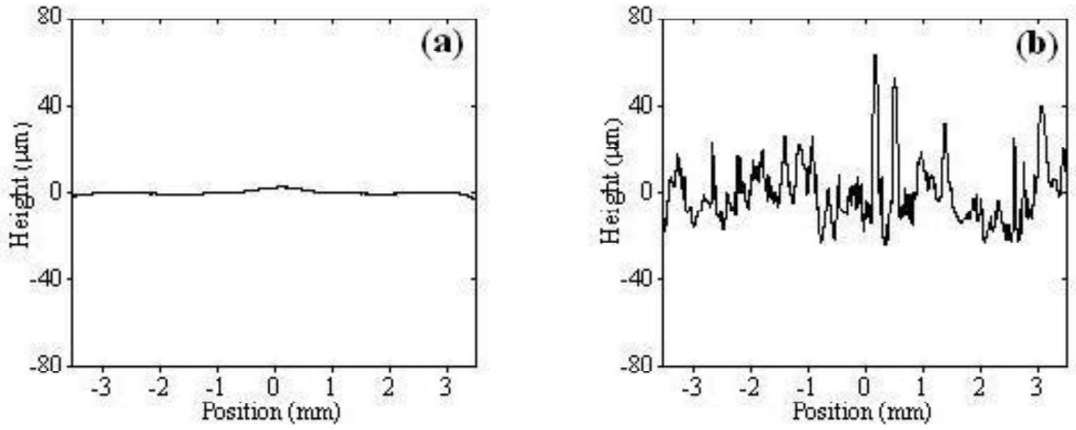

FIG. 5.9 Surface roughness profile of stainless steel sample (a) before and (b) after exposed to 20 PF discharges.

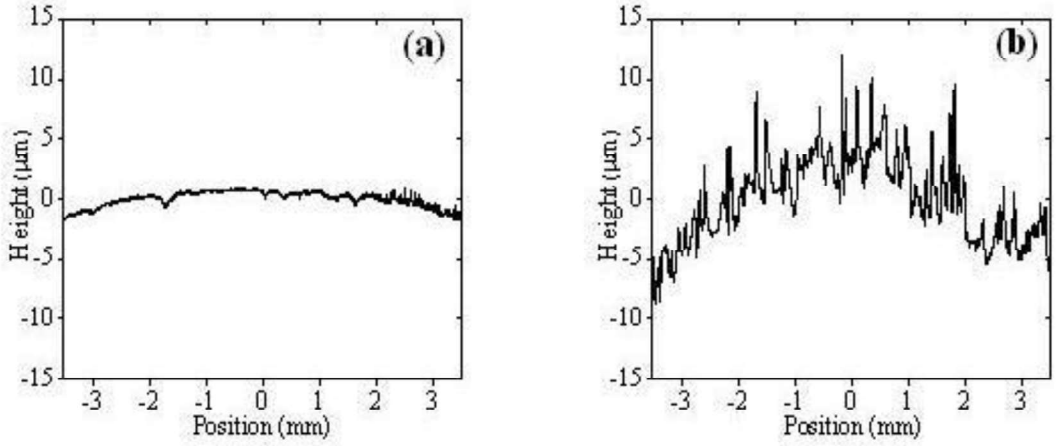

FIG. 5.10 Surface roughness profile of molybdenum sample (a) before and (b) after exposed to 20 PF discharges.

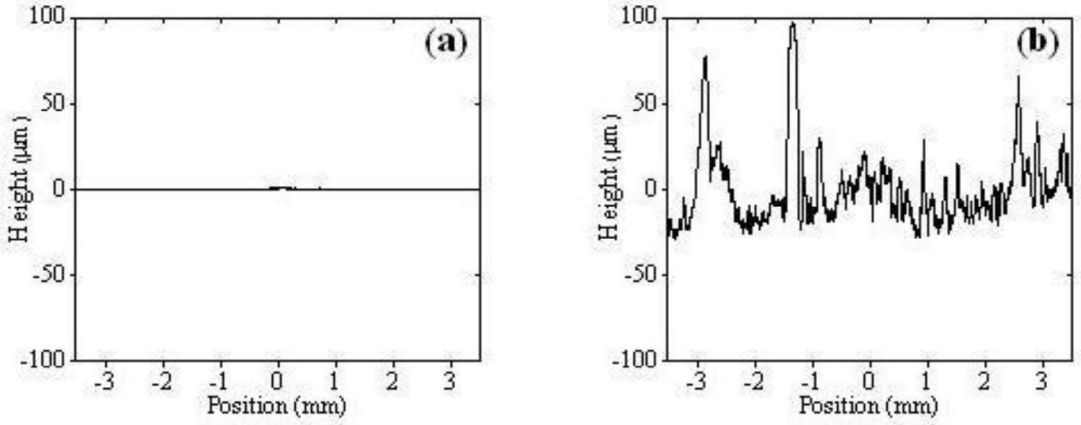

FIG. 5.11 Surface roughness profile of copper sample (a) before and (b) after exposed to 20 PF discharges.

The R_a values of SS, Mo and Cu have increased by eighteen-fold (0.6 to 10.8 μm), six-fold (0.5 to 2.9 μm) and eighty-six-fold (0.18 to 15.5 μm) after irradiations. The maximum peak to peak roughnesses of Ni, SS, Mo and Cu are increased from 14.0 to 31.5 μm, 5.2 to 87.1 μm, 2.9 to 20.7 μm and 1.4 to 125.8 μm respectively. The surface roughness profiles of W and Mo suggest increase in the roughness mainly due to the micro cracks and erosion as seen in figs. 5.7(b) and 5.10(b). Fig. 5.8(b) shows that the crest of the wavy surface in virgin Ni is eroded after multifold melting, evaporations and sputtering. A large number of ridges and grooves are observed in the roughness profile of the irradiated Ni due to formation of blisters, pores and cracks of different dimensions. The high R_a values of irradiated SS and Cu surfaces as observed in figs.5.9(b) and 5.11(b) are due to the blisters and craters of different sizes formed on the surfaces and high erosion due to splashing of the melted surface layer. These observed differences in the surface roughness of different samples may be attributed to difference in erosions due to the evaporation and the sputtering and surface defects characteristics. For light ions incident on heavy materials, sputtering yield is determined by the threshold energy (E_{th}) transferred to the target atoms.

The energy, E_{th}, can be approximated by [Federici et al. 2001]

$$E_{th} = \frac{(M_1+M_2)^4}{4M_1M_2(M_1-M_2)^2} E_s \qquad \textbf{(5.3)}$$

Here M_1 and M_2 are the incident particle mass and target mass, respectively, and E_s is the surface binding energy. Among all the materials (W, Ni, SS, Mo and Cu), the threshold energy [SRIM- 2008, Federici et al. 2001] of deuterium ions needed for physical sputtering is minimum

(36eV) for Cu and is maximum (212eV) for W. The threshold energy of deuterium ion beam required for sputtering of different materials has been tabulated (table 5.2)

Table 5.2 Threshold energy of deuterium ion beam for sputtering of materials.

Material	W	Mo	Ni	Cu
E_{th}(eV)	212	92	39	36

The sputtering of the materials depends on the surface binding energy, surface morphology, incident ion mass, energy and angle of incidence of ions [Makeev et al. 2004]. Moreover, the enhancement of sputtering yield due to the increased surface roughness and the surface temperature rise [Mcckacken et al. 1975, Makeev et al. 2004] after successive exposures to plasma focus discharges leads to variation in the erosion and the roughness of different samples. The extent of surface damage depends on radiation power flux density and the materials physical (density, atomic mass, surface binding energy, and lattice displacement energy), thermal (melting and boiling point, specific heat, and thermal conductivity) and mechanical (elastic constant, and hardness) properties.

5.1.2.3 X-ray Diffraction analysis

The X-ray diffraction analysis of the irradiated samples suggests formation of various microstructures and structural phase transformation due to the thermal stress and the crystal defects (vacancies, interstitials, and lattice dislocations) [Ivanov et al. 2000, Pimenov et al. 2002, Pimenov et al. 2008, Singh et al 2008, Feugeas et al. 1988, Morozov et al. 2015]. The structural phases of W, Ni, Mo and Cu remain unchanged. But an increase in the volume ratio of austenite (γ) to ferrite (α) phases of the SS is observed after multiple irradiations. The diffraction peaks have asymmetrically broadened and peak intensities have changed on irradiations. The 2θ angular positions of the diffraction peaks shift towards higher 2θ angle due to the thermal stress. The residual stress on the irradiated samples is

estimated using angular shifts in diffraction peaks [Singh et al. 2008]. The changes in d-values of the crystal reflection planes corresponding to shifts in 2θ of the diffraction peaks are calculated using Bragg's equation

$$2d\sin\theta = n\lambda. \quad \textbf{(5.4)}$$

From this relation, the strain produced in the crystalline reflection planes of different samples is given as

$$\frac{\Delta d}{d} = \frac{d_{Final} - d_{Initial}}{d_{Initial}} \quad \textbf{(5.5)}$$

The residual stress can be estimated by multiplication of the elastic constant of material with the strain produced on the samples after irradiations. The XRD profiles of the W before and after irradiations are shown in figs.5.12 (a) and (b) respectively.

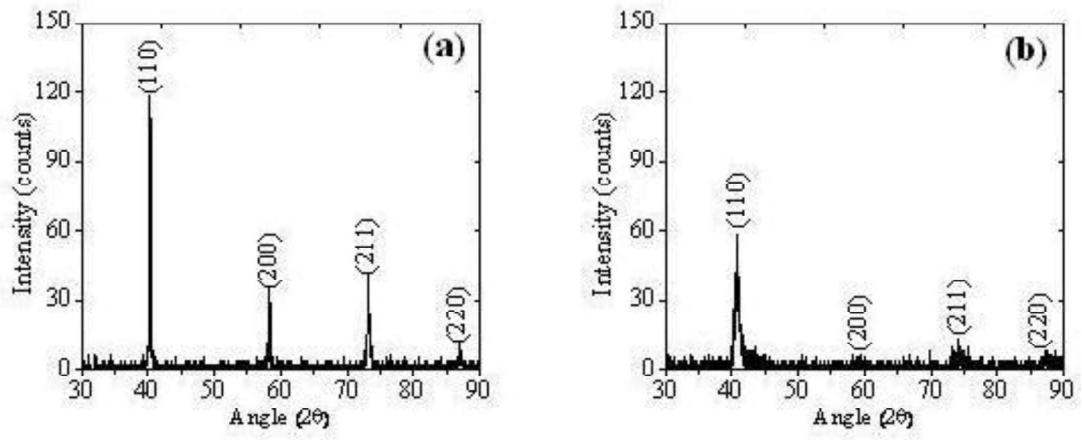

FIG. 5.12 X-ray diffraction profile of tungsten sample (a) before and (b) after exposed to 20 PF discharges.

The diffraction peaks belong to body centered cubic (BCC) phase of the W and there are no other phases formed after irradiations. The shifts in angular positions are different for different peaks. This is possibly due to the non-steady state heat influence into the deeper solid layers and multifold recrystallization under exposure to multiple deuterium ions pulses [Ivanov et al. 2000]. The (110) diffraction peak shifts by 0.38 deg. i.e. from 40.34 to 40.72 deg. so the corresponding value of strain is 0.0078. The elastic constant of the W is 411 GPa and therefore the residual stress is estimated to be 3.21 GPa. Similarly, the residual stresses on other samples are calculated using shift in 2θ angle of most intense diffraction peaks in the XRD profiles of exposed samples with respect to unexposed samples.

The XRD profiles of irradiated Ni, Mo and Cu have similar characteristics as shown in figs 5.13, 5.15 and 5.16 respectively.

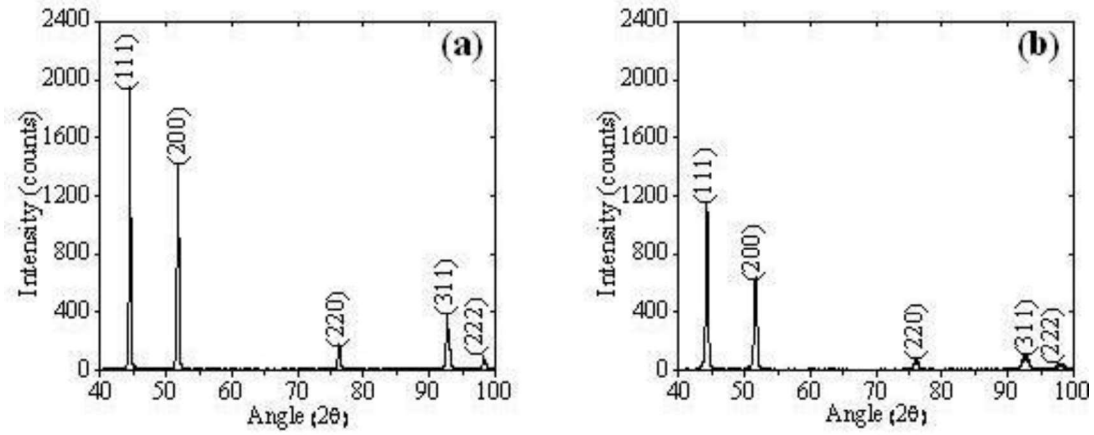

FIG.5.13 X-ray diffraction profile of nickel samples (a) before and (b) after exposed to 20 PF discharges.

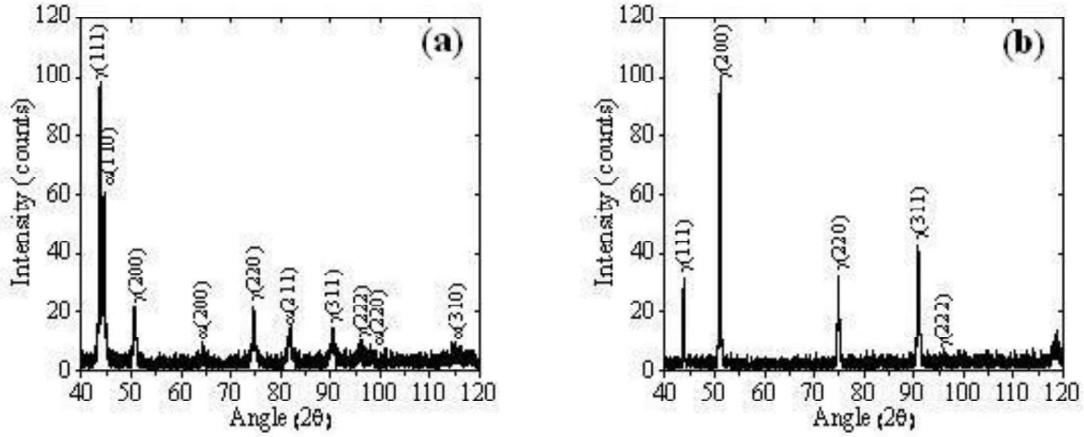

FIG.5.14 X-ray diffraction profile of stainless steel sample (a) before and (b) after exposed to 20 PF discharges.

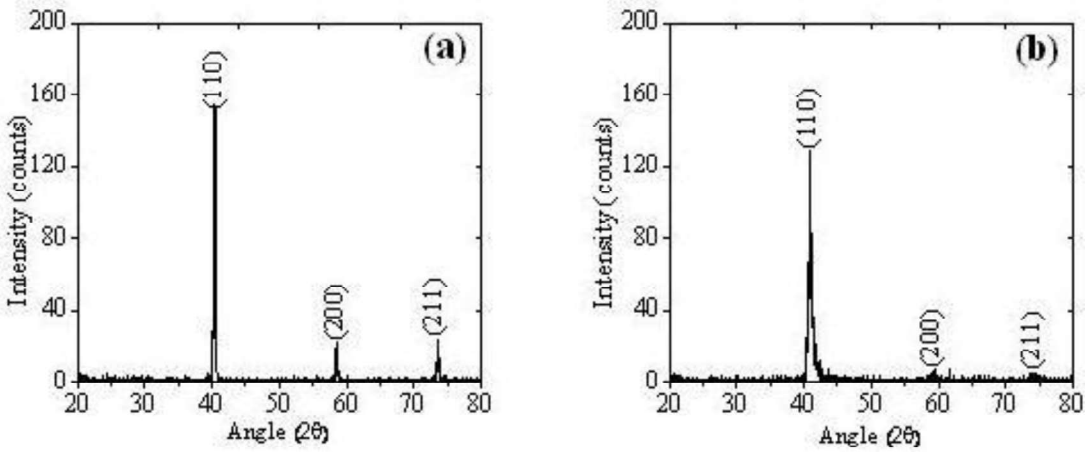

FIG. 5.15 X-ray diffraction profile of molybdenum sample (a) before and (b) after exposed to 20 PF discharges.

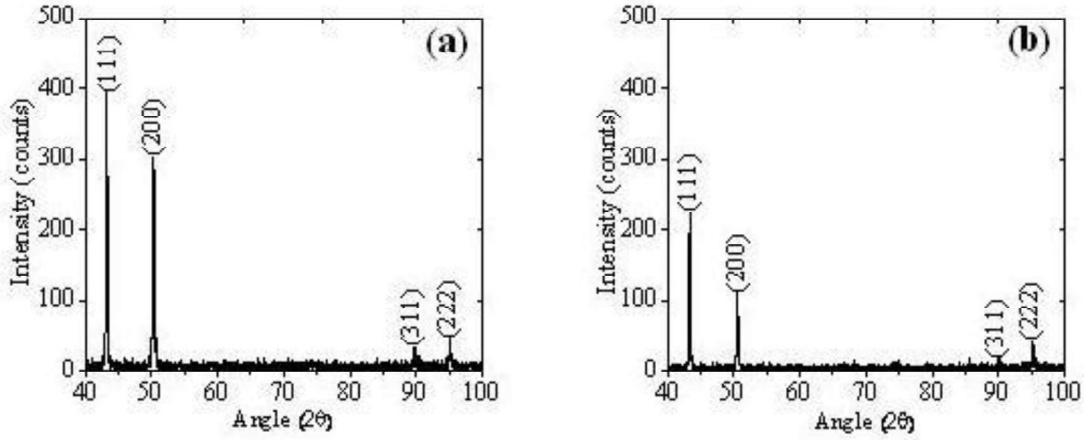

FIG. 5.16 X-ray diffraction profile of copper sample (a) before and (b) after exposed to 20 PF discharges.

The BCC phase of the Mo does not change after irradiations but the diffraction peaks corresponding to (200) and (211) reflection planes diminish as seen in the fig.5.15(b). The angular position of the (110) diffraction peak is shifted by 0.54 deg. so the corresponding strain value is 0.011. The elastic constant of Mo is 329 GPa and therefore residual stress is estimated to be 3.6 GPa. The (111) diffraction peaks corresponding to face centered cubic (FCC) phase of Ni and Cu have shifted by 0.2 deg. and 0.14 deg respectively. The strain values for Ni and Cu are calculated to be 0.0029 and 0.0026 respectively. The values of elastic constants for Ni and Cu are 200 GPa and 120 GPa respectively and corresponding residual stresses are 0.58 GPa and 0.31 GPa respectively.

The ferrite (α) to austenite (γ) structural phase transitions is observed in the XRD profile of the SS sample after irradiations as seen in fig.5.14. The XRD profile of unexposed SS304 sample has mixed microstructures of the austenitic (γ) and the ferrite (α) phases. The observed diffraction peaks γ (111), γ (200), γ (220), γ (311) and γ (222) and α (110), α (200), α (211), α (220) and α (310) correspond to the reflection planes of the austenite (γ) and the ferrite (α) phases of the virgin SS. The exposure to twenty shots has resulted in the change of the relative volumes of the austenite (γ) and the ferrite (α) phases. After multiple irradiations, the diffraction peaks corresponding to ferrite phase

diminish. An increase in the intensity of the γ (111) and γ (222) and reduction of intensities of the γ (200), γ (220) and γ (311) are observed due to non-steady state heat influence on the SS sample. Ivanov et al. [2000] measured significant change in relative volume of the austenite (γ) and ferrite (α) phase in the 10Cr12Mn20W steel and 25Cr12Mn20W steel under the multifold exposures to deuterium ion pulses and deuterium plasma streams in dense plasma focus. Morozov et al. [2015] observed phase structural transformations in austenitic 18Cr10NiTi SS to martensitic SS upon implantation with deuterium ions at atomic concentration (ratio of atomic density of deuterium to material) of ≥ 0.5. The structural phase transformation is probably due to change in lattice parameters of the austenite-ferrite SS as implanted deuterium ions may occupy interstitial lattice sites Moreover, shock wave could also result in displacement of atoms into an interstitial position which could trigger the phase structural transformations. The shift in γ (111) diffraction peak is 0.02 deg. and the corresponding strain value is 0.0004. The elastic constant value is 193GPa and therefore residual stress is estimated to be 0.08 GPa. Therefore, residual stresses after irradiation are of 0.08 GPa, 0.31 GPa, 0.58 Gpa, 3.21 GPa and 3.6 GPa for SS, Cu, Ni, W and Mo respectively.

5.1.2.4 EDX analysis

The measurements of elemental content using EDX suggested no change in chemical compositions as the deuterium ions largely remain undetected in the EDX measurement. The EDX analysis show that elements of the anode material (SS) have deposited over the irradiated samples. The reason is that the relativistic electrons having energy up to a few MeV are accelerated in the axially downward direction and erode the anode materials. After multiple irradiations, the eroded material mix with the melted surface layer in liquid phase and it results in to alloying of sample surface layer uniformly. The elemental composition (weight %) of surfaces of different material samples before and after irradiations is depicted in table 5.3. The error in EDX measurement is ≤ 1% for all elements. The surfaces of irradiated W, Mo, and Cu contain Ni, Fe and Cr which are alloying

elements of the anode material. These elements are not present before irradiation. Similarly, Ni and SS form alloy with the anode material after irradiations. The erosion of anode material is attempted to reduce by using deep hollow anode. This can further be reduced to a very large extent by inserting material having higher threshold for erosion such as tungsten at the tip of the anode.

Table 5.3: Elemental compositions (wt %) of various samples before and after irradiations.

Material		W	Mo	Cu	Ni	Fe	Mn	Cr	O	C
Anode		-	-	-	7.92	69.57	2.16	17.72	-	2.64
W	Before	91.48	-	-	-	-	-	-	4.66	3.86
	After	58.53	-	-	4.1	26.07	-	7.37	-	3.94
Ni	Before	-	-	-	100	-	-	-	-	-
	After	-	-	-	54.42	33.86	-	8.69	3.03	-
SS	Before	-	-	-	8.29	70.28	2.06	17.73	-	1.64
	After	-	-	-	7.81	69.49	2.27	18.41	-	2.02
Mo	Before	-	77.18	-	-	-	-	-	22.82	-
	After	-	65.59	-	3.08	21.88	-	6.05	-	3.40
Cu	Before	-	-	94.42	-	-	-	-	2.23	3.35
	After	-	-	72.23	2.73	16.69	-	4.69	1.34	2.32

5.2. Carbon nanostructure formations

The hot and dense plasma in the focus phase is being used to evaporate materials kept at the tip of the anode. The evaporated materials are deposited over substrate and form a thin film over substrate. Thin films of elements as well as compound materials are being deposited over any substrate in good stoichiometry. Thickness of the thin films or the size of the nanoparticles depend strongly on plasma focus parameters such as operation energy, filling gas species and its pressure, number of plasma focus deposition shots [R. S. Rawat et al. 2001]. Pan et al. [2009] reported the deposition of nanostructured cobalt-platinum (CoPt) on Si using repetitive NX2 device. The CoPt thin films was synthesized at various filling hydrogen gas pressures (2, 4, 6 and 8 mbar) at a fixed distance of 25 cm from the anode top by 25 deposition shots at 1 Hz repetition rate. The thicknesses of the CoPt thin films deposited at 2, 4, 6 and 8 mbar were measured to be around (94 ± 4.0) nm,

(58 ± 3.0) nm, (44 ± 2.0) nm and (22 ± 1.0) nm respectively. They correlated the decrease in thickness to decrease in focusing efficiency with increasing pressure. J. J. Lin et al. [2008] used 3kJ plasma focus device for synthesis of uniform FePt nanoparticles through nano-structuring of pulsed laser deposited FePt thin films by single shot H^+ irradiation.

Bhuyan et al. [2007] used plasma focus device for formation of hexagonal silicon-carbide (SiC) layer on Si(100) substrate. They irradiated high-energy ion beam on Si (100) substrates using a 1.8 kJ plasma focus device operating in methane gas. The interaction of the energetic carbon ions (60–450 keV) with the Si surface results in the formation of silicon-carbide. Further, the carbon ion beams produced in the 1.8 kJ plasma focus device were used for production for sub micrometer-sized carbon composite coatings on different substrates including Si (100) and Ti. On Si substrate, a step-bunched surface layer of hexagonal SiC or an amorphous carbon layer is formed, depending on the focus anode material whereas on Ti, gradient layers of titanium-carbide (TiC) with embedded carbon nanostructures were observed. The natural angular anisotropy of the focus ion beams allowed investigation of the effect of ion beam characteristic energy and flux on the resulting coatings using SEM, EDX, XRD, AFM, AES, and Raman spectroscopy techniques [Bhuyan et al.2010].,

In present work, PF-2 device is used for deposition of carbon nanostructures on Si substrate. The silicon substrate (8 mm x 8 mm x 0.5 mm) is placed at 10 cm axial distance from the anode tip and operated with 0.5 mbar of Acetylene (C_2H_2) gas at 2 kJ. The schematic of setup is shown in fig. 5.17. The substrate is exposed to 50 shots. In another experiment, graphite rod is inserted in the hollow anode and substrate is exposed to 50 shots. In each shot, the ablated graphite material along with the chemical precursors such as C_2H_2+, CH+, C+, etc. get deposited over the substrate. The thickness of the deposited films depends on the number of shots. Effect of ablation of graphite, angular emission of ions and number of shots are studied by characterizing the deposited thin films. The deposited thin films are characterized using SEM, Raman Spectroscopy and EDX. Typical SEM

images of thin films deposited using hollow anode and graphite rod inserted anode by 50 shots are shown in figs. 5.18(a) and (b) respectively.

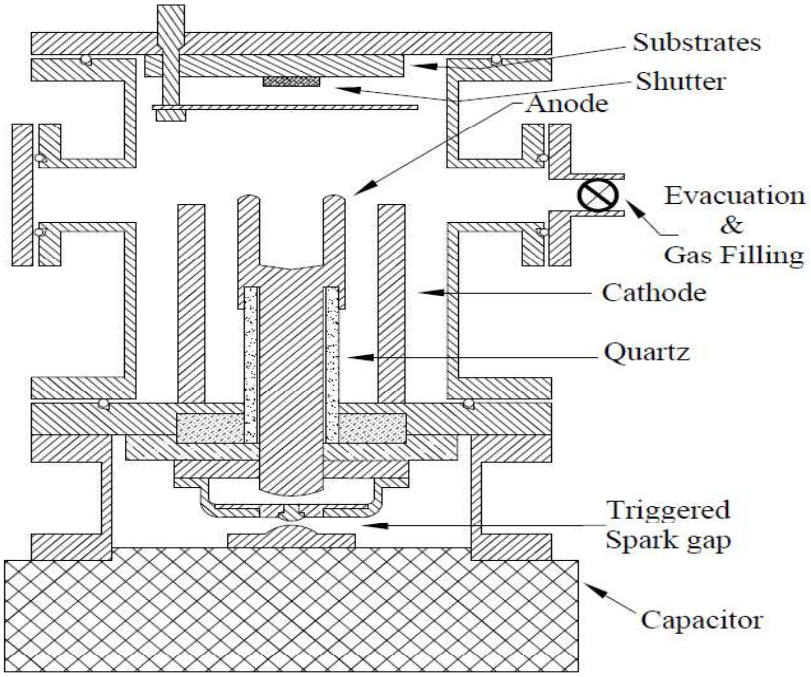

FIG.5.17 Schematic of thin film deposition setup.

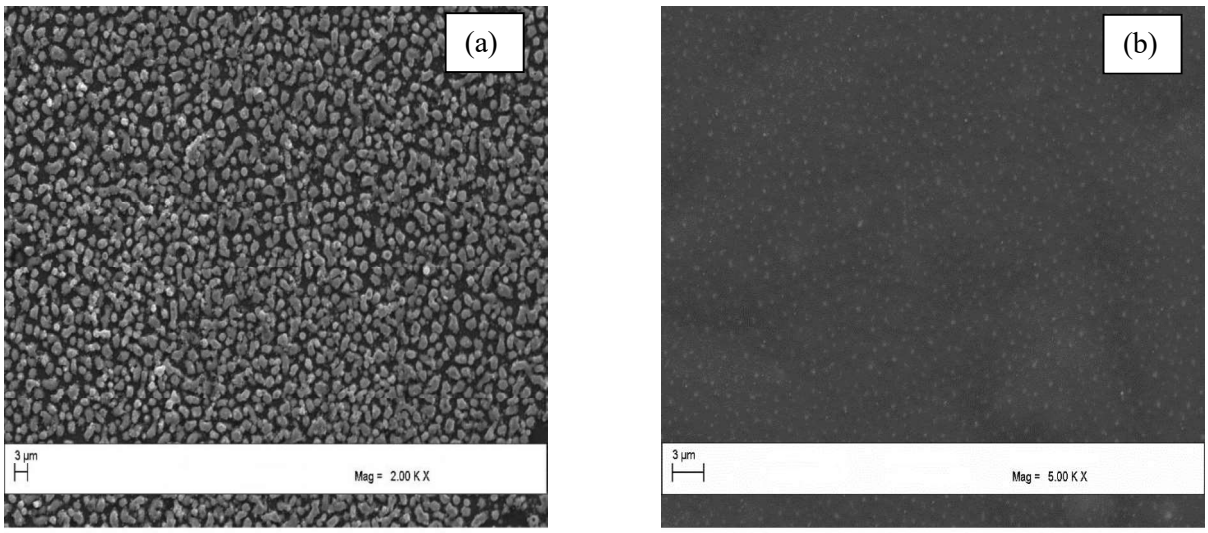

FIG. 5.18 Typical SEM image of thin films formed over the Si substrate (a) without graphite insert and (b) with graphite insert using PF-2 device.

Clusters of size typically of several hundreds of nm to a few μm are formed using former method whereas uniform and smooth thin film is formed using graphite inserted anode. Clusters are distributed uniformly over the substrate as seen in fig. 5.18(a). The possible reason of formation of clusters is the energetic precursors which deposit and diffuse over the Si substrate to form clusters of various sizes. As seen in fig. 5.18(b), uniform thin film of carbon is deposited due to the ablation of graphite materials.

The exposed Si substrates have also been characterized using Raman Spectroscopy. The Raman spectrum [figs. 5.19(a) to (b)] suggests that the deposited thin films are of diamond like carbon (DLC) with two peaks corresponding to D and G band. The peak characteristics such as intensity, peak width, and peak positions are signature of DLC properties. The intensity ratio of the two peaks i.e. I_D/I_G is related to the content of sp^3 bonded carbon in the film [Namba et al. 1992, Wang et al. 1997, Beeman et al. 1984, Dillon et al. 1984]. The FWHM of the G peak is related to the size of the sp^2 cluster as well as content of the sp^2 bonded carbon. The peak characteristics can be determined by de-convolution using multi-peak Lorentzian fitting. It is observed that the position of G peak shifts towards lower wave number from 1584 to 1575 cm^{-1} and the FWHM of G peak decreases from 97.6 to 45.7 when deposited using graphite inserted anode.

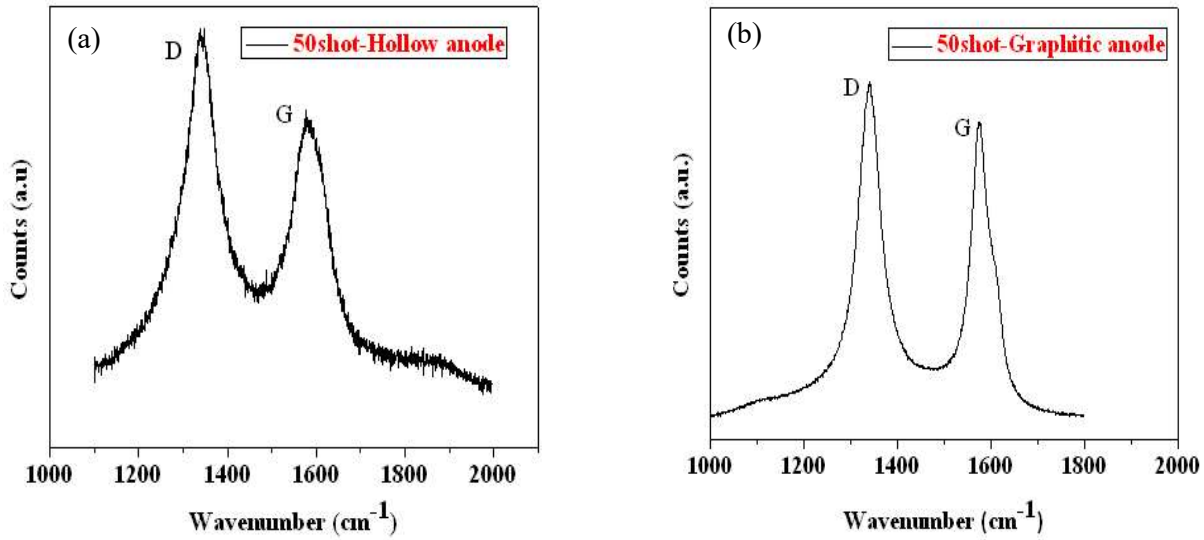

FIG. 5.19 Typical Raman spectrum of thin films deposited using (a) hollow anode and (b) Graphite inserted anode.

5.3 Assay of nuclear fissile material

Plasma focus devices as a neutron source have many applications such as neutron activation analysis, and short-lived radio-isotope productions. Nuclear activation analysis (NAA) is a non-destructive method to determine absolute mass of different elements in samples as well as for detection of elements present in sub-ppm range. It is independent of form of samples. In this method, fast ($\geq$ 1 MeV) and thermal (0.025 eV) neutrons are used to irradiate samples followed by detection of reaction products. The decay gamma spectrum is characteristics of a nucleus which allows their identification and quantification. Both, prompt and delayed gammas are used for analysis of samples.

NAA has been used for active assay of nuclear fissile materials [Uranium (^{235}U)] using delayed neutron counting [Raoux et al. 2003, Lyoussi et al. 2000, Lakosi et al. 2011] and delayed gamma counting [Fisher et al. 1964, Hollas et al. 1986, Beddingfield et al. 1998]. Neutron sources normally used are spontaneous fission based neutron source (^{252}Cf), radioisotopes based (α, n) neutron source (Am-Be, and Pu-Be), fission reactors and particle accelerators (cyclotrons or LINACs). In the case of^{252}Cf, the source is stored behind a shielding (for gamma rays and neutrons) and it is brought to the sample for a short period after which it is quickly pushed back to the shield. However, despite the shielding, the background neutrons cannot be completely eliminated leading to an increase in the detection limit. In the case of the D-T LINAC, the neutron pulse repetition rate (typically few Hz) results in the rise and fall of delayed neutron counts during irradiation and hence the de-convolution of the decay profile into individual delayed neutron groups is difficult. Plasma focus based neutron source is desirable over other neutron sources since it produces high neutrons with short pulse duration (several 10s of ns). Therefore, efforts are made by many researchers [Verri et al. 2000, Tartari et al. 2002, Gribkov et al. 2010] to see feasibility of plasma focus in the activation of substances for their detection and also to produce short-lived isotopes. Such feasibility studies have also been carried out in present work as described further.

Non-destructive assay (NDA) of ^{235}U in U_3O_8 samples using MEPF-12 device has been performed and reported [Tomar et al. 2013]. Different amounts of U_3O_8 samples (0.1 to 40 g) containing enriched ^{235}U (14.8%) are irradiated separately with (1.2 ± 0.3) x 10^9 neutrons/pulse having pulse duration of (46 ± 5) ns. Subsequently delayed neutrons and/or delayed gammas from activated samples are measured using appropriate detectors. The samples are in powder form doubly sealed in a polyvinyl chloride (PVC) bag of size 50 x 50 mm^2. They are placed inside a cylindrical cavity kept along the axial direction. The cavity is made of high density polythene (HDPE) of size: 60 mm diameter and 30 mm depth. The effective HDPE thickness of 40 mm is used for moderation of 2.45 MeV neutrons. The delayed neutrons from activated samples are measured using ^3He detectors coupled to a data acquisition system operating in multichannel scaling (MCS) mode. The schematic of experimental setup is shown in fig.5.20.

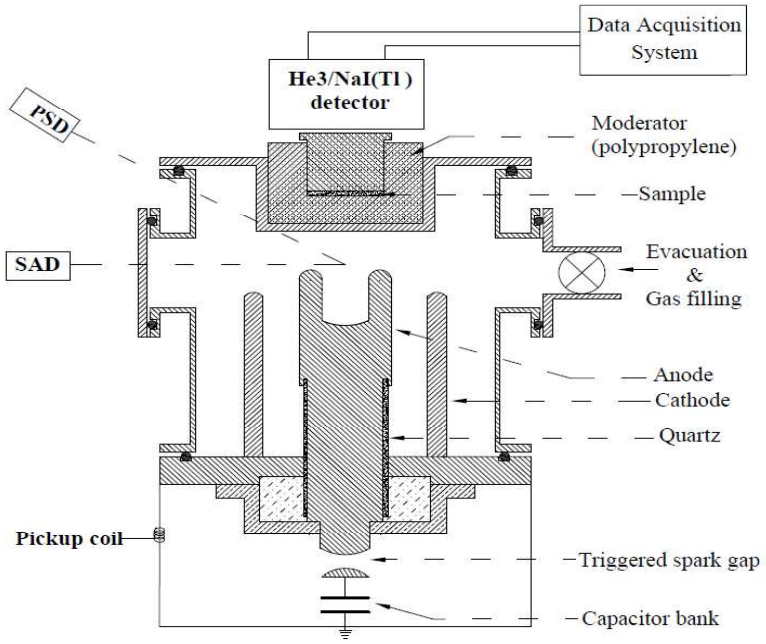

FIG. 5.20 Schematic of the experimental setup for assay of nuclear fissile materials.

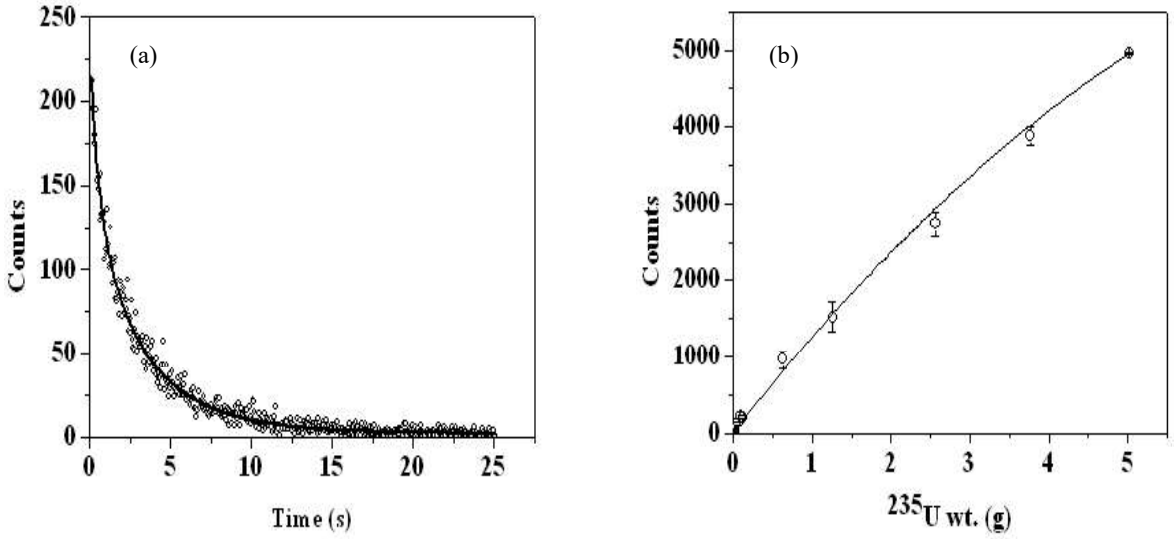

FIG. 5.21 (a)Temporal profile of delayed neutron counts (solid line is multi-exponential fit) and (b) calibration graph of delayed neutron count rate vs ^{235}U mass with second order polynomial fits.

Fig. 5.21a shows typical temporal spectrum of delayed neutrons from a sample containing 40 g of U_3O_8. Fig. 5.21b shows the plot of time integrated delayed neutron counts for 25 s (normalized to the neutron yield) as a function of ^{235}U mass. It appears that the time integrated delayed neutron counts increase nearly linearly with the ^{235}U content. However, it is best fitted using second order polynomial ($a + bw + cw^2$) where a = (12.7 ± 2.5), b = (1308.1 ± 72.6) and c = (-64.6 ± 14.5) and w is the mass of ^{235}U. The detection limit (D) of the system is determined using the formula $D_n = C_{b,n} + 3\sigma_{b,n}$. Here, $C_{b,n}$ is average background and $\sigma_{b,n}$ is standard deviation of the average background. The detection limit is found to be 18 mg of ^{235}U. The detection limit is further expected to be less with high neutron yield.

In another experiment, delayed gammas from the irradiated U_3O_8 samples are measured [Andola et al. 2014] using NaI(Tl) scintillator detector coupled to a data acquisition system in MCS mode. The schematic of experimental setup is shown in fig. 5.20. Fig. 5.22(a) shows the time profile of delayed gammas (above 3 MeV) from a sample containing 5 g of U_3O_8. Fig. 5.22(b) shows time

integrated delayed gamma counts for 100 s (normalized to the neutron yield) as a function of ^{235}U mass.

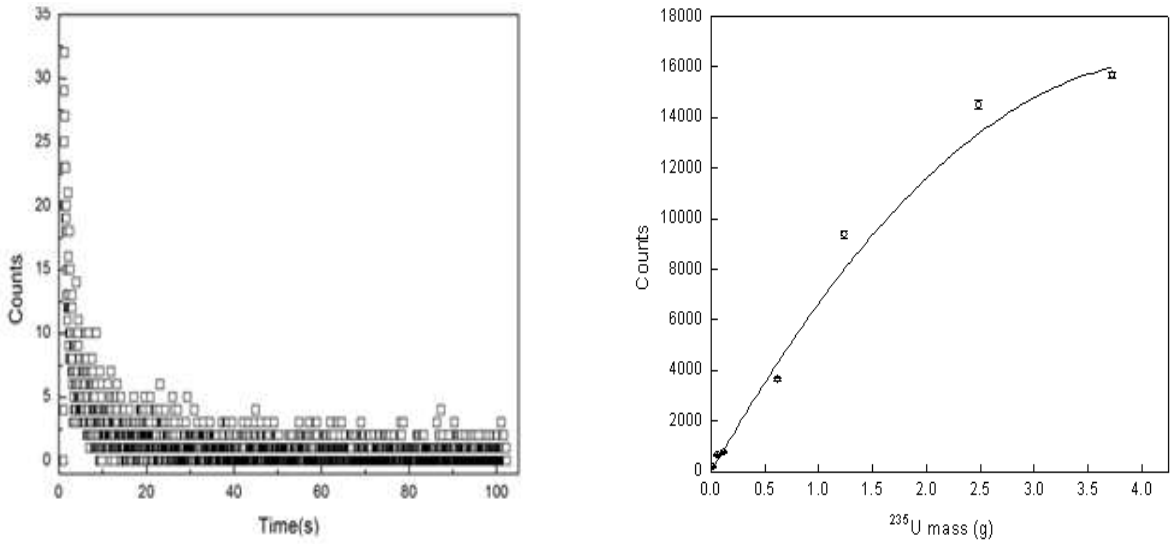

FIG. 5.22(a)Temporal profile of delayed gamma radiation counts and (b) calibration graph of delayed gamma radiation count rate vs ^{235}U mass with second order polynomial fits.

The delayed gamma counts are best fitted using second order polynomial ($a + bw + cw^2$) where a = -61.48, b = 7591.6 and c = -881.52. The detection limit (D) of the system is determined using the formula $D= C_{b,\gamma} + 3\sigma_{b,\gamma}$ and it is found to be 14 mg of ^{235}U. Here, $C_{b,\gamma}$ and $\sigma_{b,\gamma}$ is the delayed gamma radiation background and standard deviation of the background respectively.

5.4 Short-lived Radioisotopes production and half-life measurement

Various short-lived radio-isotopes [^{198}Au, ^{56}Mn and ^{165m}Dy] are produced using MEPF-12 device and their half-life is estimated from decay gamma spectrum [Rout et al. 2013]. Approximately one gram of each samples namely gold-chloride ($AuCl_3$), manganese-oxide (MnO_2) and dysprosium-oxide (Dy_2O_3) are irradiated using single or multiple shots in MEPF-12 device operated with deuterium as the filling gas. The samples are in powder form doubly sealed in a polyvinyl chloride (PVC) bag of size 50 x 50 mm^2. They are placed inside a cylindrical cavity kept along the axial direction. The cavity is made of high density polythene (HDPE) of size: 60 mm diameter and 30 mm

depth. The effective HDPE thickness of 40 mm is used for moderation of 2.45 MeV neutrons. The decay gammas are measured offline using a NaI(Tl) detector coupled to a calibrated multichannel analyzer (MCA). The experimental setup (fig. 5.20) used here is same to that for non-destructive assay of fissile materials. The neutron yield in each shot is measured to be $(1.2 \pm 0.3) \times 10^9$ neutrons/pulse with pulse duration of (46 ± 5) ns.

The $AuCl_3$ sample is exposed to eight shots. By capturing thermal neutrons, the nuclide ^{197}Au transforms into ^{198}Au through the neutron capture reaction ^{197}Au (n, γ) ^{198}Au. The cross-section for the nuclear reaction is 98 b. The radioisotope ^{198}Au has a mean lifetime of 2.7 days [Mughabghab 2003]. It then, via β decay, passes to an excited ^{198}Hg which decays to the ground state by emitting gamma radiation of 412 keV energy [Be et al., 2008]. Typical time profile and energy spectrum of gamma radiations from the irradiated $AuCl_3$ sample are in fig. 5.23 (a) and (b) respectively. The half-life of ^{198}Au measured from decay gamma counts is 2.84 ± 0.6 days. This is approximately same as that of reported half-life of 2.69 days [Heath 1997].

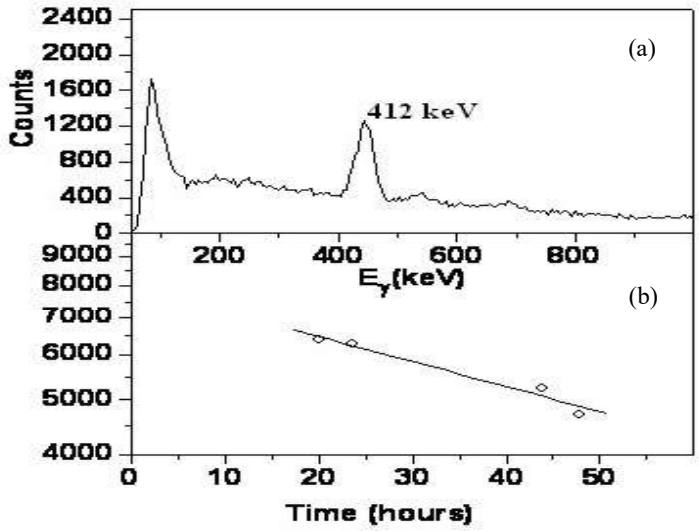

FIG. 5.23 (a) Energy spectrum and (b) decay gamma counts from decay of ^{198}Au.

Similarly, for Manganese, the reaction by neutron capture is ^{55}Mn (n, γ) ^{56}Mn with cross-section of 15 b [Mughabghab 2003]. The ^{56}Mn then decays to ^{56}Fe with half-life of 2.57 h. The energy spectrum and temporal profile of decay gammas are measured. Typical energy spectrum and temporal profile of decay gammas are shown in fig. 5.24(a) and (b) respectively.

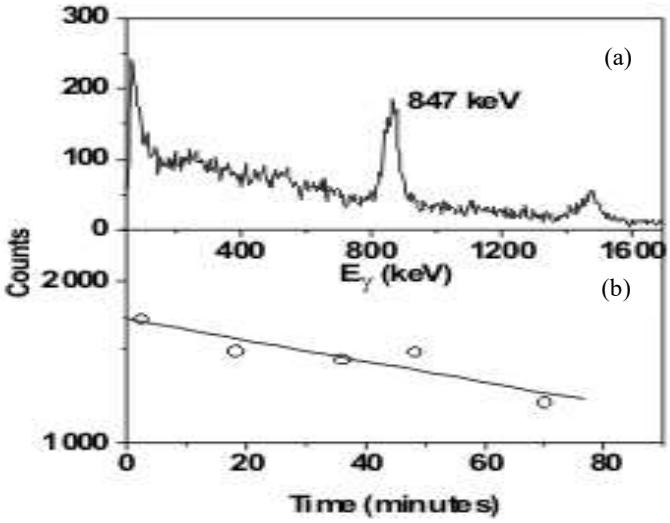

FIG 5.24 (a) Energy spectrum and (b) decay gamma counts from decay of ^{56}Mn.

As seen in fig. 5.24(a), a characteristic peak at 847 keV corresponds to ^{56}Mn decay [Be et al. 2008]. The half-life obtained from the decay profile is 2.56 hrs., approximately same to that of literature value of 2.58 hrs [R. L. Heath 1997].

The natural dysprosium has seven isotopes: ^{156}Dy, ^{158}Dy, ^{160}Dy, ^{161}Dy, ^{162}Dy, ^{163}Dy, and ^{164}Dy. It also has at least 11 metastable isomers, ranging in atomic mass from 140 to 165 and the most stable of these is ^{165m}Dy which has a half-life of 1.257 min. [Mughabghab 2003]. The ^{165m}Dy β^-decays to ^{165}Ho (stable). The neutron capture reaction is ^{165}Dy (n, γ) ^{165m}Dy with cross-section of 2100 b. After the irradiation, the gamma rays resulting from the decay of ^{165m}Dy are measured. A characteristic peak is observed at 165 keV [Be et al., 2008] which corresponds to decay of ^{165m}Dy. Typical energy spectrum and temporal profile of decay gamma rays have been shown in fig. 5.25(a) and (b)

respectively. The half-life of ^{165m}Dy obtained from the decay profile is 86 s, close to the literature value (78 s) [R. L. Heath 1997].

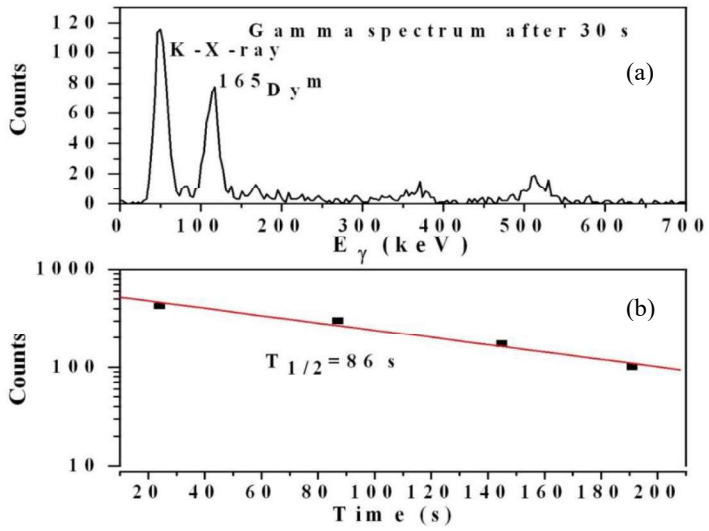

FIG. 5.25 (a) Energy spectrum and (b) decay gamma counts from decay of ^{165m}Dy.

5.5 Summary and conclusion

Plasma focus devices are used for wide range of applications ranging from short-lived radioisotope production to study of fusion reactor relevant materials surface damage. The high power density ions and plasma produces damages (thermal as well as radiative). The thermal damage consists of melting and evaporation as well as micro-cracks due to thermal stress on the surface layer of material. The radiation damage consists of sputtering of surface layer as well as various crystalline effects such as vacancies, interstitials, pores, bubbles etc. Comparative analysis of surface damages on the samples of various materials suggests that they are highly dependent on materials physical, thermal as well as mechanical properties. Among the samples studied here, the W has the least and the Cu has the most damage in various forms. The reason is attributed to various properties of W such

as the high melting point (3695 K), high threshold for sputtering (212 eV), high elastic constant (411 GPa) among others. The study reinforces for use of W as the first wall material in ITER fusion reactor.

The observed phase transition (ferritic-austenitic to austenitic) in SS is attributed to the fact the implanted deuterium atoms occupy interstitial sites which triggers the phase transition. Moreover, shock wave could also result in displacement of atoms of alloying elements into an interstitial position which could trigger the phase structural transformations. This study shall prove to be useful in understanding pulse fusion grade plasma and material interaction and also in predicting various other materials behavior in fusion reactor environment.

Study on deposition of DLC on Si substrate and its characterization further bolsters the position of plasma focus device as tool to modify the surface tribological properties through coatings of various materials on different substrate materials.

Non-destructive assay of ^{235}U in varying masses of U_3O_8 samples is performed using pulse neutrons. Detection of ^{235}U as low as 14 mg using this method proves that plasma focus device can be efficiently and effectively used for detection of explosives and illicit materials present in trace amount.

Feasibility study on production of short-lived radioisotopes (^{56}Mn, ^{198}Au, ^{165m}Dy) and their half-life measurements proves potential applications of plasma focus devices in producing radioisotopes for application in different areas such as for medical applications [Boron Capture Neutron Therapy (BCNT)].

References

1. "Use of delayed gamma rays for active non-destructive assay of ^{235}U irradiated by pulsed neutron source," Andola S., Niranjan R., Kaushik T. C. et al., *Nucl. Instrum. Methods Phys. Res.* A, **2014**, *753*, 138–142.
2. "Material challenges for ITER-current status and future activities", Barabash V., The ITER International team, Peacock A. et al., *J. Nucl. Mat.,* **2007**, *367-370*, 21-32.

3. "Identification of fissile materials from fission product gamma-ray spectra" Beddingfield D.H., Cecil F.E., *Nucl. Instrum. Methods Phys. Res. A,* **1998**, *417*, 405-412.

4. "Modeling studies of amorphous carbon", Beeman D., Silverman J., Lynds R. et al., *Phys. Rev. B,* **1984**, *30(2)*, 870-875.

5. "Formation of hexagonal silicon carbide by high energy ion beam irradiation on Si (100) substrate", Bhuyan H., Favre M., Valderrama E. et al., *J. Phys. D: Appl. Phys.,* **2007**, *40*, 127–131.

6. "High energy ion beam irradiation on titanium substrate in a pulsed plasma device operating with methane", Bhuyan H., Favre M., Valderrama E. et al., *J. Phys. D: Appl. Phys.,* **2009**, *42*, 205207-1-8.

7. "Plasma focus assisted damage studies on tungsten," Bhuyan M., Mohanty S. R., C. V. S. et al., *Appl. Surf. Sci.,* **2013**, *26*, 674-680.

8. "Plasma surface interaction issues of an all-metal ITER," Brooks J. N., Allain J. P., Doerner R. P. et al., *Nucl. Fusion,* **2009**, *49*, 035007(1-6).

9. "Radiation damage (blistering) in Al, Cu, Si by exposure to a plasma focus discharge," Bostick W. H., Nardi V., Prior W. et al., *J. Nucl. Mat.,* **1976**, *63*, 356-372.

10. "Conduction of heat in solids", Carslaw H. S., Jaeger J. C., second ed., Clarendon press, Oxford, 2001.

11. "Use of Raman scattering to investigate disorder and crystallite formation in as-deposited and annealed carbon films", Dillon R. O., Woollam J. A., *Phys. Rev. B,* **1984**, *29(6)*, 3482-3489.

12. "Damage studies on tungsten due to helium ion irradiation", Dutta N. J., Buzarbaruah N., Mohanty S. R., *J. Nucl. Mat.,* **2014**, *452*, 51-56.

13. "The role of implanted gas and lateral stress in blister formation mechanisms", Evans J. H., *J. Nucl. Mat.*, **1978**, *76-77*, 228-234.

14. "Plasma-material interactions in current tokamaks and their implications for next step fusion reactors", Federici G., Skinner C. H., Brooks J. N.et al., *Nucl. Fusion,* **2001**, *41(12R)*, 1967-2137.

15. "Nitrogen implantation of AISI 304 stainless steel with a coaxial plasma gun", Feugeas J., Llonch E. C., de Gonzalez C. O. et al., *J. Appl. Phys.,* **1988**, *64*, 2648–2651.

16. Energy and time dependence of delayed gammas from fission", Fisher P. C., Engle L. B., *Phys. Rev.,* **1964**, *134*, B796.

17. "Plasma dynamics in PF-1000 under full-scale energy storage:I. Pinch dynamics, shock-wave diffraction and inertial electrode", Gribkov V. A., Bienkowska B., Borowiecki M. et al., *J. Phys. D: Appl. Phys.,* **2007**, *40*, 1977.

18. "A dense plasma focus-based neutron source for a single-shot detection of illicit materials and explosives by a nanosecond neutron pulse", Gribkov V. A., Latyshev S. V., Miklaszewski R. A. et al., *Phys. Scripta.,* **2010**, *81*, 035502.

19. "Scintillation Spectrometry: Gamma-ray Spectrum Catalogue," Heath R. L., Report IDO-16880-1, 2nd Edition-Vol.1(rev.), **1997**.

20. "ITER Relevant High Heat Flux Testing on Plasma Facing Surfaces", Hirai T., Ezato K., Majerus P., *Mat. Trans.,* **2005**, *46(3)*, 412-424.

21. "Analysis of fissionable material using delayed gamma rays from photo-fission", Hollas C. L., Close D. A., Moss C. E., LA-UR 86-3363, **1986**.

22. "Confinement and divertor studies in Alcator C-Mod", Hutchinson I. R. et al, *Plasma Phys. Control. Fusion,* **1994**, *36***,** B14.

23. "Influence of Dense Deuterium Plasma Pulses on Materials in Plasma Focus Device", Ivanov L. I., Pimenov V. N., Maslyaev S. A. et al., *Nukleonika,* **2000**, *45(3)*, 203-207.

24. http://www.srim.org/ - J. Ziegler-SRIM&TRIM.

25. "Erosion yield of metal surface under ion pulsed irradiation", Krivobokov V., Stepanova O., Yuryeva A., *Nucl. Instrum. Methods Phys. Res. B,* **2013**, *315*, 261-264.

26. "Neutron interrogation of shielded/unshielded uranium by a 4 MeV LINAC", Lakosi L., Nguyen C. T., Serf E., *Appl. Radioisotop.,* **2011**, *69*, 1251–1254.

27. "FePt nanoparticle formation with lower phase transition temperature by single shot plasma focus ion irradiation", Lin J. J., Roshan M. V., Pan Z. Y. et al., *J. Phys. D: Appl. Phys.,* **2008**, *41*. 135213(1-6).

28. "Transuranic waste detection by photon interrogation and on-line delayed neutron counting", Lyoussi A., Romeyer-Dherbey J., Jallu F. et al., *Nucl. Instrum. Methods Phys. Res. B,* **2000**, *160*, 280-289.

29. "Effect of surface morphology on the sputtering yields. I. Ion sputtering from self-affine surfaces", Makeev M. A., Barabasi A. L., *Nucl. Instrum. Methods Phys. Res. B,* **2004**, *222*, 316-334.

30. "The behaviour of surfaces under ion bombardment", Mcckacken G. M., *Rep. Prog. Phys.,* **1975**, *38*, 241-327.

31. "Structural transformations in austenitic stainless steel induced by deuterium implantation: irradiation at 100K", Morozov O., Zhurba V., Neklyudov I. et al., *Nanoscale Res. Lett.,* **2015**, *10*,154.

32. "Thermal neutron capture cross sections resonance integrals and g-factors", Mughabghab S. F., IAEA, **2003**, INDC(NDS)-440, 7-32.

33. "Attempt to grow diamond phase carbon films from an organic solution", Namba Y., *J. Vac. Sci. Tech. A,* **1992**, *10(5)*, 3368-3370.

34. "Nanostructured magnetic CoPt thin films synthesis using dense plasma focus device operating at sub-kilojoule range", Pan Z. Y., Rawat R. S., Roshan M. V. et al., *J. Phys. D: Appl. Phys.,* **2009**, *42*, 175001-1-12.

35. "Damage and modification of materials produced by pulsed ion and plasma streams in dense plasma focus device", Pimenov V. N., Demina E. V., Maslyaev S. A. et al., *Nukleonika,* **2008**, *53(3)*, 111-121.

36. "Influence of powerful pulses of hydrogen plasma upon materials in PF-1000 device", Pimenov V. N., Gribkov V. A., Dubrovsky A. V. et al., *Nukleonika,* **2002**, *47(4)*, 155- 162.

37. "Table of Radionuclides (Comments on evaluation)", `Rao M. M. Be, Chiste V., Dulieu C. et al, *Bureau International Des Poids ET Mesures,* **2008**, *1-4*, 1-829.

38. "Transuranic waste assay by neutron interrogation and online prompt and delayed neutron measurement", Raoux A. C., Lyoussi A., Passard C. et al., *Nucl. Instrum. Methods Phys. Res. B,* **2003**, *207*, 186–194.

39. "Room temperature deposition of titanium carbide thin films using dense plasma focus device," Rawat R. S., Lee P., White T. et al., *Surf. Coat. Technol.,* **2001**, *138*, 159-165.

40. "Crystallization of an amorphous lead zirconate-titanate thin film with a dense-plasma-focus device", Rawat R. S., Srivasatva M. P., Tandon S. et al., *Phys. Rev. B,* **1993**, *47*, 4858–4862.

41. "Chamber wall materials response to Pulsed ions at power plant level fluence," Renk T. J., Provencio P. P., Tanaka T. J. et al., *J. Nucl. Mat*., **2005**, *347*, 266-288.

42. "Evaluation of Half Lives Through Thermal Neutron Activation Using Plasma Focus Neutron Source," Rout R. K., Tomar B. S., Ramanjaneyulu P. S. et al., *28th National Symp. Plasma Sci. Technol.* (PLASMA-2013), KIIT Bhubaneswar, India, **2013**.

43. "The thermal evolution of target under plasma focus pulsed ion implantation", Sanchez G., Feugeas J., *J. Phys. D: App. Phys.,* **1997**, *30*, 927-936.

44. "Deuterium retention, blistering and local melting at tungsten exposed to high-fluence deuterium plasma", Shu W. H., Nakamichi M., Alimov V. K. et al., *J. Nucl. Mat.,* **2009**, *390-391*, 1017–1021.

45. "Phase formation in selected surface-roughened plasma-nitrided 304 austenite stainless steel", Singh G. P., Joseph A., Raole P. M. et al., *Sci. Tech. Adv. Mat.,* **2008,** *9*, 025007(1-5).

46. "Improvement of calibration assessment for gold fast-neutron activation analysis using plasma focus devices", Tartari A., Verri G., Da Re A. et al., *Meas. Sci. Technol.,* **2002**, *13***,** 939.

47. "Non-destructive assay of fissile materials through active neutron interrogation technique using pulsed neutron (plasma focus) device", Tomar B. S., Kaushik T. C., Andola S. et al., *Nucl. Instrum. Methods Phys. Res. A,* **2013**, *703*, 11–15.

48. "Fast Neutron Activation Analysis of gold by inelastic scattering, ^{197}Au (n, n'γ) ^{197}Au^{m}, by means of Plasma Focus device," Verri G., Mezzetti F., Da Re A. et al., *Nukleonika,* **2000**, *45(3)*, 189–191.

49. "Deposition of un-hydrogenated diamond-like amorphous carbon films by electrolysis of organic solutions", Wang H., Shen M. R., Ning Z. Y. et al., *Thin Solid Films,* **1997**, *293*, 87-90.

50. "Impact of low energy helium irradiation on plasma facing metals," Yoshida N., Iwakiri H., Tokunaga K. et al., *J. Nucl. Mat.,* **2005**, *337-339*, 946-950.

Chapter 6

Summary and Future scope of Studies

6.0 Summary

The present work includes design, development and characterization of pulsed radiation sources based plasma focus devices for applications in different areas. A Faraday cup is indigenously designed, developed and characterized for time resolved measurement of ions. Plasma focus devices operating at 200 J to 17 kJ are optimized for pulsed radiations including neutrons and ions. The parameters like electrodes dimensions, electrodes configurations, insulator, filling pressure as well as transmission lines for a given operation energy are optimized for maximum radiation output. By multiple iterations of electrodes dimensions, neutrons emissions from a miniature and portable sealed tube based device, SPF1-P2, are observed. This device is characterized for neutron emissions for 200 shots without purging deuterium filling gas between shots. This device has plasma chamber of effective volume of 33 cm^3 which is smallest among its class of miniature devices.

Compatibility of plasma focus device for repetitive operation is studied in PF-P5 device. Enhancement in time averaged neutron yield is observed by repetitively operating at a repetition rate of 10 Hz. Time resolved measurements of neutrons performed using PSD detector revealed that the neutrons yield/pulse vary from shot to shot at the same operation conditions but time integrated neutron is typically multiplied by number of shots in repetitive operations. The reason may be attributed to the fact that the impurities and their effects on plasma sheath are statistically distributed. Also, the leakage current may vary in each shot and this results into variation in pinch current (I_p).

Three different plasma focus devices operating in kilojoule range viz. PF-2, MEPF-12 and MEPF-17 have been optimized for radiation emissions as well as to understand the plasma focus dynamics. The PF-2 and MEPF-12 devices are assembled using parallel-plate transmission lines whereas multiple coaxial cables are used in MEPF-17. The parallel plate transmission lines reduce the

overall system inductance as well as they make the whole system compact and transportable. The coaxial cables provide the desired flexibility to the plasma focus head.

The PF-2 and MEPF-12 are characterized as a compact radiation source. Time resolved emissions of neutrons and ions are measured in MEPF-12 device. A correlation between neutrons and ions is tried to establish at various filling pressures. It is found that the neutron yield varies with deuterium pressures but the ion fluence (in axial direction) remains nearly same in filling pressure range 1 – 10 mbar. The possible reason is that the although total ion is same but the velocity distribution of deuterium ions varies with filling pressure. The measurements carried out by varying operation energies, showed similar characteristics. The ion fluence of typically $\approx 10^{14}$ cm^{-2} is measured using faraday cup signal in MEPF-12 device (11.5 kJ, 499 kA). Similar order of ion fluence is measured in PF-2 device (2 kJ, 225 kA) and MEPF-17 device (17 kJ, 506 kA). This reinforces the concept of "plasma focus scalability" for ions which essentially means that plasma focus devices of all the energies have same ion fluence. This means that a similar ion energy spectrum, although at a different scale can be achieved with operation energies in the range of sub-kilojoule to megajoule.

The angular anisotropy in ion emissions is measured using CR39 track detectors in MEPF-12. It is found to be more along the electrodes axis than in the perpendicular directions and it also varies with filling pressure. This is assumed to be the main reason of anisotropy in neutron yield and their energy. To further confirm, anisotropies in neutron yield/energy i.e. ratio of neutron yield/ energy in the axial to that in the radial direction were measured in MEPF-17 device by varying the filling pressures at 17 kJ. It was observed that the anisotropy factor for neutron yield and neutron energy was (1.33 ± 0.18) and (1.35 ± 0.09) respectively. This suggests that the mechanism of neutron emission is predominantly a beam-target phenomenon, in conformity with other reports.

Samples of different materials (W, Mo, Cu, Ni and SS304) have been exposed to fusion grade plasma in the MEPF-12 device. The combined effects of ions, neutrons, plasma streams, X-rays on the surfaces of the above samples have been studied. They are expected to produce damages in the

sample under irradiation (thermal as well as radiative). The thermal damage consists of melting and evaporation as well as micro-cracks due to thermal stress on the surface layer of material. The radiation damage consists of sputtering of surface layer as well as various crystalline effects such as vacancies, interstitials, pores, bubbles etc. Comparative analysis of surface damages on the samples of various materials suggests that they are highly dependent on materials physical, thermal as well as mechanical properties. Among the samples studied here, the W has the least and the Cu has the most damage in various forms. The reason is attributed to various properties of W such as the high melting point (3695 K), high threshold for sputtering (212 eV), high elastic constant (411 GPa) among others. The study reinforce for use of W as the first wall material in ITER fusion reactor.

The observed phase transition (ferritic-austenitic to austenitic) in SS is attributed to the fact the implanted deuterium atoms occupy interstitial sites which triggers the phase transition. Moreover, shock wave could also result in displacement of atoms of alloying elements into an interstitial position which could trigger the phase structural transformations. This study shall prove to be useful in understanding pulse fusion grade plasma and material interaction and also in predicting various other materials behavior in fusion reactor environment.

Study on deposition of DLC on Si substrate and its characterization further bolsters the position of plasma focus device as tool to modify the surface tribological properties through coatings of various materials on different substrate materials.

Non-destructive assay of ^{235}U in varying masses of U_3O_8 samples is performed using pulse neutrons. Detection of ^{235}U as low as 14 mg using this method proves that plasma focus device can be efficiently and effectively used for detection of explosives and illicit materials present in trace amounts.

Feasibility study on production of short-lived radioisotopes (^{56}Mn, ^{198}Au, ^{165m}Dy) and their half-life measurements proves potential applications of plasma focus devices in producing

radioisotopes for application in different areas such as for medical applications [Boron Capture Neutron Therapy (BCNT)].

6.1 Future scope of studies

Ion fluence is observed to be nearly same for three different plasma focus devices PF-2, MEPF-12 and MEPF-17. Also, it is seen to be nearly independent of filling pressures and operation energies. The anisotropy in ions can be studied in different plasma focus devices and effects of filling pressures and operation energies on them can be studied further. Deuterium ion acceleration and their propagation in the thermal plasma and background neutral gas can further be studied. This will be useful in understanding accelerated ion-plasma interactions, effects of collisions with neutrals/ thermal plasma on the ion energy spectrum and range of ions and for estimating the neutron emission per unit path length traversed by deuterium ions in the pinch plasma and background plasma.

Interaction of pulsed ions with materials can be studied further to understand the structural phase transformation mechanism in stainless steel sample. The ions of different species can be produced and accelerated to high energies in the plasma focus devices. They can be used in implantation into surfaces of different material and improve their surface tribological properties important for many commercial applications. The transformation in structural phase of SS sample needs to be probed in detail to understand its mechanism as well as to induce phase transformations in other materials useful for many applications.

Applications of energetic ions may further be used for production of radioisotopes useful for medical applications and measurement of their half-lives.